Ministère de l'enseignement Supérieur et de la recherche Scientifique
وزارة التعليم العالي والبحث العلمي

Badji Mokhtar Annaba University
Université Badji Mokhtar – Annaba

Faculté de Technologie

Département Hydraulique

جامعة باجي مختار – عنابة
كلية التكنولوجيا
قسم الري

Thèse

Présentée pour obtenir le diplôme de

Doctorat Troisième Cycle

Filière : Hydraulique

Spécialité : Hydraulique urbaine

Par :
DJELLIT Leila

Thème :

Effet du changement climatique et de l'occupation du sol sur la réponse des bassins versants : Cas Nord-Est de l'Algérie

Thèse soutenue le 30/10/2024 devant le jury composé de :

N°	Nom et prénom	Grade	Etablissement	Qualité
01	HAMMAR Yahia	Prof.	Université Badji Mokhtar -Annaba	Président
02	LAOUACHERIA Fares	MCA	Université Badji Mokhtar -Annaba	Rapporteur
03	KECHIDA Said	MCA	Université Badji Mokhtar -Annaba	Examinateur
04	HEDDAM Salim	Prof	Université de Skikda	Examinateur
05	MAROUF Nadir	Prof	Université d'Oum El Bouaghi	Examinateur

"تأثير تغير المناخ واستخدام الأراضي على استجابة مستجمعات المياه: حالة شمال شرق الجزائر "

الملخص:

شهدت الجزائر، كغيرها من بلدان حوض البحر الأبيض المتوسط، فيضانات كبيرة أدت إلى خسائر في الأرواح والممتلكات. السبب الرئيسي لهذه الفيضانات هو تغيرات استخدام الأراضي والغطاء الأرضي (LULC) وتقلب المناخ. تركز هذه الدراسة على فحص وتقييم التأثيرات الفردية والمجمعة لتغيرات LULC وتأثيرات تغير المناخ على ذروة التصريف وحجم الجريان السطحي في مستجمع نهر كبير باستخدام تقنيات وأساليب مختلفة. تم استخدام تحليل LULC من عام 1985 إلى عام 2020 باستخدام صور الأقمار الصناعية Landsat 5 و Landsat 7 ETM + والشبكة العصبية الاصطناعية الخلوية (CA-ANN) لتوليد التغيير المتوقع لخريطة LULC لعام 2040. بشكل عام، امتد تغير استخدام الأراضي إلى المناطق الحضرية والزراعية على حساب الغابات والأراضي الجرداء. تم ربط البيانات المناخية المتوقعة المشتقة باستخدام نموذج الدوران العالمي من Europe-CORDEX بنموذج الدوران الإقليمي RCA4-CNRM-CERFACS-CM5 لمسارين تمثيليين للتركيز (RCP 4.5 و8.5)، مع تصحيح التحيز للفترة بين 2020-2060. مركز الهندسة الهيدرولوجية - تم استخدام نموذج نظام النمذجة الهيدرولوجية (HEC-HMS) لتقدير ذروة التصريف المستقبلي وحجم الجريان السطحي لفترات وسيناريوهات مختلفة لتغير استخدام الأراضي و التغير المناخي. تمت معايرة نموذج HEC-HMS للفترة من 1984/12/18 إلى 1985/07/31 وتم التحقق من صحته للفترة من 2003/01/01 إلى 2003/07/31. أظهرت النتائج دقة جيدة فيما يتعلق بمعايير RMSE وNSE وR2 وKGE للمعايرة والتحقق من حجم ذروة التصريف والجريان السطحي. وخلص تحليل معدل المساهمة الفردية والمجمعة إلى أن التأثير على تغير المناخ يتجاوز بكثير تأثير استخدام الأراضي. ويختتم التحليل بتقييم شامل لاتجاهات هطول الأمطار ودرجة الحرارة والتصريف، كما كشف عنها اختبار مان-كيندال. وتوقعت النتائج حدوث انخفاض كبير في هطول الأمطار والتصريف بحلول عام 2060، يصاحبه ارتفاع في درجات الحرارة.

كلمات مفتاحية: النمذجة الهيدرولوجية، استخدام الأراضي، تغير المناخ، اختبار مان-كيندال، HEC-HMS، RCM، CA-ANN

« Effet du changement climatique et de l’occupation du sol sur la réponse des bassins versants : Cas Nord-Est de l’Algérie »

Résumé :

L'Algérie, comme d'autres pays du bassin méditerranéen, a connu d'importantes inondations qui ont entraîné des pertes en vies humaines et en biens. La principale cause de ces inondations est le changement d’occupation des sols et la variabilité climatique. L'objectif de cette étude est d'examiner et d'évaluer les impacts individuels et combinés des changements d’occupation des sols et les impacts du changement climatique sur le débit de pointe et le volume de ruissellement dans le bassin versant de l’oued Kébir en utilisant différentes techniques et approches. L'analyse de l’occupation des sols de l’année 1985 à 2020 à l'aide d'images satellites classifiées (Landsat 5 et Landsat 7 ETM+) et du réseau neuronal artificiel d'automates cellulaires (CA-ANN) a été utilisée pour générer le changement prédit de la carte d’occupation des sols de 2040. Dans l'ensemble, le changement d’occupation des sols s'est étendu aux zones urbaines et des zones agricoles au détriment des forêts et des terres arides. Les données climatiques projetées dérivées à l'aide du modèle de circulation mondiale d'Europe-CORDEX ont été couplées au modèle de circulation régionale RCA4-CNRM-CERFACS-CM5 pour deux voies de concentration représentatives (RCP 4,5 et 8,5), avec correction du biais pour la période

2020-2060. Le modèle Centre d'ingénierie hydrologique - Système de modélisation hydrologique (HEC-HMS) a été utilisé pour estimer les futurs volumes de ruissellement et débits de pointe pour différentes périodes et scénarios de changement d'occupation des sols et de changement climatique. Le modèle HEC-HMS a été calé pour la période du 18/12/1984 au 31/07/1985 et validé pour la période du 01/01/2003 au 31/07/2003. Les résultats ont montré une bonne précision par rapport aux critères RMSE, NSE, R2 et KGE pour l'étalonnage et la validation du débit de pointe et du volume de ruissellement.

Mots clés : Modélisation hydrologique, Occupation des sols-couverture végétale, changement climatique, test de tendance Mann-Kendall, HEC-HMS, RCM, CA-ANN.

« Effect of climate change and land use on the response of catchments: Case of North-East Algeria »

Abstract :

Algeria, like other countries in the Mediterranean basin, has experienced major floods that led to loss of life and property. The main cause of these floods is land use and land cover (LULC) changes and climate variability. The focus of this study is to examine and evaluate the individual and combined impacts of LULC changes and the impacts of climate change on the peak discharge and runoff volume in a Kebir river catchment using different techniques and approaches. The LULC analysis from 1985 to 2020 using classified Landsat 5 and Landsat 7 ETM+ satellite images and Cellular Automata Artificial Neural Network (CA-ANN) were used to generate the predict change of LULC map of 2040. In overall, LULC change has expanded into urban and agricultural areas at the expense of forests and bare lands. Projected climate data derived using global circulation model from Europe-CORDEX were coupled to regional circulation model RCA4-CNRM-CERFACS-CM5 for two representative concentration pathways (RCP 4.5 and 8.5), with bias correction for the period between 2020-2060. The Hydrological Engineering Center - Hydrological Modeling System (HEC-HMS) model was used to estimate future peak discharge and runoff volume for different periods and scenarios of land use change and climate change. The HEC-HMS model was calibrated for period of 18/12/1984 to 31/07/1985 and validated for period of 01/01/2003 to 31/07/2003. The results showed good accuracy in relation to RMSE, NSE, R2, and KGE criteria for the calibration and validation of the peak discharge and runoff volume.

Key words: Hydrological modeling, Land use - Land cover, Climate change, Mann-Kendall Trend test, HEC-HMS, RCM, CA-ANN.

ACKNOWLEDGEMENTS

I would like to express my sincere gratitude to my Supervisor MCA LAOUACHERIA Fares whose expert advice, suggestions and support guided me through this research successfully. His invaluable guidance, continuous help, and attention to details, were instrumental in shaping the direction and quality of this thesis.

I would like to thank Professor Hammar Yahia from University of Badji Mokhtar, Annaba, for their dedicated mentoring and excellent review, which led to the successful completion of my dissertation.

I would like to thank MCA KECHIDA Said from University of Badji Mokhtar, Annaba, for their immense support and their willingness to provide answers to all my numerous questions.

I would like to thank Professor HEDDAM Salim from University of 20 Août 1955, Skikda, for their dedicated mentoring and excellent review, which led to the successful completion of my dissertation.

I would like to thank Professor MAROUF Nadir from University of Larbi Ben Mhidi, Oum El Bouaghi, for their dedicated mentoring and excellent review, which led to the successful completion of my dissertation.

I would like to thank the academic and administrative staff of the Hydraulic department and the Hydraulic and Soil Laboratory, for their valuable teachings and assistance throughout my academic journey.

I would like to express my gratitude to Professor MORBIDELLI Renato and his entire team at the Civil and Engineering Department of the University of Perugia for hosting me during my internship. It was a valuable learning experience. Their warm welcome and guidance greatly contributed to my academic development.

I want to extend my appreciation to the Research Institute for Geo-Hydrological Protection (IRPI) within the National Research Council of Italy (CNR) in Perugia for receiving me. Their willingness to share ideas helped me obtain significant insights and essential expertise in the subject of hydrology.

Last but not the least, I am particularly grateful to my family and friends for their encouragement and support throughout my research.

List of Abbreviations

ANN – Artificial Neural Network

ANRH - National Agency for Hydraulic Resources

AR - Assessment Report

CA-ANN - Cellular Automata Artificial Neural Network

CMHyd - Climate Model for Hydrological Modeling Tool

CMIP5 - Coupled Model Intercomparison Project Phase 5

CN – Curve Number

CORDEX - Coordinated Regional Climate Downscaling Experiment

DEM - Digital elevation model

DM - Distribution Mapping

FAO - Food and Agriculture Organization

GCM - Global climate models

GHG - Greenhouse gas

GIS - Geographical information systems

GMST - Global Mean Surface Temperature

HEC-HMS - Hydrologic Engineering Centers-Hydrologic Modeling System

HSG - Hydrologic Soil Groups

HYSOG - Global Hydrologic Soil Groups

IMP - Impervious

IPCC - Intergovernmental Panel on Climate Change

KGE – Kling-Gupta Efficiency criterion

KRC - Kebir River Catchment

LCM – Land Change Modeler

LOCI - Local intensity scaling

LR – Logistic Regression

LS - Linear scaling

LULC - Land use -Land cover

MAE - Mean absolute error

MCE - Multi-Criteria Evaluation

MK - Mann-Kendall

MLP - Multi-Layer Perceptron

MOLUSCE - Modules for Land Use Change Simulations

NSE - Nash-Sutcliffe Efficiency criterion

OFAT - One-factor-at-a-time

PET - Potential evapotranspiration

PT - Power Transformation

R^2 - Correlation coefficient

RCM - Regional climate models

RCP - Representative Concentration Pathway

RMSE - Root Mean Square Error

RS - Remote sensing

SCS - Soil Conservation Service

SRTM - Shuttle Radar Topography Mission

SWAT - Soil and Water Assessment Tool

USGS - United States Geological Survey

VS - Variance scaling

WoE - Weights of Evidence

List of Figures

List of Tables

Introduction

Urbanization include the growth of urban populations, built-up areas, and agricultural grounds. According to the United Nations (Nugroho et al., 2018; United Nations, 2018), the global urban population is expected to reach 68% by 2050, as of 55% now, with Asia and Africa accounting for over 90% of the increase. As urbanization develops in accord with societal and economic growth, diverse human activities and interventions have a major effect on the landscape, hydrological cycle, and water resources via multiple means (Li et al., 2023). Rapid expansion in built-up areas will result in fewer natural open spaces and more impermeable surfaces. Increased impervious surface area makes a watershed more hydrologically active (Hu and Shrestha, 2020). This type of land use land cover (LULC) changes can especially raise extensive drought or flooding potential risks in cities. In order to reduce those adverse effects of future land development, it's crucial to analyze and comprehend projected changes in runoff regimes (Huq and Abdul-Aziz, 2021). Increased human activity due to urbanization causes greenhouse gas concentrations (GHGs) to escalate at a rapid rate. This, in turn leads to climatic extremes (drought or flood) with the mid-to-high latitudes observing greater humidity and the subtropics getting drier over time. The rise in temperature and decline in precipitation witnessed over comparable periods, in the Mediterranean region, exhibit a major impact on water resources availability and industrial and agricultural activities (Trenberth, 2018; Derdour et al., 2022). To establish effective, long-term, and sustainable strategies for water and land resource management, decision and policy makers must comprehend the effects of LULC alterations and climatic variability on watersheds.

Land use describes the human exploitation of the natural environment for shelter and subsistence, while land cover refers to the biophysical characteristics such as vegetation, soil and water distributed on earth's surface (Liping et al., 2018). Human activity-induced changes in land use can affect land cover, detrimentally affecting the natural environment and biosphere. These changes can result in the loss of natural ecosystems and biodiversity. (Rawat and Kumar, 2015). Land use-land cover change has the potential to influence hydrological processes, in a watershed, due to this fact, it is one of the key drivers of stream flow shift. LULC Change can alter watershed runoff and stream flow generation processes, including a change in peak discharge (Hurkmans et al., 2009; Msovu et al., 2019; Chen et al., 2020). Expanded impermeable cover and limited storage capacity in natural basins, both of which result from reduced soil infiltration, increase the speed and volume of generated runoff. Increased drainage density allows for quicker transit of water to

the main stream, resulting in faster and greater peaks in the flow rate of receiving streams under high water input, such as heavy rainfall or rapid snowmelt. This occurrence has been shown to have severe effects, such as a longer return period for mild floods, lower baseflow, and changes in groundwater dynamics (Huang et al., 2008; Rezaei et al., 2019).

Assessing LULC, monitoring evolving patterns, and identifying optimal land resource usage are all critical components for efficient land use planning and water resources management. Climate change (CC) analysis is another major component to discover hydrological processes behaviors in watersheds. The change in temperature and precipitation factors of the cycle are direct consequences of Climate change.

According to the Copernicus Climate Change Service (C3S), the global surface air temperature rose by 1.17°C above the average for the 1991-2020 reference period. As per a recent report of the Intergovernmental Panel on Climate Change (IPCC) Sixth Assessment Report (AR6), The global mean surface temperature (GMST) has increased by 1.1°C (2.0°F) since the pre-industrial period (Unger, 2010; Shukla et al., 2019). These changes are projected to perturb the hydrological cycle (i.e. rainfall-runoff interplay). Water storage will also be affected, and evapotranspiration will rise, resulting in rainfall timing and intensity variations. Ultimately, extreme hydro-meteorological events can cause water supply spatio-temporal availability to be stressed, which can have detrimental effects on sectors such as agriculture, industry, and urban development (Legesse et al., 2010; Kiprotich et al., 2021). Regional climate models (RCM) are an excellent tool to explore the impacts of past and future climate change on the hydrological cycle. RCMs are global climate models (GCMs) that have been reduced to a regional scale by dynamical descaling and serve in a variety of research that focus on smaller regions (Mami et al., 2021). The Coordinated Regional Climate Downscaling Experiment (CORDEX) initiative provided various regional climate projections in different domains worldwide (WRCP, 2015). These projects includes four Representative Concentration Pathways (RCP) that represent different trajectories of future emissions and atmospheric concentrations of GHGs (RCP 2.6, RCP 4.5, RCP 6.0, and RCP 8.5). This study applied RCP 4.5 and 8.5 of these scenarios. The RCP4.5 scenario is categorized as an intermediate emission scenario, with CO2 levels ranging from 580 to 720 ppm by the year 2100. In contrast, the RCP8.5 scenario signifies high emissions, resulting in a CO2 concentration surpassing 1000 ppm by 2100 (Zhang et al., 2018a). In light of these emission scenarios and their impact on hydro-climatic variables, forecasting accurate water resources, especially in arid and

semiarid areas with high evaporation and low rainfall volume, necessitate a thorough examination of hydrologic variable trends, such as recorded and predicted hydrologic and meteorological data (Forootan, 2019). It is imperative to pinpoint the changing traits of climatic and hydrological time series, since they have demonstrated to be non-stationary in various global regions (Liu et al., 2022).

Hydrologic modeling is a conceptual representation of a part of the hydrologic cycle, and a powerful approach to deal with impacts of LULC Change and Climate Change. Hydrologic models might differ substantially based on the environment of interest, availability of data, or accuracy demand. The availability of modern computation tools and easy access to spatial geographical and meteorological data, as well as the incorporation of geographical information systems (GIS) and remote sensing (RS) in distributed hydrological models, simplified and improved the process of defining physical parameters for a watershed in a hydrologic model (Kusre et al., 2010; Hu and Shrestha, 2020). This advanced modeling technique simplifies and enhances the simulation for rainfall-runoff and evaluation of the impact of the changes mentioned above.

The combined application of RS and GIS proves to be a cost-effective and accurate technique in LULC Change detection and hydrology dynamics tracking (Shen et al., 2020). LULC mapping is updated on a constant basis using permanent inventory of imagery provided by Satellite RS and Landsat data. To determine changes during mapping and hydrologic modeling, it is critical to utilize GIS as a tool for integrating data from several sources and combining the implications of topographic maps, hydrological data, meteorological data, soil data and classified images (Baig et al., 2022). The Cellular Automata Artificial Neural Network (CA-ANN) approach, found in QGIS version 2.0 and later MOLUSCE plugin, is an efficient method for assimilating existing LULC data and accurately predicting the spatio-temporal distribution of LULC Change (Blissag et al., 2023). ANN is used to determine CA's local transition rules, thereby improving its utility in understanding and simulating LULC dynamics. This global non-parametric land change modeler (LCM) functions as a non-linear data mining tool, making it highly effective in processing inaccurate and inferior data (Yang et al., 2016; Dede et al., 2022). The CA-ANN model stands out due to its dynamic simulation capability, efficient performance with minimal data, ease of calibration, and ability to replicate intricate patterns (Baig et al., 2022). Additionally, The Climate Model for Hydrological Modeling Tool (CMhyd) serves to rectify systematic flaws detected in RCMs that prevent the direct use of simulated output. The program features multiple bias-

correction approaches, such as linear scaling, variance scaling, power transformation, local intensity scaling and distribution mapping (Rathjens et al., 2016). It is utilized to generate simulated climate data for research on the effects of climate change, facilitating the forecast of essential climatic variables under various scenarios such as RCP4.5 and RCP8.5. Thus, enabling the assessment of trends and consequences on stream flow dynamics and other hydrological parameters (Rashid et al., 2021; Orkodjo et al., 2022).

A specific issue in hydrological modeling is considering LULC Change as an inherent component when setting appropriate parameters for the rainfall-runoff model (Jiang et al., 2015). Among many, conceptual distributed hydrologic models Hydrologic Engineering Centers-Hydrologic Modeling System (HEC-HMS) is extensively used for long-term hydrology simulation with respect to LULC Change and Climate Change (Saghafian et al., 2008; Zope et al., 2015) and analysis of their impact on hydrological processes (Hachemaoui et al., 2022). HEC-HMS is designed to implement a rainfall-runoff model capable of simulating rainfall events corresponding to the Kebir River Catchment (KRC), in Algeria. The watershed's parameters must be established in conjunction with particular local conditions before it can be utilized to estimate runoff (Ford et al., 2008). The catchment area's features and the hydrological forecast's purpose within that catchment determine the rainfall-runoff model used (Abdulkareem et al., 2018). GIS and RS data at various resolutions are used in HEC-HMS to simulate hydrological processes at multiple levels. It has been noticed that the primary constraints of using the HEC-HMS model in KRC is the difficulty to adequately calibrate and validate applications due to the lack and scarcity of measured data at the level of gauged station. Despite its limitations, the HEC-HMS model remains the most logical and scientifically proficient means of understanding the complex hydrological behavior of catchments (Zhang et al., 2013).

Low-lying areas of the Ain Charchar region, where the Kebir River flows through, are prone to periodic floods, affecting largely agricultural fields. One of the Kebir River's main rivulet is part of the Skikda city, while the other is related to the Guelma city. These regions of northeastern Algeria are characterized by high and irregular precipitation. To address the issue and capitalize on the hydric excess, The Zit Emba Dam, located 2 km from the town of Bekkouche-Lakhdar in the Skikda Province, was constructed in 1989, but its impoundment did not start until 2003. Despite this, the plains of Ain Charchar still experiences recurrent small floods. This is the first study of its type that models rainfall-runoff in order to offer information on peak discharge and stream flow

fluctuation during various rain events in KRC, allowing to appropriately prepare for extreme events and their repercussions. Rainfall-runoff modeling within KRC is imperative to grasp intricate processes in the hydrologic cycle that are taking place now and forecasting future extreme events. Hence, this research aims to assess trends in climatic and hydrological data, predict the LULC map for the year 2040, and subsequently evaluate the variation in peak discharge and runoff volume relative to climate and LULC changes. This was achieved by:

* Monitoring LULC Change that occurred from 1985 to 2020 and projecting the 2040 LULC map via QGIS's MOLUSCE plugin and classified Landsat images.

* Correcting RCMs climatic data and forecasting future precipitation and temperature data under two representative concentration pathways of gas emission scenarios (RCP 4.5 and RCP 8.5) for the period 2020 to 2060.

* Simulating daily runoff for KCR using a GIS-implemented HEC-HMS model and Generating rainfall-runoff hydrographs, for estimated LULC Change, between 1985 and 2040, and for different storm events;

* Evaluating the model performance using performance criteria, such as RMSE, NSE, KGE and R^2.

* Assessing the individual contribution rate of climate change and land use-land cover;

* Analyzing climatic and hydrological time series using non-parametric Mann-Kendall (MK) trend test approach;

The long-term purpose of this study is to assist decision-makers design a more sustainable water resources management plan while also reducing possible disasters caused by extreme events. This is accomplished by providing valuable insights into the variability of intrinsic hydrological process parameters; along with trends in climate change (CC) and land use and land cover change (LULC Change).

Chapter I: Context and literature review.

Landscape Context of Flooding: Factors at Play.

Flooding stands as a serious natural hazard, resulting in various losses and damages. In urban settings, it devastates property and infrastructure, putting lives at risk. Meanwhile, in agricultural plains, it leads to crop losses and triggering food shortages. Climate change's drastic shift in precipitation patterns, along with significant variations in land use and land cover (LULC), has an important effect on hydrological processes within a watershed, provoking the occurrence of flooding (Zope et al., 2017). The Ain Charchar Area, located in the Kebir River catchment and encompassed by the Constantinois coastal basins, is recurrently susceptible to periodic floods. This low-lying region, primarily used for agricultural purposes, occasionally suffers severe losses.

Figure 1. Flood event in Kebir River, April 2024.

Figure 2. Kebir River, Flood event April 2024.

Monitoring flood events is capital and requires an understanding of the changes occurring in climate and land use/land cover (LULC). It is necessary to evaluate the hydrological regime's fluctuations that result from these two key factors and their interplay (Zhang et al., 2018a; Li et al., 2022). Integrating LULC and climate change in integrated conceptual hydrological models, coupled with GIS and remote sensing, is crucial for accurately estimating the impacts of environmental changes on hydrological processes. Moreover, this will help overcome the challenges associated with projecting future hydrological responses to LULC and climate change.

Climate change impact review

Climate change, more specifically resulting from anthropogenic forces, commonly referred to as radiative forcing, is a subject that interested many researchers. Radiative forcing measures the influence that different factors, such as greenhouse gas emissions (GHG), aerosols in the atmosphere and changes in the Sun's energy output, have on the Earth's climate and temperature.
The IPCC's Fifth Assessment Report (AR5) attributes over half of the observed increase in global average surface temperature from 1951 to 2010 primarily to the rise in greenhouse gas (GHG) concentrations, alongside other anthropogenic forcing (Scott et al., 2016; Arias et al., 2021). The IPCC's Sixth Assessment Report (AR6) further reinforces this statement, linking 100% of the observed global warming since 1970 to urbanization and industrial growth (Ming et al., 2021; IPCC, 2023). Additionally, IPCC AR6 documented an annual CO2 emissions increase of about 90%, from 15.8 GtCO2 to 36.7 GtCO2, between 1970 and 2019 (**Figure 3**, (Stainforth and Pepinster, 2022)).

Global warming has extensive consequences, such as rising sea levels from melting snow and ice, changing weather patterns, and increasing evapotranspiration. These changes result in shifts in average precipitation and variations in precipitation event characteristics and patterns. As a result, the hydrological cycle is impacted, leading to uneven global distribution of effects, including significant alterations in wet and dry seasons (Mamuye and Kebebewu, 2018; Giorgi et al., 2019).

The (IPCC, 2023) projects a general increase in global surface temperature (+4.4°C) and precipitation (+17%) by the end of the 21st century under climate change at a global scale. Since 1976, a significant shift in global average land and sea surface temperatures has been documented,

with the most pronounced changes observed in middle and high latitudes of the Northern Hemisphere.

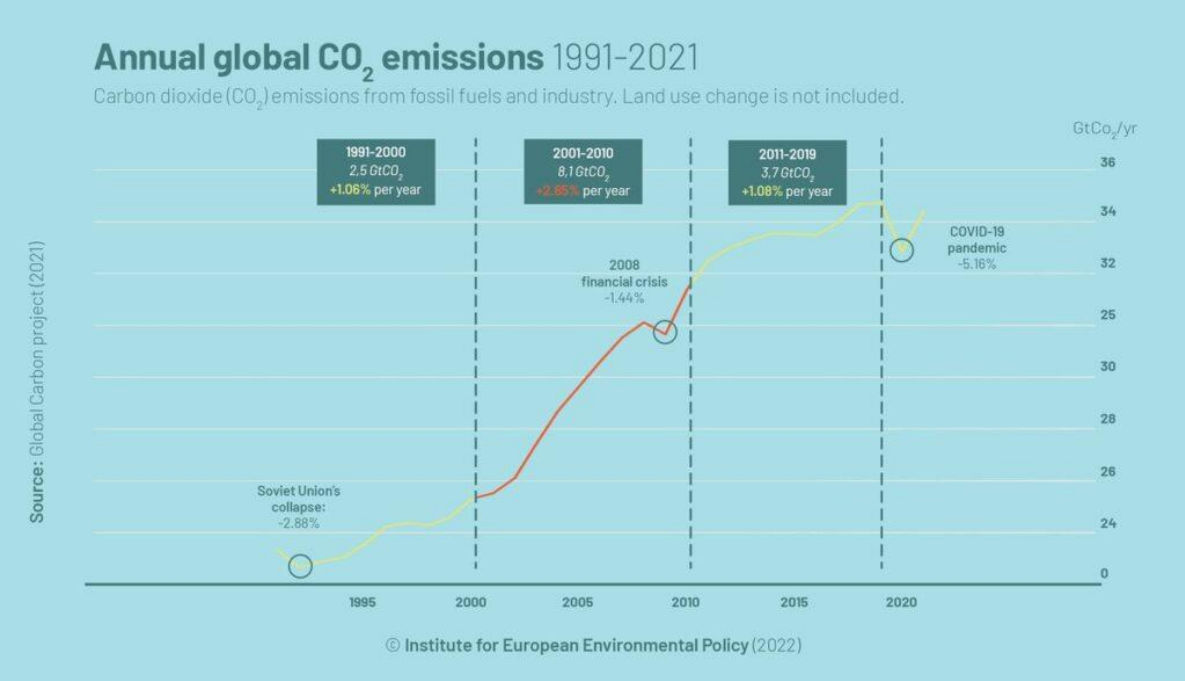

Figure 3. Annual global CO2 emission, from 1991-2021, (Global Carbon project)

Projections from climate model simulations suggest a potential overtake in global temperatures by 1.4 to 5.8°C from 1990 to 2100, unless deep reductions in GHG emissions occur in the coming decades shown in **Figure 4**, (Wuebbles et al., 2017). By the end of the 21st century, annual precipitation accumulation is expected to undergo modest to moderate alterations. Climate models projected systematic increase the intensity of mid-to-high latitudes regions precipitation and a non-uniform decline in arid and semi-arid regions precipitation, particularly under higher emissions scenarios like RCP4.5 and RCP8.5. However, as global temperature increases, precipitation is projected to decrease in the Mediterranean region across all seasons, at a rate of around -20 mm/K or -4%/K. This dying trend is not anticipated to uniformly affect all areas across the Mediterranean region. The northwest Africa and eastern Mediterranean are expected to experience the most significant impacts be the hardest hit areas (Brogli et al., 2019; Chandler, 2020; Ming et al., 2021).

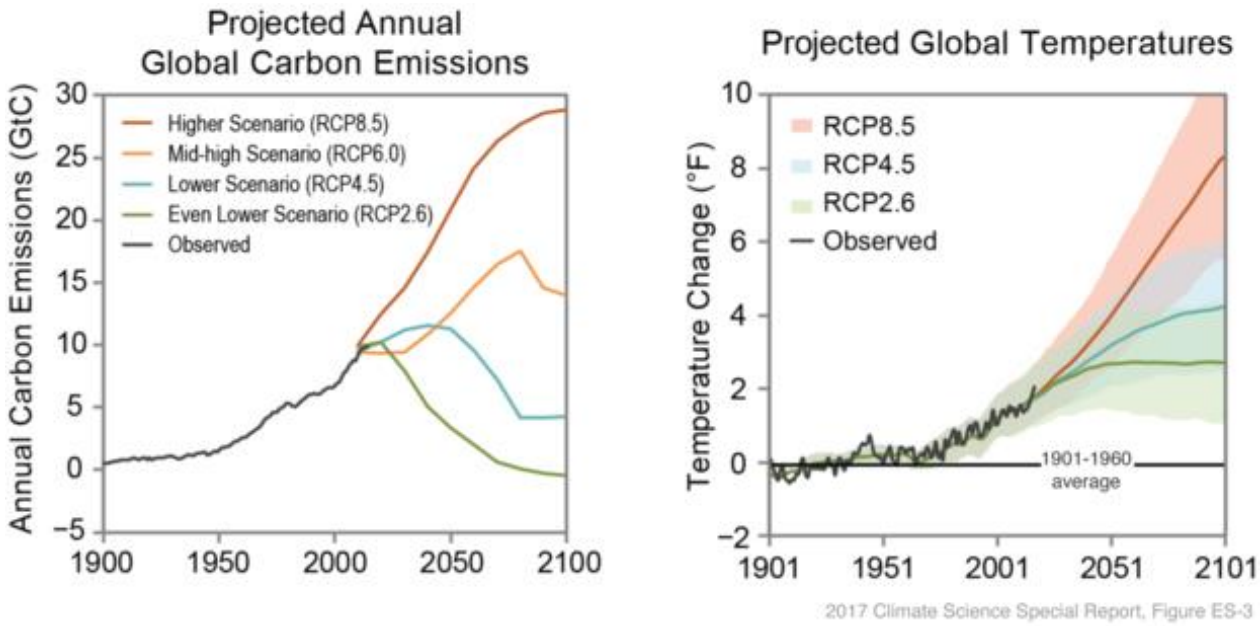

Figure 4. (left) Representative concentration pathways (RCPs) throughout the 21st century based on various possible energy policies and economic growth patterns. (right) Projected temperature increase relative to the 1901-1960 average depending on which RCP we eventually follow. (Katharine Hayhoe, 2017).

Figure 5 illustrates a rise in temperature between global climate model projections for changes in surface temperature and precipitation from 1986-2005 to 2081-2100 under two different greenhouse gas emissions scenarios (RCP2.6 and RCP8.5). The Mediterranean region is observed will experience major warming and drying trends, especially under higher emissions scenarios. Specifically, surface temperature is projected to increase substantially, with greater warming under the higher emissions RCP8.5 scenario compared to RCP2.6. In addition, precipitation is projected to decrease, with more severe drying expected under RCP8.5 than RCP2.6. The Mediterranean appears as one of the regions facing the largest percentage reductions in precipitation. These projections suggest an ensuing decline in stream flow and overall water resources.

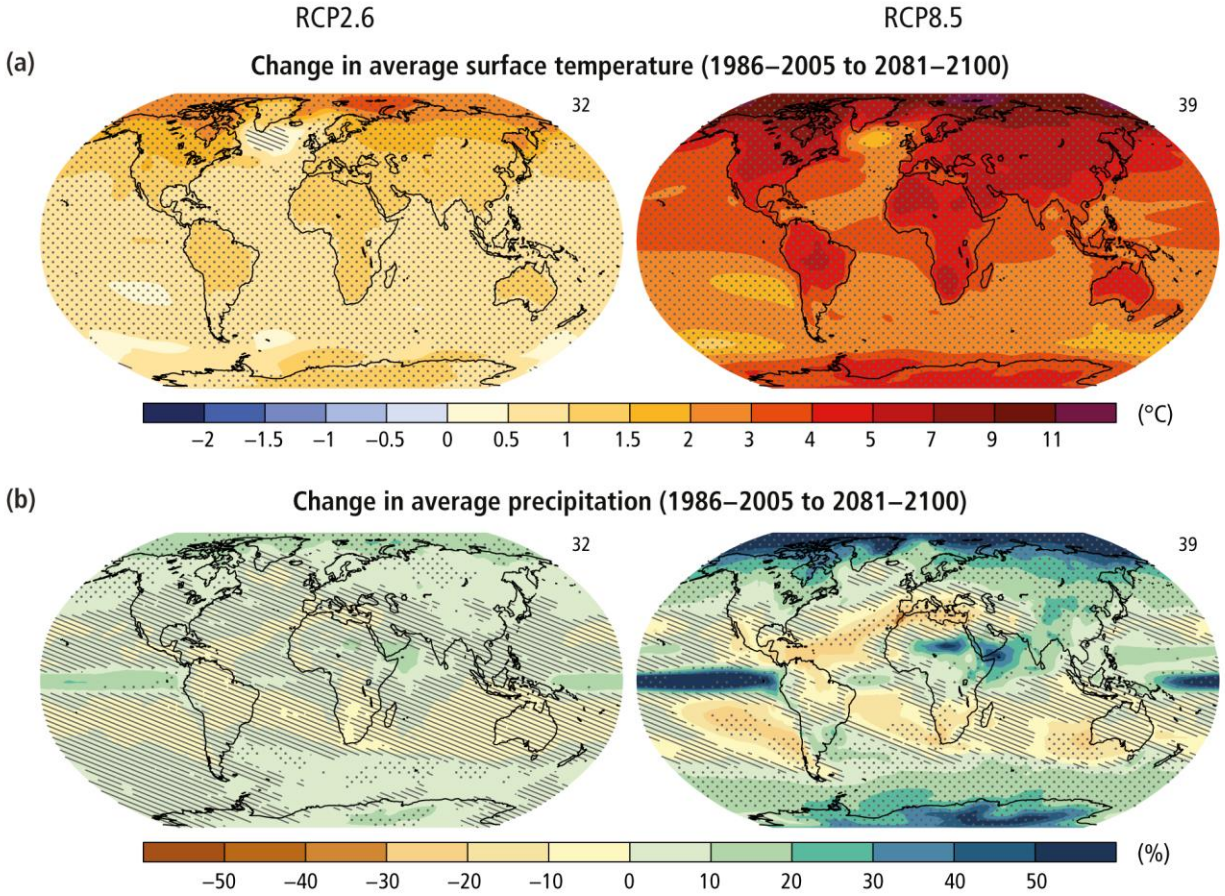

Figure 5. Coupled Model Intercomparison Project Phase 5 (CMIP5) multi-model mean projections (i.e., the average of the model projections available) for the 2081–2100 period under the RCP2.6 (left) and RCP8.5 (right) scenarios for (a) change in annual mean surface temperature and (b) change in annual mean precipitation, in percentages. Changes are shown relative to the 1986–2005 period.

Numerous Algerian researchers have investigated the impact of climate change on various regions of Algeria (Taibi and Souag, 2012; Zeroual et al., 2013; Bessaklia et al., 2018; Hallouz et al., 2019; Mami et al., 2021; Derdour et al., 2022); their studies have served as a significant source of inspiration for this work.

Taïbi and Souag (2012), analyzed temporal series of precipitation and temperature in northern Algeria over 73 years (1936-2009) to detect climate change trends. They used Pettit, Kendall and Hubert segmentation statistical tests on 102 rainfall and 4 temperature series. Within the analysis a standardized precipitation index (SPI) was used to specify drought periods.

The study discern reveals a downward trend in precipitation since 1970, particularly in the west region with a 30% rainfall deficit. Furthermore, the Pettitt test revealed a temperature rise of 0.7°C since 1980.

Zeroual et al (2013), assessed the impact of future climate change on seasonal flows of 2050 and 2100 in the Algerian-Hodna-Soummam basin. The GR2M model was used in their study to compare the average flow of the reference period (1961–1990) with future projections for 2050 and 2100. The findings revealed a potential influence of climate change on river flow in arid and semi-arid rivers in Algeria, as average monthly flows exhibited a decrease when compared to the reference period.

Bessaklia et al (2018), used Mann–Kendall (MK) test to analyze the trend in daily precipitation concentration index values. The study objective was to examine the spatial variation, the seasonality and aggressiveness of precipitation for 23 rainfall stations in the extreme northeast of Algeria over the period 1970–2010. The study results suggest that regions with limited overall precipitation experience greater concentration of daily precipitation index values. In addition, the eastern and western parts showed high seasonality and intensity of precipitation, while the central area shows a moderately seasonal pattern with lower intensity. This confirmed the impact of climate change on temperature and precipitation trends in Northeast Algeria.

Hallouz et al. (2019), studied the spatial and temporal variability of precipitation, temperature, and discharge in the Wadi Mina watershed in Northwestern Algeria from 1979 to 2013. To determine the trends of these variables, non-parametric tests such as, Kruskal-Wallis test and the Mann-Kendall test, were applied. The study found a decreasing trend in annual rainfall totals, while maximum and minimum temperatures significantly increased over time. There was a decrease in the frequency of high flow days and an increase in low flow days in the Mina, Haddad, and El Abd wadis. They concluded that the decrease in rainfall and increase in temperature led to a reduction in water resources.

Mami et al. (2021), Utilized the SWAT model for analysis, alongside climate model outputs, to assess hydrological components trends from 2020 to 2099 compared to the period 1981-2000. The study focuses on the Tafna basin, a region vulnerable to drought in northwestern Algeria. The outcomes indicates a decrease in both precipitation and river discharge, particularly in January.

Derdour et al. (2022), compared four regional climate model (RCM) estimations for averaged precipitation over the Wadi Chemora Basin in northeastern Algeria for the historical period (1970–2005) and future forecasts (2006–2100). Data from four RCMs RCA4, ICHEC-EC-EARTH, NOAA-GFDL-GFDL-ESM2M, ALADIN, and RegCM4 were adjusted using CMHyd to enhance the performance of the RCMs through bias correction methods. The results showed that precipitation was overestimated by the raw RCMs. Bias correction improved the models. The adjusted projection suggest a decline in seasonal rainfall horizons of the century periods. The projected annual rainfall was anticipated to decrease by an average of 66% by the end of the 21st century.

Land use-Land cover impact review

Land Use-Land Cover change refers to variations in the appearance and surface characteristics between two different time periods. These changes can be both natural (earthquakes, tsunamis, wildfires, floods, droughts…etc) or human-caused (Urbanization, agriculture, deforestation, mining…etc) (Sleeter et al., 2018). In this context, land use describes the human exploitation of the natural environment also referred to as land cover (Liping et al., 2018). Urban development has a significant impact on rivers (**Figure 6**), leading to increased regulation and higher runoff levels. A study examining 106 river catchments globally predicts that by 2050, around 70% of these catchments will see their streamflow disrupted and fragmented by dams in urbanized regions (Deng et al., 2015).

Deforestation has been proved to disrupt water cycle components. Minimized forest capacity to regulate water produces a variety of effects which are specific to each place (**Figure 7**). Drought hazards might worsen for some places. In others, stream flow may rise (Levy et al., 2018; Kayitesi et al., 2022; Grabowski et al., 2022). Moreover, cropland expansion at the expense of forests mostly results in land surface features modifications, such as water erosion and organic carbon loss. In addition, resulting climatic changes have been notes, surface temperatures may rise, while rainfall may decrease (Lim et al., 2017; Wolosin and Harris, 2018; Maeda et al., 2023).

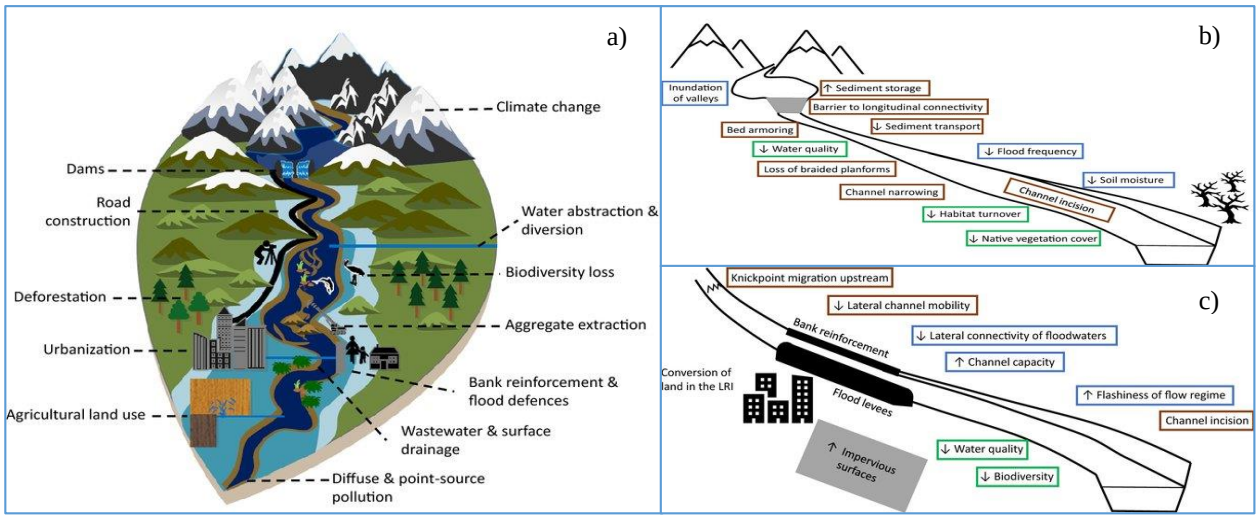

Figure 6. a) Land – River Interface (LRI) illustrating numerous human activities which may affect the land, water, and people. b) Urban alteration of the land and rivers. c) Valley-spanning dams alteration on flow regimes and disruption of sediment transport. Im pacts on LRI : hydrological (blue), geomorphic (brown), and ecological (green) (Grabowski et al., 2022).

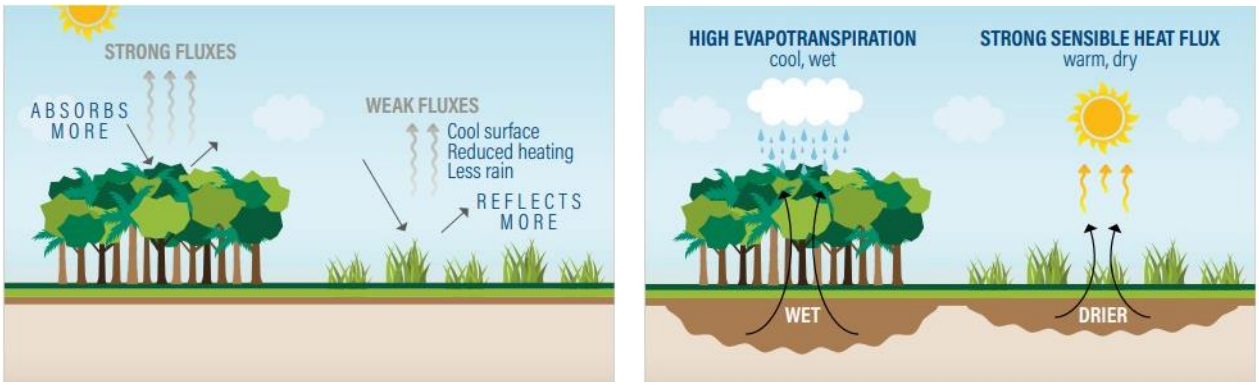

Figure 7. Effects of deforestation on surface albedo, land and evapotranspiration (Wolosin and Harris, 2018).

Overall, land use features within a region play a crucial role in shaping the hydrological processes of a catchment area. The ratio of pervious to impervious surfaces has a direct influence on stream flow dynamics. When impervious areas expand at the expense of natural areas as in **Figure 8**, runoff and total volume increase, leading to higher flooding frequency and reduced underground storage capacity (Boyd et al., 1993; Dennison et al., 2009; Mutayoba et al., 2018).

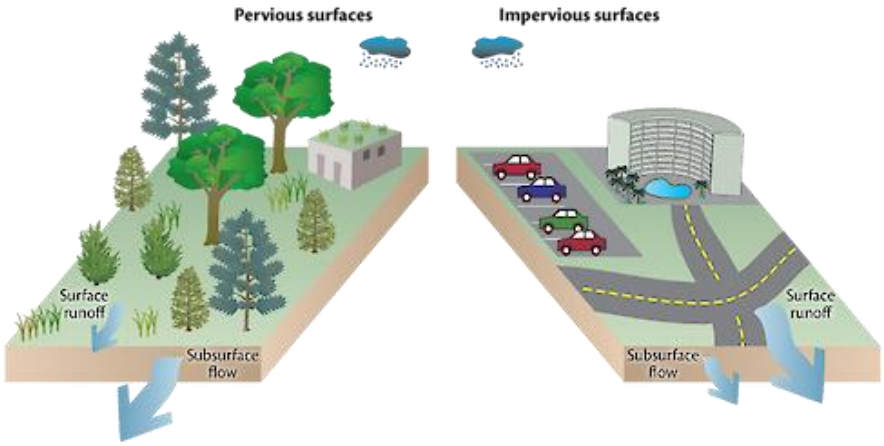

Figure 8. Conceptual diagram illustrating the differences between pervious and impervious surfaces regulation of groundwater flow and surfaces flow (Jane Thomas, 2009).

Algerian academics have conducted several studies on Land use-Land cover (Abdelkebir et al., 2021; Hachemaoui et al., 2022; Hind et al., 2022; Astite et al., 2023; Blissag et al., 2023; Weslati et al., 2023). The vast majority of their research provide useful insights for decision-makers, assisting in the formulation of sustainable management plans and land use preservation policies.

Abdelkebir et al. (2021), implemented Low-Impact Development (LID) practices, for the Guelma watershed in northeast Algeria, into GIS and Integrated the Personal Computer Storm Water Management Model (PCSWMM) to decrease simulated runoff peaks and volume. Calibration was conducted using sensitivity-based radio tuning calibration tool. The findings state that LID practices could reduce peak runoff by 54.7% and total runoff volume by 75.2% in the urban watershed.

Hachemaoui et al. (2022), used classified Landsat images, FAO soil data and the Soil and Water Assessment Tool (SWAT) model to quantify the impact of land use/land cover changes on the hydrological response of the Oued Saida basin, from 1998 to 2005. The results revealed that LULC has a clear influence on runoff, seepage water and groundwater recharge. The peak flow rise was attributed to the expansion of urban areas.

Madani Hind et al. (2022), Analyzed of the spatio-temporal change of land use and regression of agricultural and forest areas in Algiers, Algeria. In this context, Utilize GIS, remote sensing, and a

CA–Markov model to categorize and analyze land use changes in Algiers from 1987 to 2018, predict changes by 2040, and assess the impact of urbanization on agricultural and forest areas.

Blissag et al. (2023), Applied Maximum Likelihood Supervised Classification (MLSC) to Landsat data from 2000 to 2020 with a five-year interval, along with an artificial neural network (ANN) and cellular automata (CA) algorithm to simulate and predict future LULC for the years 2030, 2040, and 2050. Their objective was to identify LULC changes in the Hodna basin, forecast change scenarios up to 2050 and analyze the changes impact on the different cover classes. They documented a decrease in agricultural lands and an expansion in forest coverage, urban land. In addition, sandy soil observed an increase implying some desertification by 2050.

Weslati and Serbaji (2023), used the Revised Universal Soil Loss Equation (RUSLE), remote sensing, and GIS to compare soil losses catchment and assess soil erosion risk, between 2002 and 2018 in the Mellegue Watershed. Topography, soil erodability, rainfall erosivity, anti-erosion cultivation practices, and vegetation cover were integrated in ArcGIS 10.4 environment. The results found approximately 14,000 new areas vulnerable to erosion by water in 2018 compared to 2002. Downstream areas of the basin were the most eroded.

Astite et al., (2023), Assessed the impact of LULC changes on the hydrological response of the two watersheds Wadi Koriche and Wadi Kniss, Algiers, Algeria. Aerial and satellite images, from 1959, 1984, and 2019 were utilized to establish land use scenarios and to simulate the peak flows and runoff volumes, via Hydrologic Engineering Center-Hydrologic Modeling System (HEC-HMS). The impact of LULC changes on the hydrological response was then assessed based on changes in built environment, vegetation cover, impervious surfaces, runoff coefficients, response times, peak flows, and runoff volumes. Results showed an increase in impervious surfaces and runoff coefficients caused by the increase of built environment and a reduction in vegetation cover from 1959 to 2019. In addition, peak flows and runoff volumes both rose during the same period, causing flooding in downstream areas.

Hydrological modeling review

Hydrological modeling is the mathematical translation of the water cycle (**Figure 9**). In other terms, it is the conceptualization of reservoirs and processes in the form of equations. The main purposes of hydrological modeling are to anticipate extreme events (floods, droughts) or scenario simulations (climate change, water quality or quantity) (Yu, 2015; Ogden, 2021).

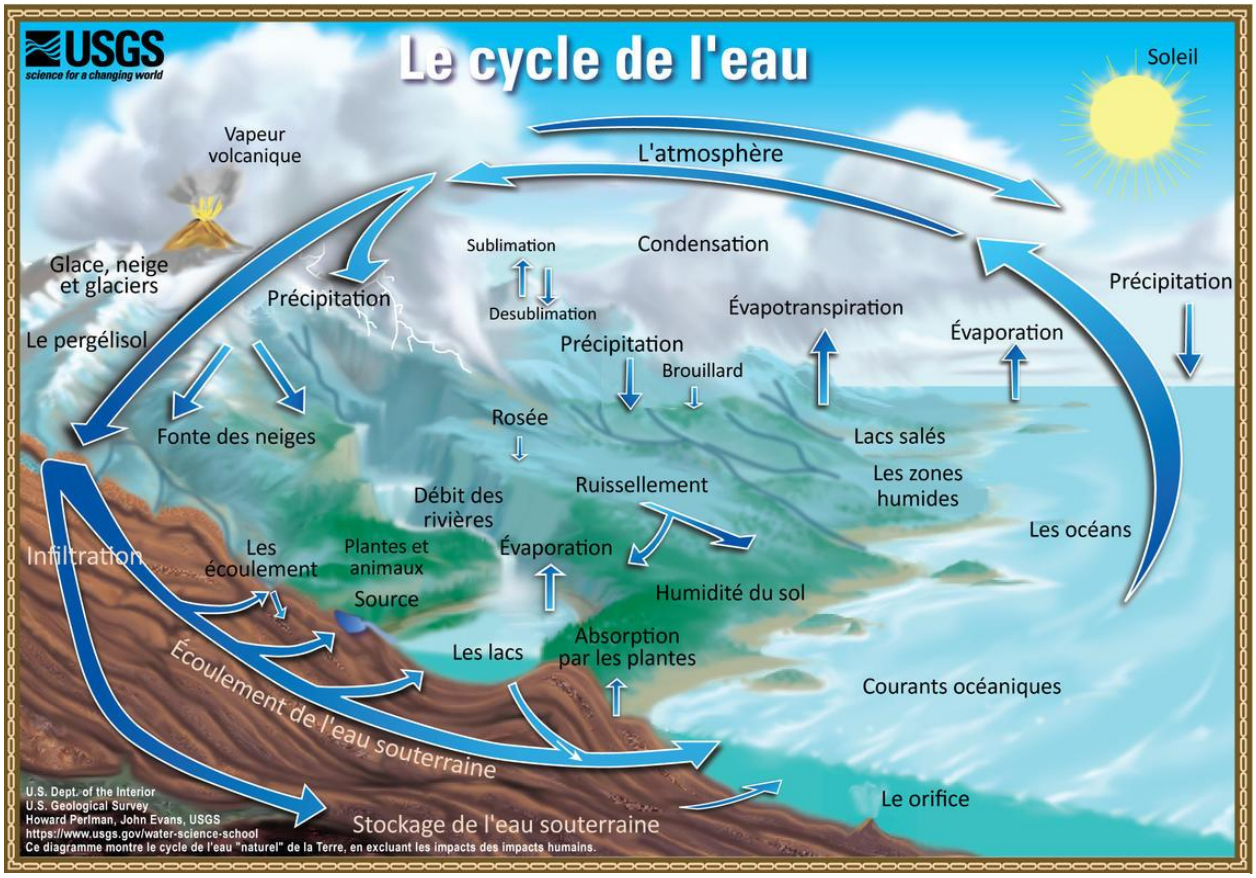

Figure 9. Hydrologic cycle representation showing relevant fluxes and storages (USGS).

Hydrological modeling serves two key functions (Fleming and Brauer, 2018):

The production function that distributes precipitation among various hydrological processes, such as infiltration, runoff, evapotranspiration, and soil storage.

The transfer function (routing) which transfers the water determined by the production function to the stream. It transforms net rainfall and shapes the flood hydrograph at the watershed outlet.

Numerous hydrological models have been developed. This research focuses specifically on deterministic, conceptual, and semi-distributed models.

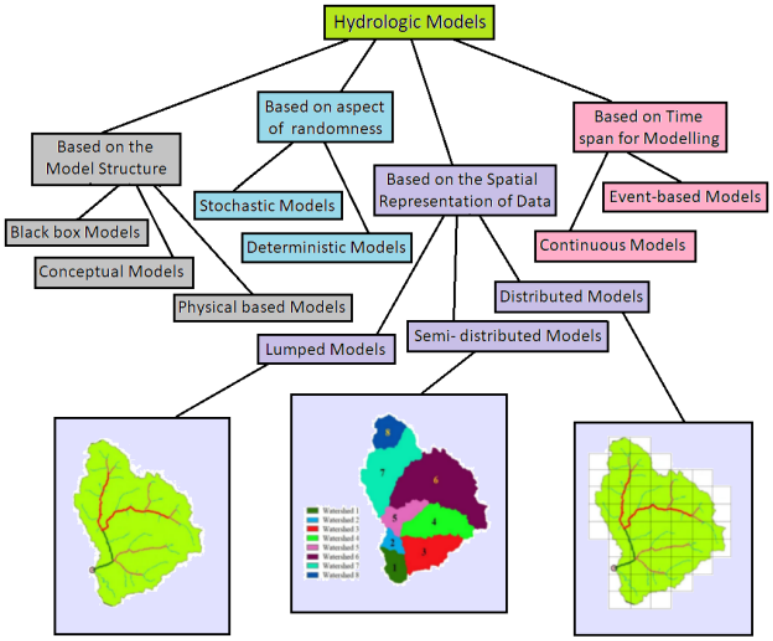

Figure 10. General classification of hydrological models (Godara, 2019).

Conceptual models also referred to as parametric or grey-box models represent watersheds as a series of interconnected storages or reservoirs, such as soil moisture, groundwater, and surface water. Mathematical equations depicting simplified physical processes manage hydraulic movement between these storages. Conceptual models are generally denoted as more flexible than strictly physically-based models, since parameters are estimate by calibrating model output to observed stream flow data. They are frequently perceived as a compromise between the complexity of physically-based models and the simplicity of empirical models. An essential aspect of a conceptual model involves comprehending the processes of water inflow and outflow movement within the system. Among conceptual hydrologic models, Hydrologic Engineering Center's Hydrologic Modeling System (HEC-HMS) and Soil and Water Assessment Tool (SWAT) are two of the most extensively used (Feldman, 2000; Godara and Bruland, 2019; Jaiswal et al., 2020).

The field of hydrological modeling has been thoroughly examined by researchers in Algeria and internationally through multiple studies (Hadour et al., 2020; Hu et al., 2020; Makhlouf Adel et al., 2021; Iqbal et al., 2022; Allali et al., 2023; Masood et al., 2023). Common objectives for research

studies include identifying and modeling phenomena, reviewing industry practices, and developing conceptual frameworks to address complex issues.

Hadoura et al. (2020), evaluated the sensitivity of hydrological parameters to future climate change in North-West Algeria, particularly in the Cheliff, Tafna, and Macta river basins. ANRH Meteorological data, estimated potential evapotrenspiration (PET) estimated by Thornthwaite method and climatic data from CNRM-CM5 model were implimented in GR2M hydrological model. Results exhebited decrease in both precipatation and discharge between 1970 and 1999. However, PET increased with the increase of temperature. Projections indicated a continued decrease in Winter discharges in the future, with varying trends in other seasons.

Hu and Shrestha (2020), focused on how (LULC) changes between 2001 and 2011 in the Richland Creek Watershed (RCW) in the St. Louis Metropolitan Area impact stream peak discharges. They HEC-HMS model coupled with Arc Hydro and HEC-GeoHMS to assist in predicting flash flooding and mitigating property damages. HEC-HMS models was successfully calibrated and validated simulating efficiently rainfall-runoff transformation process. The model performance using Nash-Sutcliffe Efficiency values were satisfactory. The results linked the increase in peak discharge to an increase in in impervious surfaces from 2001 to 2011.

Khouas et al. (2021), used HEC-GeoHMS, to model a watershed in Algiers, Algeria, considering hydrological, morphometric, and physical characteristics of the area. In addition, the hydrological response was evaluated using HEC-HMS. Their objective was to improve urban resilience by studying the watershed's response to hydro-meteorological hazard and implement better flood Risks protocols.

Iqbal et al. (2022), investigated the combined and individual impacts of land-use changes and climate change on the hydrological processes in subbasins of the Source Region of the Yellow River (SRYR) in China. The study utilized statistical methods and SWAT hydrological modeling based on land-use maps for the period 1990 and 2010, and climate periods 1976–1995 and 1996–2014. Findings reveals that that climate change has a greater influence on hydrological processes in all subbasins of the SRYR than land-use changes. Climate is expected to be warmer and wetter. Land-use changes within sub-basins witnessed distinct spatial transformations. The combined impacts of climate and land-use changes are more noticeable in certain sub-basins, affecting runoff and evapotranspiration.

Allali et al. (2023), analyzed the impact of land use change on river runoff in the Wadi Ouahrane watershed in northwestern Algeria using HEC-HMS hydrological modeling. The curve number (CN) sensitivity evaluation was conducted, demonstrating its significance as the most influential factor impacting watershed hydrology. LULC analysis depicted an increase in that cultivated land and built-up areas, while forest and grassland areas decreased in the watershed. The peak discharge in 2017 increased by 68% compared to the peak discharge in 1987, indicating the impact of land use changes on hydrological processes.

Masood et al. (2023), quantified the impacts of climate and land cover changes on the hydrological regime of the Khanpur dam catchment area. HEC-HMS model was utilized in their study to forecast the hydrological impact of precipitation, analyze land cover and climate changes, and evaluate their potential impact at the Khanpur Dam. The HEC-HMS model demonstrated reliable performance in simulating actual flow and forecasting anticipated flows under different socioeconomic pathways.

In conclusion, this chapter highlights the significant influence of climate and land use/land cover (LULC) changes on rainfall-runoff modeling and discharge dynamics. These factors critically affect the occurrence and intensity of floods and extreme events. Therefore, it is essential to integrate them into hydrological modeling frameworks and conduct thorough studies to quantify their isolated and combined impacts. This approach will enhance our understanding of hydrological responses, improve flood prediction accuracy, and contribute to more effective water resource management and disaster mitigation strategies.

Chapter II: Basin Study.

Study Area

The Kebir river catchment is located in the North-East of Algeria, between (36°32′13.42″N to 36°35′0.21″N latitudes and 7°3′45.87″E to 7°18′19.47″E longitudes). The research area is included in the Constantinois coastal basins and covers 1136.50 km^2. Skikda city owns 80% of this surface area, with Guelma city owning the remaining 20% (**Figure 11**).The altitude ranges from 29 to 1201 m. The rainfall can be characterized as heavy and irregular. The mean annual rainfall of Skikda city is about 720 mm. The study area lies in the subtropical Mediterranean region, characterized by a warm and dry summer and a relatively mild and wet winter.

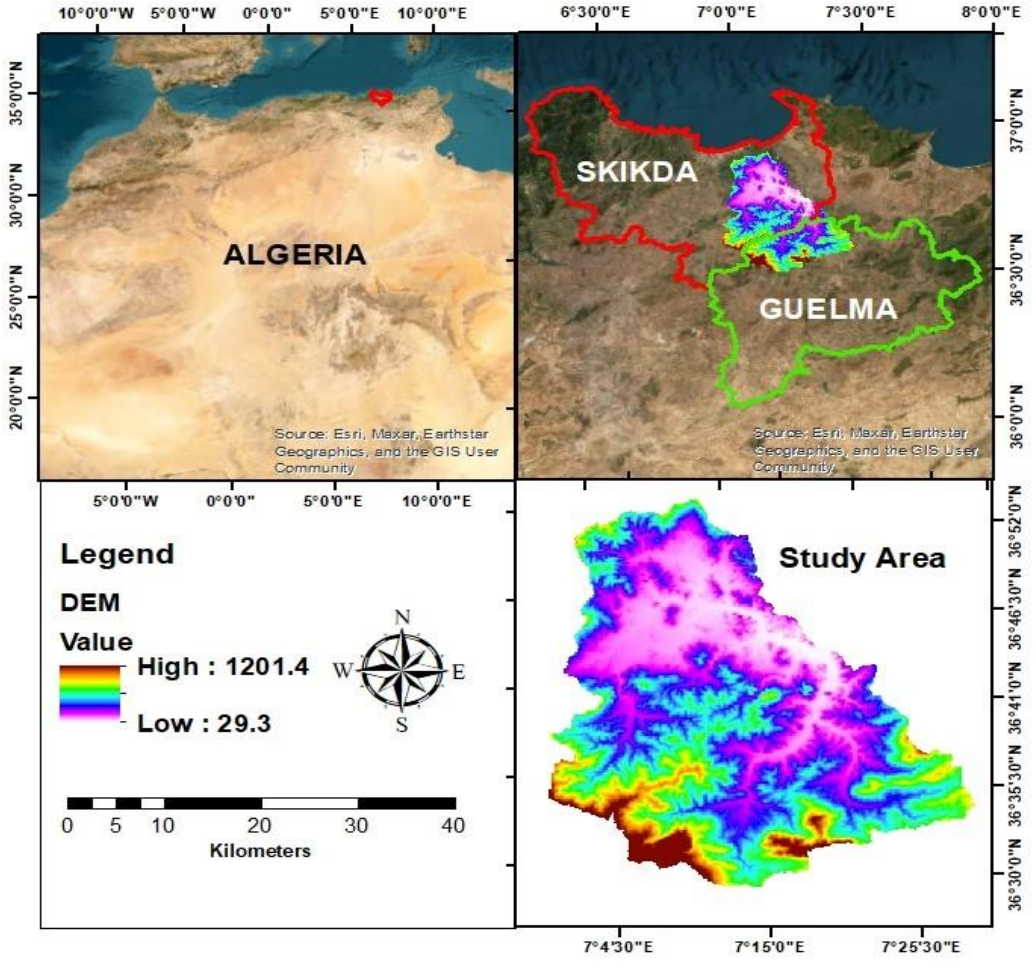

Figure 11. The study area of Kebir river catchment.

Hydrographic Network

The KRC flow pattern is known as endorheic in northeastern Algeria. The hydrographic network in this region is significantly influenced by geological features and has helped to drive urban development over time. The flows through Ain Charchar province and is supplied by many medium-depth intermediate (**Figure 12**). The Mouger Wadi and Ghrara Wadi serve to fill the Zit Emba dam.

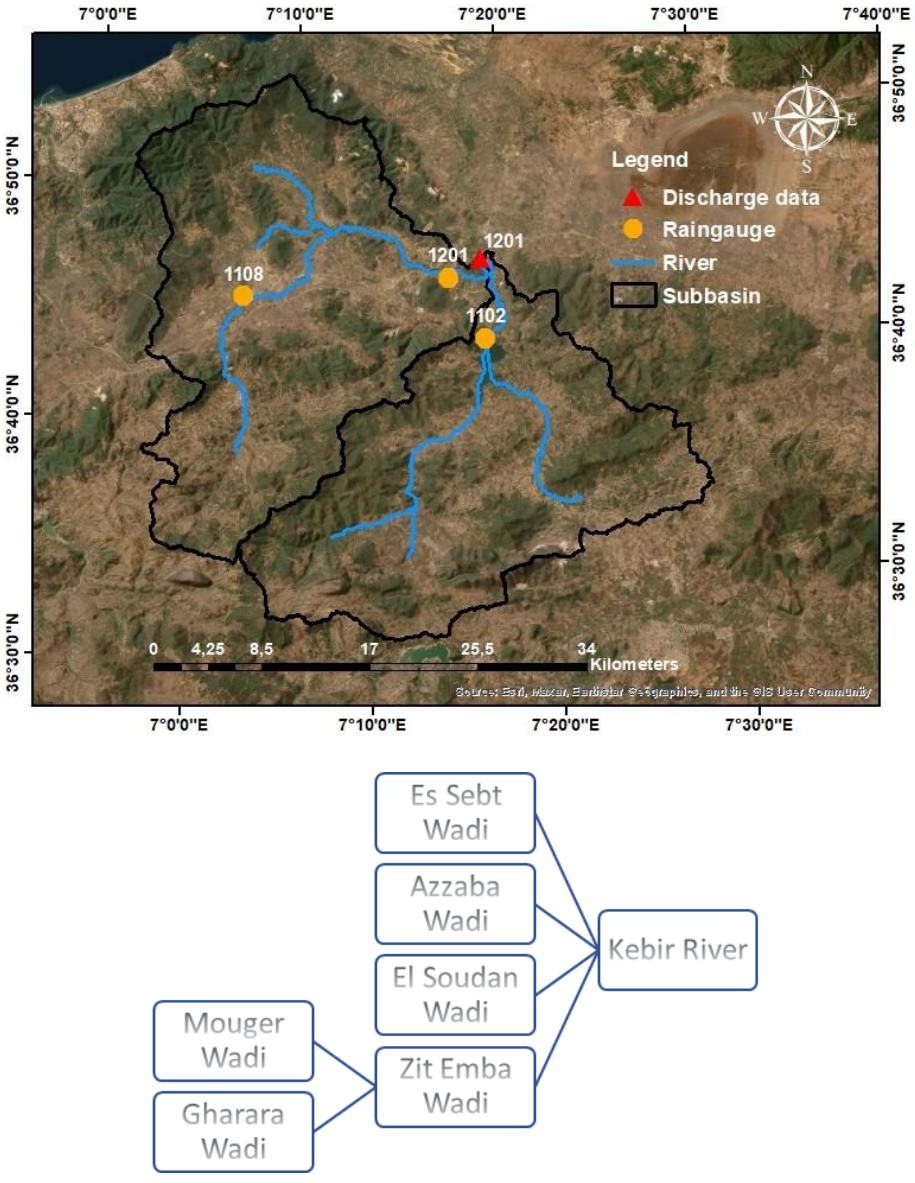

Figure 12. Kebir River tributuaries.

Data Acquisition

The list of climatic, hydrological and topographic data used in this study are given in **Table 1**.

Table 1. The catalogue of datasets utilized in this research.

Category	Data	Source
Meteorology	Precipitation Temperature,	The National Agency for Hydraulic Resources (ANRH)
Hydrology	Discharge	
Climatic	RCM	Coupled Model Intercomparison Project Phase 5 (CMIP5) (https://cds.climate.copernicus.eu/).
Topography	Digital Elevation Model (DEM)	Shuttle Radar Topography Mission (SRTM - 30m spatial resolution) (https://earthexplorer.usgs.gov/)
Soil	Digital soil maps	Global Hydrologic Soil Groups (HYSOGs250m)
Land-use	Land-use data for chosen periods	Processed Landsat TM/ETM remote sensing images (https://earthexplorer.usgs.gov/)

Meteorology and Hydrology Data

The ANRH dataset provided meteorological data for mean daily temperatures, precipitation, and runoff records for the period 1970-2010. Meteorological data were provided by three stations: Ain Charchar (1201), Azzaba (1108), Zit Emba (1102). Standard statistical procedures were used to maintain the uniformity and consistency of time series data, via Hydrolab, on portions of the record, thus allowing for trend and climate change analysis. However, during the periods from December 18, 1984, to July 31, 1985, and January 1, 2003, to July 31, 2003, the ANRH dataset remained unchanged, and no standard statistical approaches were used to fill any gaps in the time series. These periods represent instances where the data remained existent and complete, providing a reliable basis for hydrological analyses.

RCM Data

Regional climate models (RCMs) were initially developed as a method of dynamical downscaling from Global Climate Models (GCMs) to bridge the spatial gaps between GCMs and other modeling components. This downscaling is required to offer precise representations of physical processes, high spatial resolution, land-sea contrast, and land use necessary for hydrological models (Wang

et al., 2004; Foley, 2010). Numerous Coordinated Regional Climate Downscaling Experiment (CORDEX) include different simulated combinations of RCMs driven by various GCMs and emission pathways, providing a comprehensive view of future climate projections (Giorgi et al., 2009; Yeboah et al., 2022). However, GCMs and RCMs often exhibit systematic errors, known as biases, in their output. To address these biases, various bias correction methods have been developed, aiming to reduce the disparity between observed and simulated climatic variables. (Teutschbein and Seibert, 2012; Bai et al., 2019). Bias correction methods provided by CMhyd, are used in this study to correct climate change projection models for precipitation and temperatures (min and max) variables. In addition, two emission scenarios in Coupled Model Intercomparison Project Phase 5 (CMIP5), mentioned by the Fifth Assessment Report (AR5) (Shukla et al., 2019), are implemented for forecasting future climate changes. The Representative Concentration Pathway (RCP) intermediate emission scenario 4.5 and high emission scenario 8.5, which are characterized by the radiative forcing values of 4.5 and 8.5 W/m2 produced by CO2 emissions, respectively, by the end of the 21st century (San José et al., 2016).

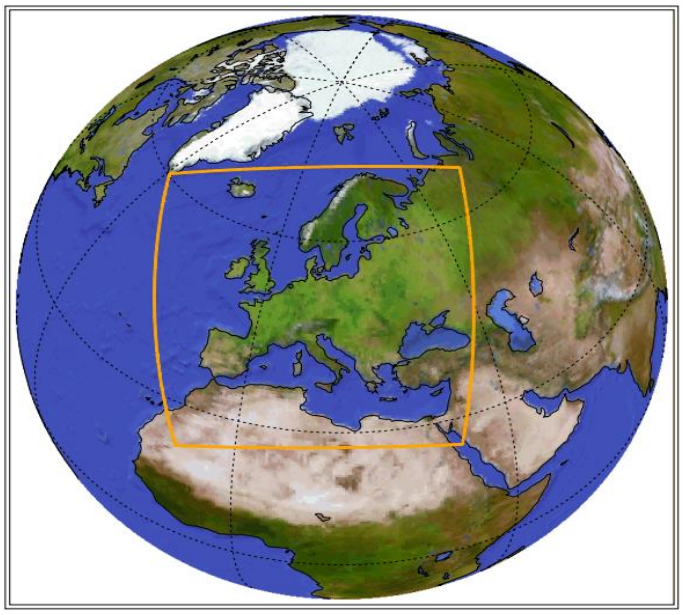

Figure 14. Europe-CORDEX (WRCP, 2015).

Daily precipitation, as well as maximum and minimum temperatures, were analyzed using RCA4 (RCM) judged adequate for the Algerian region for the period 1970–2005 (Derdour et al., 2022).The RCM RCA4 is driven by CNRM-CERFACS-CM5 (GCM) from Europe-CORDEX

(**Figure 14**), operating at a high resolution of 12 km (0.11◦). The entire set of data is sourced from the data portal accessible at (https://cds.climate.copernicus.eu/). Furthermore, future scenarios for the period 2020 to 2060 under two emission pathways (RCP4.5 and RCP8.5) were considered to project potential changes in rainfall and temperature, facilitating impact assessments. It is critical to note that including additional climate projection data might help understand the variability in projected stream flow.

Table 2. Regional climate models (RCMs).

Domaine	Resolution	Ensemble	RCM-GCM	Historical	RCP	
					4.5	8.5
EUR-CORDEX	0.11° (12 km)	r1i1p1	RCA4-CNRM-CERFACS-CM5	X	X	X

Topographic Data

Digital Elevation Model (DEM) at a 30m resolution data was obtained from the Shuttle Radar Topography Mission (SRTM). It was subsequently used through the medium of Hec-GeoHMS tools (ArcGIS) to delinate the boundaries of the subabasin Oued El Kebir (**Figure 1**).

Land-Use Data

The LULC maps for the dates 17/01/1985, 19/05/2003, and 27/12/2020 were generated from the processing of Landsat 5 TM and Landsat 7 ETM+ satellite data. The data were obtained through the Earth Explorer data portal (https://earthexplorer). The selection of Landsat satellite image was mainly influenced by the image quality, prioritizing days with minimal or low cloud cover. Each Landsat was georeferenced to the WGS_84 datum and Universal Transverse Mercator Zone 32 North coordinate system.

LULC classification was done in 1985, 2003, and 2020 using the most common supervised method for quantitative analysis of remote sensing image data (Richards and Jia, 2006). The maximum likelihood method in ArcGIS divided LULC into five categories: built-up lands, agricultural lands, forests, water bodies, and barren lands (**Figure 15**).

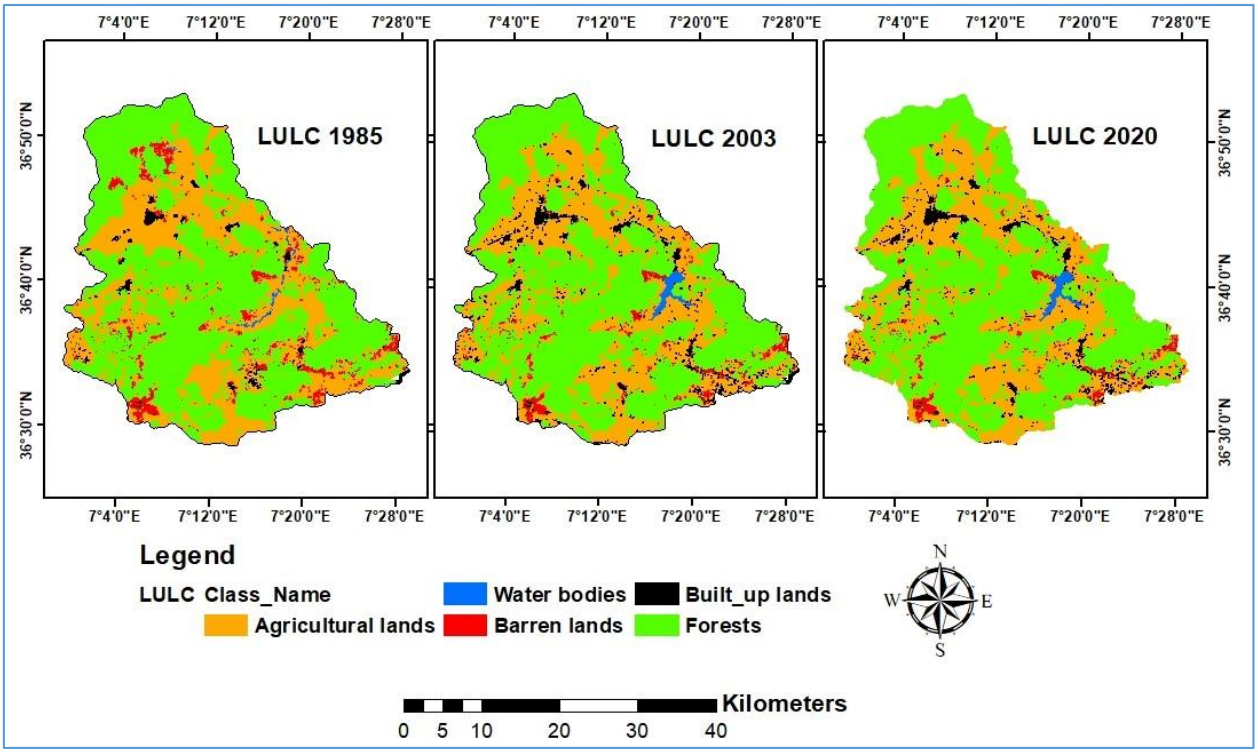

Figure 15. LULC map of the Kebir river catchment of the years of 1985, 2003 and 2020.

Soil Data

Soil cover data were obtained from the Global Hydrologic Soil Groups (HYSOGs250m) for Curve Number-Based Runoff Modeling (Ross et al., 2018). Classification of Hydrologic Soil Groups (HSG), which is used for the SCS method in hydrologic modeling, was derived from soil texture classes and depth to bedrock provided by the Food and Agriculture Organization (FAO - soilGrids250m) system. This categorizes all soil classes into four groups lettered from A through D/D.

Table 3 summarizes indicating runoff potential, infiltration rate, and texture for each group. The soil cover for KRC was categorized into B, C, C/D and D/D groups. Group C soil covered 82.20% of the research area as shown in **Figure 16**

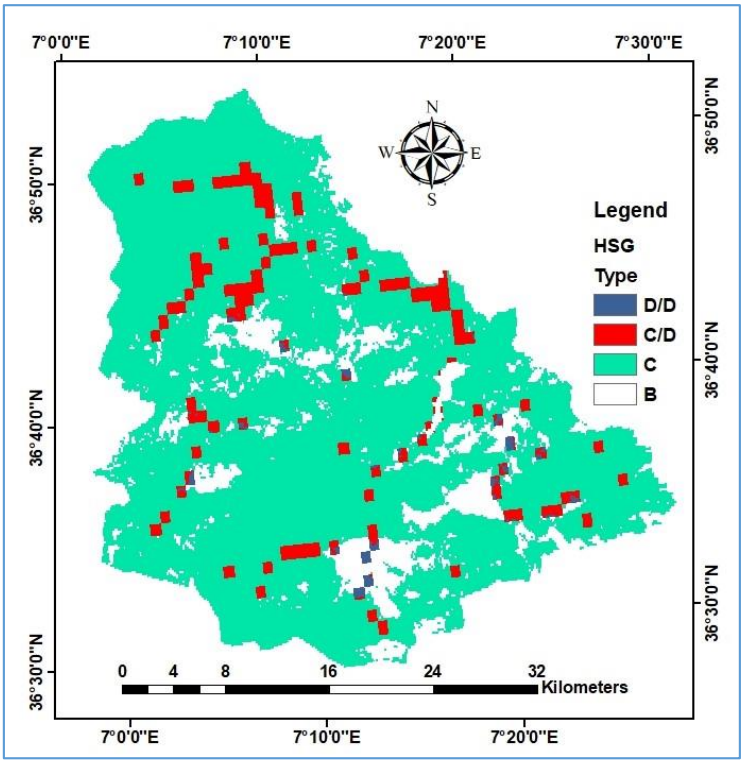

Figure 16. Types of Soil Cover present in KRC.

Table 3. Summarized description of Hydrologic Soil Groups (HSG) (Neilsen and Hjelmfelt, 1998; Ross et al., 2018).

Pixel values	Description	Soil texture class	Runoff potential	Infiltration potential
2	HSG-B	Sandy loam, Loamy sand (50-90% sand and 10-20% clay)	Moderately low runoff potential	Moderate
3	HSG-C	Clay loam, Silty clay loam, Sandy clay loam, Loam, Silty loam, Silt (<50% sand and 20-40% clay)	Moderately high runoff potential	Moderate to Low
13	HSG-C/D	Clay loam, Silty clay loam, Sandy clay loam, Loam, Silty loam, Silt (<50% sand and 20-40% clay)	High runoff potential unless drained	Low
14	HSG-D/D	Clay, Silty clay, Sandy clay (<50% sand and >40% clay)	High runoff potential unless drained	Low

Chapter III: Methodology

The methodology employed in this study encompasses multiple procedures and applications. To clarify the thought process underlying this work, the flowchart in (**Figure 17**) should be consulted, as it summarizes the processes and steps undertaken.

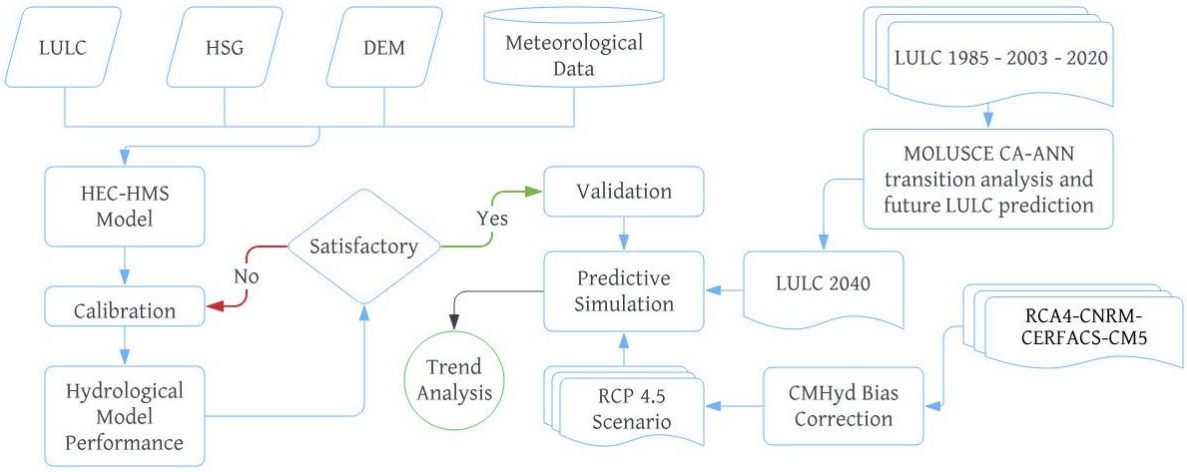

Figure 17. Flowchart of the methodology.

LULC Change Analysis

LULC classification and mapping

The ArcGIS spatial analyst tool provides users with Maximum Likelihood algorithm, a computational machine learning-based method in various remote sensing application, especially for detecting LULC classes (Abbas and Jaber, 2020). Maximum likelihood (ML) classification is a supervised statistical classification approach where pixels or cells are designated a signature during the training phase. Remaining cells are then assigned to the class with the highest likelihood on the signature identification based on Bayes' theorem (Agus et al., 2023). The signature identification used in this study included five classes: built-up lands, agricultural lands, forests,

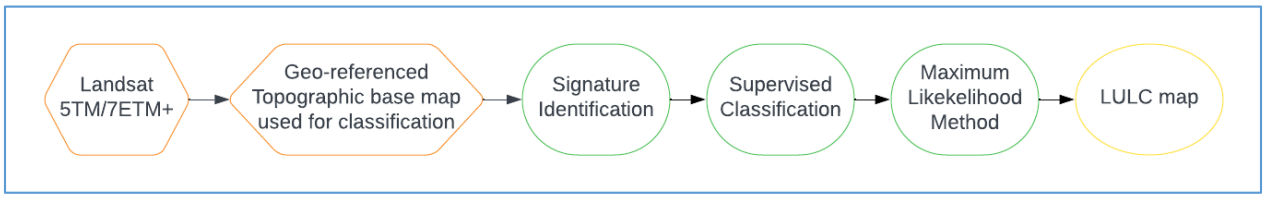

Figure 18. Classification of LULC.

water bodies, and barren lands. The classification process is depicted in **Figure 18**, while the LULC maps are illustrated in **Figure 15**.

LULC Change modelling

The modules for land use change simulation and evaluation (MOLUSCE) plugin within QGIS software was used as a land change modeler (LCM) to simulate changes in LULC (Satya et al., 2020; Blissag et al., 2024) within KRC and predict future land maps. MOLUSCE, developed by the Asia Air Survey in 2012, is an open-source plugin used for QGIS version 2.0 and later to analyze LULC condition, model spatial and temporal transitions, and predict future LULC change (Kulithalai S. S. and Deka, 2022). The MOLUSCE plugin runs four models: Artificial Neural Networks (ANN), Logistic Regression (LR), Multi-Criteria Evaluation (MCE), and Weights of Evidence (WoE). This plugin relies on steps including, inputs definition, evaluating correlation, area change assessment, transition potential modelling, Cellular Automata (CA) simulation and validation. This study used Artificial Neural Network Multi-Layer Perceptron (ANN-MLP) to assess spatiotemporal changes, generate LULC change maps, and compute the LULC transition from 1985 to 2003 and from 2003 to 2020. We employed the Cellular Automata Artificial Neural Network (CA-ANN) approach, a hybrid approach that accurately predicts changes by estimating the values of pixels based on their initial values and those of their neighboring pixels (Islam et al., 2023), to describe transition potentials and simulate the projected LULC changes by the year of 2040. For prediction accuracy validationof the model, the MOLUSCE plugin provides a Kappa validation approach and a comparison of reference and projected LULC maps. (**Figure 19**).

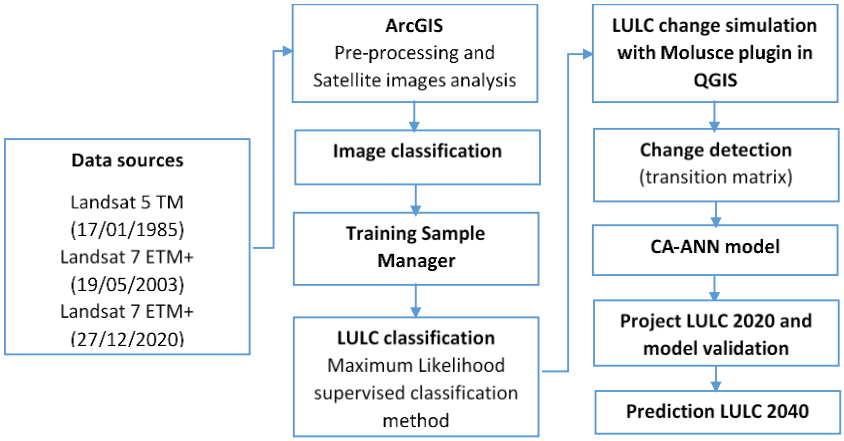

Figure 19. Methodology of predicting LULC changes in this study.

LULC change analysis and prediction

the primary objective of this part of the study was to determine the changes between the initial and final LULC maps and find the percentage of pixels that changed from one LULC to another.
In the process of ANN learning and training phase, the user must set a number of parameters, which are typically optimized through a trial-and-error process to find the best values. For this purpose, The model carried out 1000 iterations at a learning rate of 0.1, and parameters such as, 1×1 pixel neighborhood, 5 hidden layers and momentum value of 0.05 were set as the best optimized parameters for the model. Using the CA-ANN model, a prediction map of LULC changes for 2020 was made by incorporating spatial variables and LULC data from 1985 to 2003. In order to fit the model's training and validation samples, the projected LULC for 2020 was generated and compared to the reference LULC for 2020 produced via Landsat 7 ETM+ classification (**Figure 15**). Based on the validated model results observed during the accuracy assessment, we generated a LULC map for the year 2040 through an increased iterative process, using data from 2003 to 2020.

LULC Change accuracy assessment

LULC map definition and quantification relies on performing an accuracy assessment. It requires comparing the classification product with reference data. Thus, the predictions made by the trained CA-ANN model for 2020 are compared to a reference LULC map for 2020. The accuracy assessment of classified LULC was calculated using the confusion matrix and Kappa coefficient (Congalton, 2001). The Kappa coefficient was calculated using the following equation:

$$\boldsymbol{K = \frac{N\sum_{i=1}^{r} X_{ii} - \sum_{i=1}^{r}(X_{i+}).(X_{+i})}{N^2 - \sum_{i=1}^{r}(X_{i+}).(X_{+i})}} \quad \textbf{(1)}$$

where r is the rows number of the matrix, Xii is the number of observations in row i and column i (the diagonal elements), Xi+ and X+i are the marginal totals of row i and column i, respectively, and N is the number of the observations. The level of agreement based on the Kappa coefficient consists of poor agreement (< 0.4), moderate agreement (between 0.4< K< 0.8), and perfect agreement (>0.8) (Mishra and Rai, 2016).

Climate Data Generation

Bias correction

GCM and RCM models are gridded datasets that can be interpolated to the station point dataset using the station's latitude, longitude, and elevation at each gauge location. This process enables the extraction of historical and future climate model data for a specific location (Mengistu et al., 2023). However, it is important to highlight that these data may contain major biases stemming from systematic model shortcomings or spatial resolution issues (Teutschbein and Seibert, 2012). In this context, bias correction is required to minimize inconsistencies and deviations between observed and simulated climate variables on a daily time step (Hosseinzadehtalaei et al., 2021). Bias correction procedures adjust climate model output using a transformation algorithm, assuming the correction algorythme and parametrization validity for future conditions (Piani et al., 2010; Soriano et al., 2019). Climate Model data for hydrologic modeling (CMhyd) offers various bias-correction methods to correct and then extract simulated climate data (Rathjens et al., 2016). The bias-correction approaches used in this study are briefly outlined as follows.

Table 4. Bias-correction used for precipitation and temperature.

Variable	Precipitation	Temperature
Bias Correction	Distribution Mapping (DM)	Distribution Mapping (DM)
	Local intensity scaling (LOCI)	Linear scaling (LS)
	Power Transformation (PT)	Variance scaling (VS)

Distribution Mapping (DM)

Distribution mapping, also known as quantile-quantile mapping, is used to adjust the distribution of RCM outputs to match the distribution of observed data. This is achieved by fitting transfer functions of RCM-simulated data to that of observed data based on statistical measures such as mean, standard deviation and quantiles. DM adjusts simulated precipitation and temperature data to match observed data by assigning random values based on cumulative probabilities (Yeboah et al., 2022). These probabilities determine the selection of corrected values for both precipitation and temperature. The distribution mapping used in CMhyd is based on the gamma distribution, developed by (Thom, 1958). Where Γ is the Gamma function, α is the shape parameter, and β is the scale parameter.

$$f_\gamma(\chi|\alpha,\beta) = \chi^{\alpha-1}\frac{1}{\beta^\alpha \Gamma(\alpha)}e^{\frac{-\chi}{\beta}};\ \chi \geq 0;\ \alpha,\beta > 0 \quad (2)$$

Local intensity scaling (LOCI)

The LOCI method, developed by (Schmidli et al., 2006), was designed to upgrade the linear scaling method by introducing a threshold for wet-day precipitation. This approach effectively adjusts wet-day frequencies and intensities of precipitation, improving the raw data that often have too many drizzle days (Berg et al., 2012; Zhang et al., 2018b). The initial phase involves establishing the wet-day threshold for each month (Equations 3 and 4) This threshold corresponds to the precipitation level where the number of wet days in climate model simulations equals that in observed data. It is derived from the raw precipitation series to ensure alignment with observed wet-day frequencies.

$$P^1_{\text{control}}(d) = \begin{cases} 0, & \text{if } P_{\text{control}}(d) < P_{\text{th,control}} \\ P_{\text{control}}(d) & \text{, otherwise} \end{cases}$$
$$P^1_{\text{scenario}}(d) = \begin{cases} 0, & \text{if } P_{\text{scenario}}(d) < P_{\text{th,control}} \\ P_{\text{scenario}}(d), & \text{otherwise} \end{cases} \quad (3,4)$$

where $P^1_{\text{control}}(d)$ is the transitional daily precipitation during the control period; $P^1_{\text{scenario}}(d)$ is the same during the future period; $P_{\text{control}}(d)$ is the original daily precipitation during the control period; $P_{\text{scenario}}(d)$ is the same during the future period; $P_{\text{th,control}}$ is the threshold.

The second step resumes with the calculation of a scaling factors using Equation (5) to ensure that the mean (μ_m) of adjusted precipitation matches the observed data.

$$S = \frac{\mu_m\left(P_{\text{observed}}(d)|P_{\text{observed}}(d)>0\text{ mm}\right)}{\mu_m\left(P_{\text{control}}(d)|P_{\text{control}}(d)>P_{\text{th,control}}\right)-P_{\text{th.control}}} \quad (5)$$

Finally, Equations (6) and (7) are used to rectify the control and scenario precipitations, respectively.

$$\boldsymbol{P^{*}_{\text{control}}(d) = P^{1}_{\text{control}}(d) \cdot s} \quad \textbf{(6)}$$

$$\boldsymbol{P^{*}_{\text{scenario}}(d) = P^{1}_{\text{scemario}}(d) \cdot s} \quad \textbf{(7)}$$

where $P^{*}_{\text{control}}(d)$ is the corrected daily precipitation during the control period; $P^{*}_{\text{scenario}}(d)$ is the same during the future period.

Power Transformation (PT)

Power Transformation is a non-linear method used to adjust the mean (μ_m) and variance (σ_m^2) in data. It involves applying an exponential correction factor (aP^{b_m}) to modify the standard deviation of RCM simulations (Mendez et al., 2020). The scaling 'b_m' is determined by aligning the Coefficient of Variation (CV_m) of corrected RCM precipitation with observed precipitation values for each month.

$$\boldsymbol{f(b_m) = 0 = CV_m\left(P_{\text{observed}}(d)\right) - CV_m\left(P^{b_m}_{\text{control}}(d)\right)} \quad \textbf{(8)}$$

$$\boldsymbol{\frac{\sigma_m\left(P_{\text{observed}}(d)\right)}{\mu_m\left(P_{\text{observed}}(d)\right)} - \frac{\sigma_m\left(P^{b_m}_{\text{control}}(d)\right)}{\mu_m\left(P^{b_m}_{\text{control}}(d)\right)} = 0} \quad \textbf{(9)}$$

The Power Transformation then aligns the observed precipitation $P_{\text{observed}}(d)$ with the intermediate series $P^{b_m}_{\text{control}}(d)$ using the LS approach. The corrected control ($P^{*}_{\text{control}}(d)$) and scenario ($P^{*}_{\text{scenario}}(d)$) precipitation datasets are then produced as follows.

$$\boldsymbol{P^{*}_{\text{control}}(d) = P^{b_m}_{\text{control}}(d) \cdot \left[\frac{\mu_m\left(P_{\text{observed}}(d)\right)}{\mu_m\left(P^{b_m}_{\text{control}}(d)\right)}\right]} \quad \textbf{(10)}$$

$$\boldsymbol{P^{*}_{\text{scenario}}(d) = P^{b_m}_{\text{scenario}}(d) \cdot \left[\frac{\mu_m\left(P_{\text{observed}}(d)\right)}{\mu_m\left(P^{b_m}_{\text{control}}(d)\right)}\right]} \quad \textbf{(11)}$$

Linear scaling (LS)

The Linear Scaling method adjusts the mean value of RCM simulations to match observed data. It scales precipitation in control and scenario simulations based on the ratio of long-term monthly mean observed and simulated data. This method is effective when monthly mean values are available (Teutschbein and Seibert, 2012; Zhang et al., 2018b). The method involves subtracting the mean observed temperature from the mean simulated temperature for each month, creating an additive term that is applied to adjust the simulated daily temperatures. This ensures alignment of the long-term monthly means between corrected and observed temperatures.

$$\boldsymbol{T^{*}_{\text{control}}\,(d) = T_{\text{control}}\,(d) + \left(\mu_m\left(T_{\text{observed}}\,(d)\right) - \mu_m\left(T_{\text{control}}\,(d)\right)\right)} \quad \textbf{(12)}$$

$$\boldsymbol{T^{*}_{\text{scenario}}\,(d) = T_{\text{scenario}}\,(d) + \left(\mu_m\left(T_{\text{observed}}\,(d)\right) - \mu_m\left(T_{\text{control}}\,(d)\right)\right)} \quad \textbf{(13)}$$

where, $T^{*}_{\text{control}}\,(d)$ and $T^{*}_{\text{scenario}}\,(d)$ are the corrected daily temperature in the corresponding month during the control and the future period, respectively; $T_{\text{control}}\,(d)$ and $T_{\text{scenario}}\,(d)$ are the raw daily temperature in the corresponding month during the control and the future period, respectively. $\mu_m\left(T_{\text{observed}}\,(d)\right)$ and $\mu_m\left(T_{\text{control}}\,(d)\right)$ are the observed and simulated monthly mean temperature in the corresponding month during the control and future period, respectively.

Variance scaling (VS)

The normal temperature distribution makes it difficult to modify variance using the PT approach. To overcome this issue, (Chen et al., 2011) presented a variance scaling technique. This method seeks to adjust the mean and variance of temperature time series in a sequential manner (Teutschbein and Seibert, 2012).

$$\boldsymbol{T^{*}_{\text{control}}\,(d) = \left[T_{\text{control}}\,(d) - \mu_m\left(T_{\text{control}}\,(d)\right)\right] \cdot \left[\frac{\sigma_m\left(P_{\text{observed}}\,(d)\right)}{\sigma_m\left(P^{*1}_{\text{control}}\,(d)\right)}\right] + \mu_m(T_{control}(d))} \quad \textbf{(14)}$$

$$\boldsymbol{T^{*}_{\text{scenario}}\,(d) = \left[T_{\text{scenario}}\,(d) - \mu_m\left(T_{\text{scenario}}\,(d)\right)\right] . \left[\frac{\sigma_m\left(P_{\text{obsened}}\,(d)\right)}{\sigma_m\left(P^{*1}_{\text{control}}\,(d)\right)}\right] + \mu_m(T_{scenario})} \quad \textbf{(15)}$$

where, $T^{*}_{\text{control}}(d)$ and $T^{*}_{\text{scenario}}(d)$ are the corrected daily temperature in the corresponding month during the control and the future period, respectively; $T_{\text{control}}(d)$ and $T_{\text{scenario}}(d)$ are the raw daily temperature in the corresponding month during the control and the future period, respectively. $\mu_m\left(T_{\text{scenario}}(d)\right)$ and $\mu_m\left(T_{\text{control}}(d)\right)$ are the corrected monthly mean temperature in the corresponding month during the control and future period, respectively.

Evaluation of Bias-Correction Methods

The performance of bias-correction methods was evaluated using time-series-based statistics, for the overlapped period (1970-2005), between observed and RCM-simulated historical data. Root mean square error (RMSE) and mean absolute error (MAE), were used, via XLSTAT, to asses the performance of each bias correction procedure. It is important to consider the limitations and uncertainties of bias correction techniques in hydrological modeling (Equations 16 and 17). However, bias-correction method that performs well in the historical case is expected to perform better for the future scenarios (Zhang et al., 2018b).The best bias-correction methods, LOCI for precipitation and VS for temperature, were used in the hydrological model for stream flow forecasting simulation.

$$\boldsymbol{RMSE} = \left(\frac{\sum_{i=1}^{N}\left(Q_{i,Obs}-Q_{i,Sim}\right)^{2}}{N}\right)^{\frac{1}{2}} \quad \textbf{(16)}$$

$$\boldsymbol{MAE} = \frac{\sum_{i=1}^{n} /Q_{i,Obs}-Q_{i,Sim}/}{n} \quad \textbf{(17)}$$

where $Q_{i,Sim}$ is the simulated discharge at time (t = i), $Q_{i,Obs}$ is the observed discharge at time (t = i), $\overline{Q}_{Obs}$ is the average observed discharge; N is the number of observations.

Hydrological Modelling

HEC-GeoHMS processing

Hydrologic Engineering Center's Geospatial Hydrologic Modeling Extension (HEC-GeoHMS) acts as link between ArcGIS and HEC-HMS. HEC-GeoHMS (or ArcHydro Tool) performs spatial analysis and divide the overall catchment into sub-catchments using Digital Elevation Model (DEM) when the outlet of the catchment is defined (USDA, 1986). All derived information and parameters database such as area extension, Curve number (CN), impervious friction, and Lag time become attributes of a catchment model HEC-GeoHMS creates.

In the Kebir River catchment, a hydrologic modeling approach is implemented in three main steps using HEC-GeoHMS and HEC-HMS (**Figure 20**).

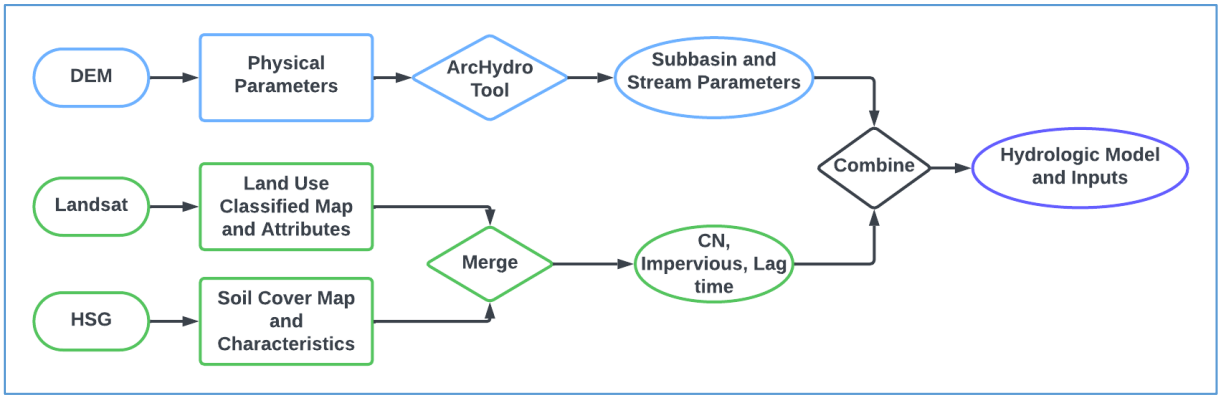

Figure 20. Hydrologic model generation process via HEC-GeoHMS.

*Subbasin and Stream Parameter Extraction: HEC-GeoHMS extracts subbasin parameters (basin slope, longest flow path, basin centroid, centroid elevation, and longest flow path elevation) and stream parameters (river length, upstream and downstream elevations, and river slope) from digital elevation models (DEM).

*Parameter Estimation and Model Development: HEC-GeoHMS uses these data, along with land use and soil data, to create model parameters (CN, lag time, and impervious) for each subbasin. The Soil Conservation Service Curve Number (SCS) and SCS unit hydrograph models use these parameters.

*Transfer to HEC-HMS: The preprocessed hydro-GIS inputs and parameters are transferred to HEC-HMS, a hydrologic modeling system, to simulate runoff and water quality processes in **Figure 21**.

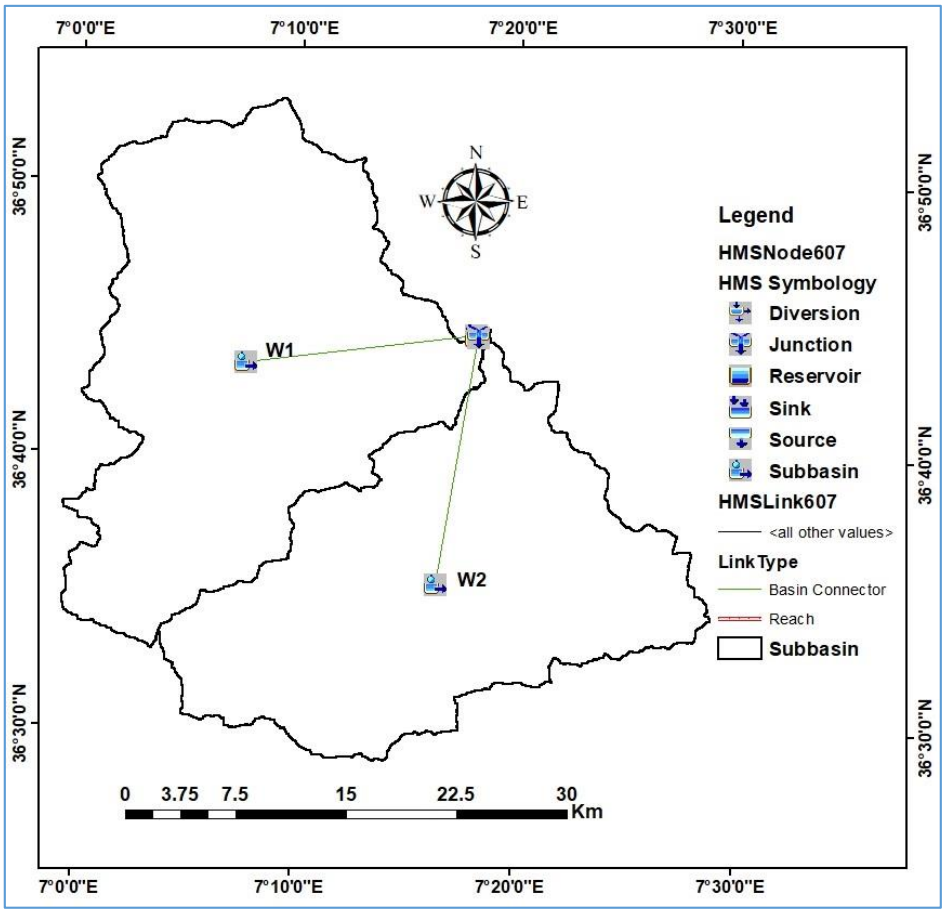

Figure 21. The Schematic Diagram of the HEC-HMS

HEC-HMS

Hydrologic Engineering Center - Hydrologic Modeling System (HEC-HMS) is an open software developed by the US Army Corps of Engineers. HEC-HMS uses meteorological and physical data of a watershed to perform hydrologic simulation for a period. These simulations can provide users with information about urban flooding, planning for flood frequency and early warning systems, stream restoration, etc. (Ford et al., 2008).

HEC-HMS reproduces similar runoff process as represented in **Figure 22**. This modeling approach incorporates various hydrological processes, including precipitation, surface runoff, base flow,

infiltration, and evapotranspiration, to simulate watershed dynamics. This project used HEC-HMS 4.11, following the flowchart as indicated in **Figure 17**.

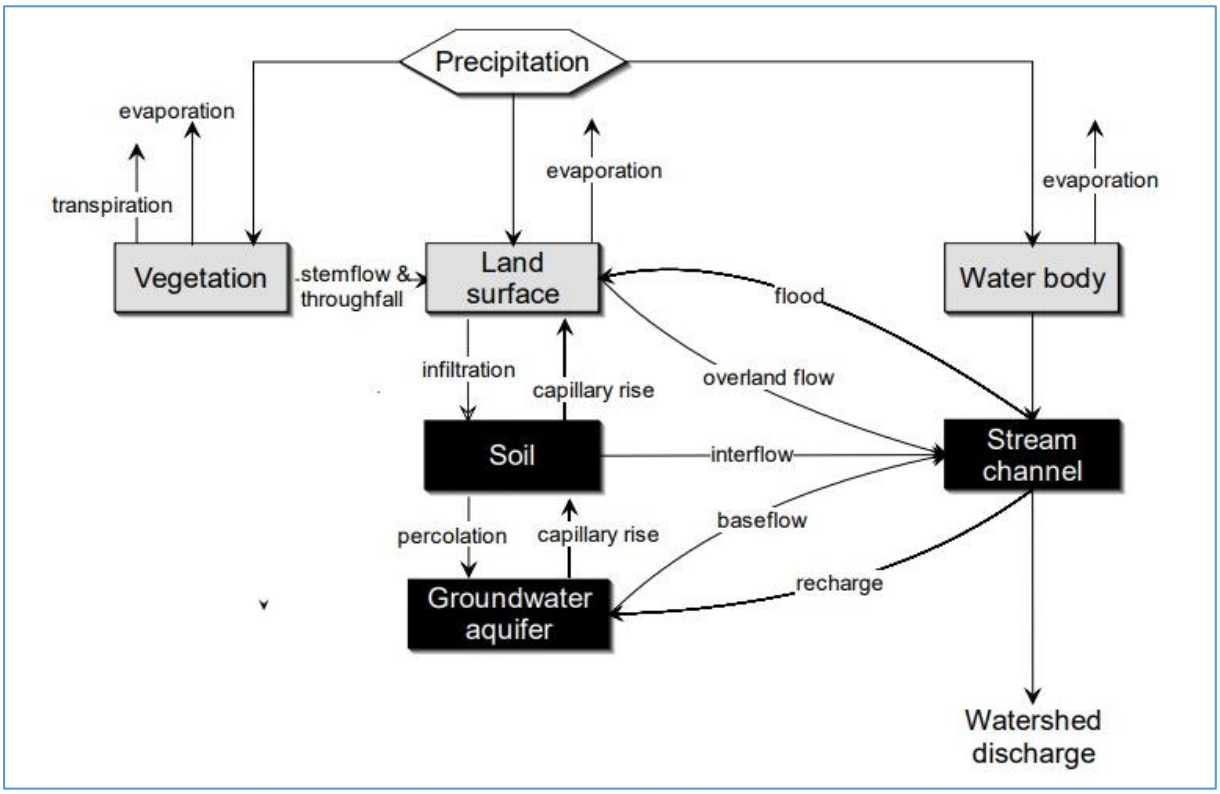

Figure 22. Diagram depicting Runoff Process (Feldman, 2000).

SCS loss method

HEC-HMS programs natural functions like interception, infiltration, storage, evaporation and transpiration as losses from the total precipitation. To predict discharge hydrographs and simulate the runoff volume using the HEC-HMS model, the transform method SCS unit hydrograph and Soil Conservation Service Curve Number (SCS-CN) was used KRC.

The SCS-CN method's extensive application as a transformation technique lies in its aptitude to estimate runoff volume resulting from rainfall events (Hawkins et al., 2019). This method relies on the determination of lag time (min) and calculates direct runoff based on factors such as total rainfall, land use, vegetation, and prior soil moisture conditions. This method uses the following equations (Feldman, 2000):

$$R = \frac{(P+I_a)^2}{(P-I_a+S)} \quad (18)$$

$$I_a = \lambda . S \quad (19)$$

$$S = \frac{25400}{CN} - 254 \quad (20)$$

where R is the direct runoff (mm), P is the total rainfall depth (mm), S is the potential maximum retention (mm), Ia is the initial abstraction (mm), λ is the initial abstraction ratio and CN is the curve number. The empirical value of λ is 0.2. suggested by (Mishra et al., 2006; Baltas et al., 2007).

Impervious and CN values, which are required as input parameters, are determined using LULC and hydrological soil groups (HSG) (**Figure 23** and **Figure 24**). Low soil infiltration leads to high Curve Number (CN) values, indicating the soil's inability to absorb large amounts of rainfall, which increases the potential for runoff. Conversely, high soil infiltration capacity results in low CN values (Xiao et al., 2011). **Table 5** summarizes the CN values gathered from the TR-55 (USDA, 1986) based on the study area's characteristics. Impervious areas in the KRC sub-basin are expressed as a proportion of the overall area.

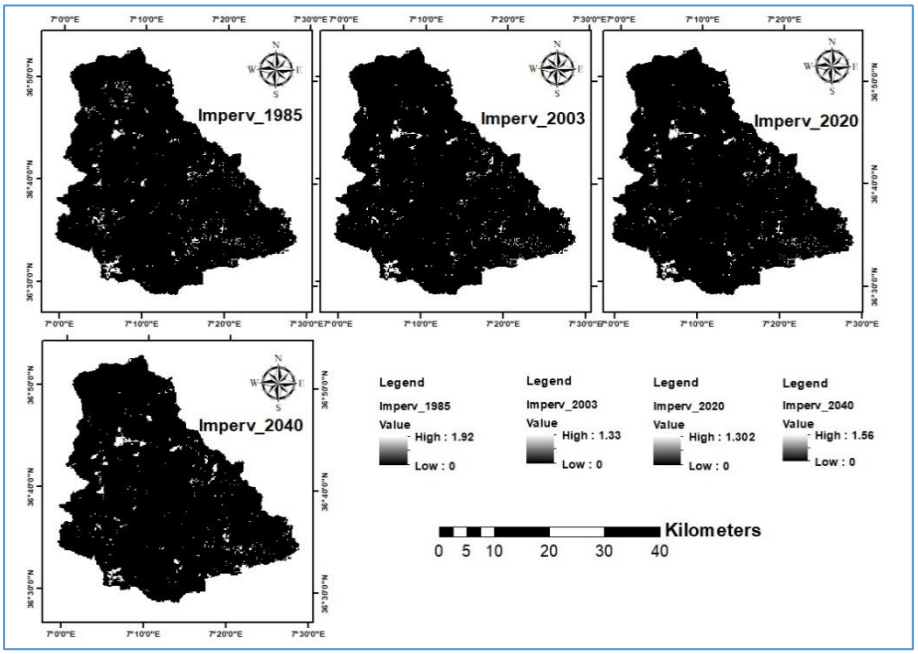

Figure 23. KRC Impervious Grid map.

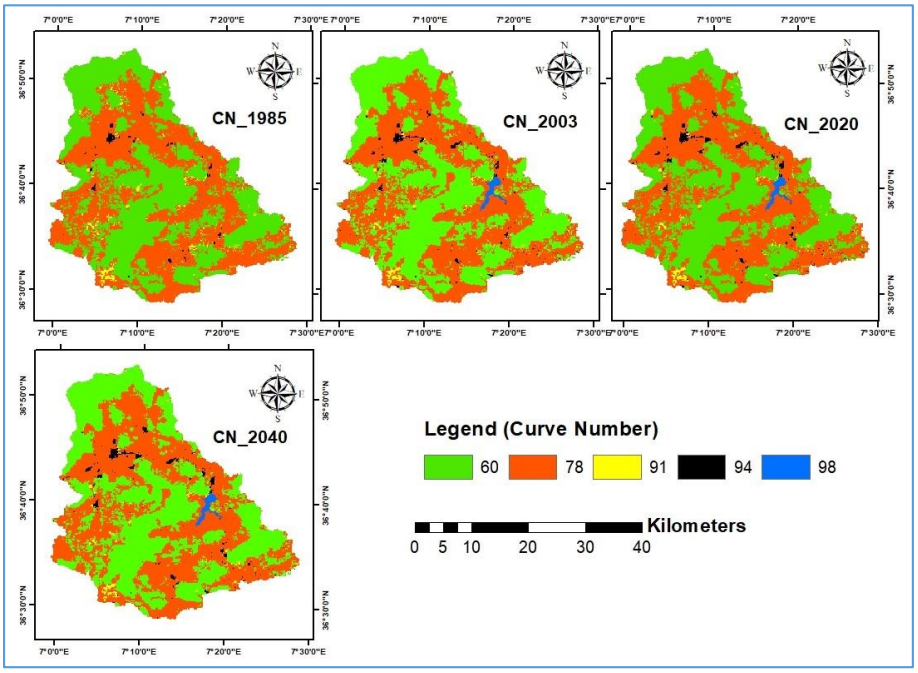

Figure 24. KRC CN Grid map.

Table 5. Runoff curve numbers relative to HSG (USDA, 1986).

Class Name	Description	CN			
		A	B	C	D
Agricultural lands	Land used for agriculture, crop fields, paddy field, fallow lands, vegetable lands, fruits, and other cultivated lands.	67	77	78	87
Water bodies	Rivers, lakes, ponds, reservoirs.	98	98	98	98
Barren lands	Bare and exposed soils, abandoned land, open space, landfill sites, construction sites.	77	86	91	93
Built-up lands	Residential, commercial, and industrial areas, isolated and clustered settlements, transportation, roads, services, urban areas.	94	94	94	94
Forests	Deciduous forest, mixed forestland, palms, orchard, herbs, climbers, gardens, recreational areas, grassland.	55	60	81	86

The composite CN value corresponding to soil classes B (silt loam or loam) and C (sandy clay loam) is determined as follows:

$$CN_{composite} = \frac{\sum(A_i * CN_i)}{\sum A_i} \quad \textbf{(21)}$$

where, Ai is drainage area for land use type and CNi is curve number for the same land use type.

SCS unit hydrograph method

The SCS unit hydrograph transform method computes the response of a watershed to a specific rainfall event, representing the runoff generated from excess rainfall. While excess rainfall and runoff are not directly proportional, they are interconnected. Excess rainfall, refers to the portion of precipitation that does not infiltrate into the soil or evaporate and is generally considered uniformly distributed over time and space within a watershed under ideal conditions. Direct runoff, however, is dependent of time and moisture. It is characterized by a lag time before reaching the stream network and is the part of excess rainfall that reaches streams and rivers driven by saturation excess and infiltration excess mechanisms (Ekeroth, 2022). The SCS unit hydrograph method uses excess rainfall hyetograph resulting from removing infiltration and interception losses of the total rainfall hyetograph as a mean to quantify the runoff hydrograph. Hence, lag time and curve number both computed previously via Hec-GeoHMS are required to generate a runoff hydrograph.

The resulting runoff hydrograph from this model uses following equations for its time of peak and peak of unit hydrograph (Feldman, 2000):

$$\begin{cases} \boldsymbol{U_p = 2.08\ \frac{A}{T_p}} \\ \boldsymbol{T_p = \frac{\Delta t}{2} + 0.6 T_c} \end{cases} \quad \textbf{(22)}$$

where Up is peak of unit hydrograph, A is the watershed area, Tp is time of peak and Δt is excess precipitation duration.

Muskingum routing method

Flood routing is a mathematical method for predicting the flood wave magnitude and celerity changes of a flood wave as it propagates down rivers or through reservoir. Muskingum routing process is determined by assigning values to the proportionality coefficient (K) and weighting factor (x), which are influenced by a river's physical properties such as channel roughness, length, slope, form, and flow upstream and downstream. The Muskingum method is a popular lumped flow hydrologic routing technique. Developed by McCarthy (1938), Muskingum routing represents a channel's storage as a function of both inflow and outflow discharge (Baláž et al., 2010; Song et al., 2011).

Muskingum routing storage, inflow and outflow is represented as (Feldman, 2000):

$$\boldsymbol{S = K(xI + (1 - x)O)} \quad \textbf{(23)}$$

where, S is the watershead storage, K represents travel time of flood wave through reach, x is dimensionless weight ranging $0 \leq x \leq 0.5$, I is the inflow and O representing the outflow is calculated as:

$$O_t = \left(\frac{\Delta t - 2Kx}{2K(1-x)+\Delta t}\right) I_t + \left(\frac{\Delta t + 2Kx}{2K(1-x)+\Delta t}\right) I_{t-1} + \left(\frac{2K(1-x)-\Delta t}{2K(1-x)+\Delta t}\right) O_{t-1} \quad (24)$$

where O_t is iteratively determined based on inflow (I_t and I_{t-1}), initial condition (O_t=0), K, and x.

Model Calibration, Validation and Forecasting

Calibration and validation were performed for KRC, to accurately estimate parameters used for rainfall-runoff simulation. To develop a calibrated and validated model, observed discharge data are required for the optimization of the model. Due to the lack of complete observed discharge data for the whole periode 1970-2010, a HEC-HMS model was calibrated in the period 18/12/1984 - 31/12/1985 and validated in the period 01/01/2003 - 31/12/2003. The focus was to obtain the peak flow and runoff volume at the outlet of KRC for rainfall events during selected years. The HEC-HMS is calibrated by identifying an optimal set of parameters minimizing the sum of squared residuals between observed and simulated hydrologic data. This study chooses the Univariate Gradient (UG) method, which provides accurate results (Feldman, 2000). Following the previous approach, peak flow and runoff volume for 2020 and 2040 were forecasted applying two RCP scenarios (4.5 and 8.5) to examine future discharge patterns. The peak runoff generated scenarios were used to assess the individual impact of LULC change and climate change.

Model Performance Evaluation

Four statistical criteria were used for model performance evaluation: the Root Mean Square Error (RMSE) to indicate the average difference between the model-simulated and the observed values. The Nash–Sutcliffe efficiency (NSE) to indicate the level of fitness between simulation and observation results. The coefficient of determination (R^2) was used to express the ability of the model to predict the outcome in a linear regression setting (Moriasi et al., 2007). In addition, Kling-Gupta Efficiency (KGE) criterion proposed by (Gupta et al., 2009), was used to assess the performance of hydrological models. It combines three components: correlation, variability, and bias. The KGE ranges between -∞ and 1, where a higher value indicates better model performance. While a lower KGE signifies poor model performance. (Knoben et al., 2019) suggested that -0.41

indicates the lowest limit of a favorable KGE value for an adequate model. The statistical indicators used in this study are given by Equations. 16, 25, 26, and 27.

$$\mathrm{NSE} = 1 - \frac{\sum_{i=1}^{N}(Q_{i,Obs} - Q_{i,Sim})^2}{\sum_{i=1}^{N}(Q_{i,Obs} - \bar{Q}_{Obs})^2} \quad \textbf{(25)}$$

$$\mathbf{R^2} = \frac{\left[\sum_{\mathbf{i=1}}^{\mathbf{N}}(\mathbf{Q_{i,obs}} - \bar{\mathbf{Q}}_{\mathbf{obs}})(\mathbf{Q_{i,sim}} - \bar{\mathbf{Q}}_{\mathbf{sim}})\right]^2}{\sum_{\mathbf{i=1}}^{\mathbf{N}}(\mathbf{Q_{i,Obs}} - \bar{\mathbf{Q}}_{\mathbf{Obs}})^2 (\mathbf{Q_{i,Sim}} - \bar{\mathbf{Q}}_{\mathbf{Sim}})^2} \quad \textbf{(26)}$$

where $Q_{i,Sim}$ is the simulated discharge at time (t = i), $Q_{i,Obs}$ is the observed discharge at time (t = i), $\overline{Q}_{Obs}$ is the average observed discharge; N is the number of observations.

$$\mathbf{KGE} = \mathbf{1} - \sqrt{(\mathbf{r}-\mathbf{1})^2 + (\mathbf{s}-\mathbf{1})^2 + (\mathbf{b}-\mathbf{1})^2} \quad \textbf{(27)}$$

where r is the Pearson correlation coefficient; s is the ratio of the standard deviation of simulated values to the standard deviation of observed values; b is the ratio of the mean simulated value to the mean observed value.

Contribution Assessment Rate

Hydrological processes are significantly affected by combined changes in climate and land use/land cover (LULC). While climate change and LULC change can interact in complex ways, they are considered as separate factors for analytical purposes (Zhang et al., 2008). In this study, we used the revised one-factor-at-a-time (OFAT) approach (Yang et al., 2017; Ahmed et al., 2022) to separate their individual contributions to the hydrological processes **Figure 25**.

The climatic data were divided into two time periods: the first period (C1) served as a reference, and the second period (C2) was used for comparison. Similarly, the land-use conditions were defined for both time periods using two land-use maps: L1 for the first period and L2 for the second period. These configurations were used to create four different modeling scenarios (SI, S2, S3, and S4) that integrated both climate and land-use data. Equations 28, 29 and 30, serves to calculate the overall fluctuation caused by climate change and LULC change on stream flow regime.

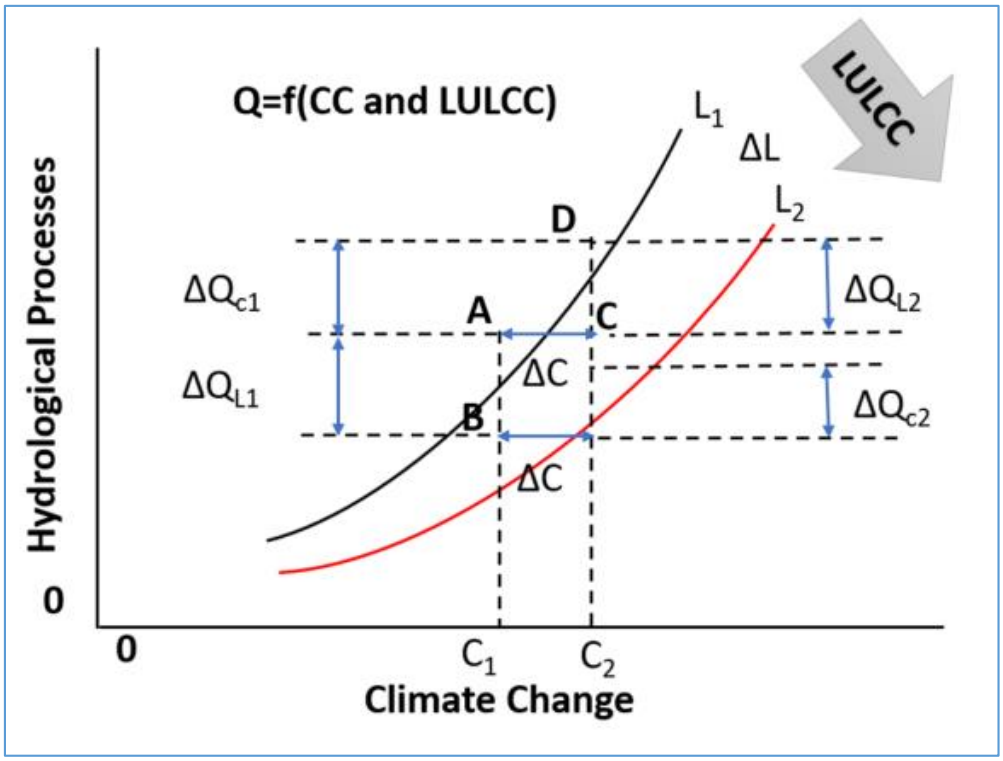

Figure 25. A schematic diagram of separating the effects of climate change and land use change on hydrological processes (Yang et al., 2017; Ahmed et al., 2022).

$$\Delta Q_C = \frac{1}{2}(\Delta Q_{C1} + \Delta Q_{C2}) = \frac{1}{2}\left[\left(Q_{C2}^{L1} - Q_{C1}^{L1}\right) + \left(Q_{C2}^{L2} - Q_{C1}^{L2}\right)\right] \quad (28)$$

$$\Delta Q_L = \frac{1}{2}(\Delta Q_{L1} + \Delta Q_{L2}) = \frac{1}{2}\left[\left(Q_{C1}^{L2} - Q_{C1}^{L1}\right) + \left(Q_{C2}^{L2} - Q_{C2}^{L1}\right)\right] \quad (29)$$

$$\Delta Q = \Delta Q_L + \Delta Q_C = Q_{C2}^{L2} - Q_{C1}^{L1} \quad (30)$$

The contribution rate for climate change and LULC change was assessed for four experimental periods as depicted in **Table 6 - Table 9**.

Table 6. OFAT modelling experiment for the Period 1985 - 2003.

Experiment	Scenario	Period of Land-Use Map	Storm Event
P1	S1	1985	18/12/1984 - 31/07/1985
	S2	2003	18/12/1984 - 31/07/1985
	S3	1985	01/01/2003 – 31/07/2003
	S4	2003	01/01/2003 – 31/07/2003

Table 7. OFAT modelling experiment for the Period 1985 – 2020.

Experiment	Scenario	Period of Land-Use Map	Storm Event
P2	S1	1985	18/12/1984 - 31/07/1985
	S2	2020	18/12/1984 - 31/07/1985
	S3	1985	01/01/2020 – 31/12/2020
	S4	2020	01/01/2020 – 31/12/2020

Table 8. OFAT modelling experiment for the Period 1985 – 2040.

Experiment	Scenario	Period of Land-Use Map	Storm Event
P3	S1	1985	18/12/1984 - 31/07/1985
	S2	2040	18/12/1984 - 31/07/1985
	S3	1985	01/01/2040 – 31/12/2040
	S4	2040	01/01/2040 – 31/12/2040

Table 9. OFAT modelling experiment for the Period 2020 - 2040.

Experiment	Scenario	Period of Land-Use Map	Storm Event
P4	S1	2020	01/01/2020 – 31/12/2020
	S2	2040	01/01/2020 – 31/12/2020
	S3	2020	01/01/2040 – 31/12/2040
	S4	2040	01/01/2040 – 31/12/2040

Trend Analysis

The Mann-Kendall (MK) test was performed, in this study, as a non-parametric, rank-based statistical method to assess and determine the presence of a monotonic trend (either upward or downward) in time series datasets (Mann, 1945; Kendall, 1948). This test is advantageous due to its ability to handle inhomogeneity encountered in climatic and hydrological datasets being less sensitive to such variations while providing reliable results (Yue and Wang, 2004; Hu et al., 2020). In hydro-meteorological data analysis, the MK statistical test paired with Sen's Slope tests are frequently used to identify trends within time series and show the trends slope. When testing the null hypothesis (H0), it assumes that the data consists of independent and identically distributed samples, indicating no consistent trend present. In contrast, when the distributions of consecutive

values (X_j and X_i) differ for distinct j, as indicated in the alternative hypothesis (Ha), and I a discernible trend in the data is apparent. (Xu et al., 2006; Da Silva et al., 2015). The test statistic is presented as follows:

$$\boldsymbol{S = \sum_{i=1}^{n-1} \sum_{j=i+1}^{n} sign(X_j - X_i)} \quad \textbf{(31)}$$

in which n is the length of the data set and X_j and X_i are sequential data values. The sign function is given as follow:

$$\boldsymbol{sign(X_j - X_i) = \begin{cases} 1, \ if \ (X_j - X_i) > 0 \\ 0, \ if \ (X_j - X_i) = 0 \\ -1, \ if \ (X_j - X_i) < 0 \end{cases}} \quad \textbf{(32)}$$

The Mann-Kendall test statistics are evaluated in relation to the Gaussian distribution in order to decide if the null hypothesis (H0) should be accepted. The critical value $\left(Z_{\frac{1-\alpha}{2}}\right)$ for the chosen significance level (α=10%) for the test statistic was set at ±1.645. The null hypothesis is rejected, for a 10% significance level, when the calculated Z value is greater than the critical value ($Z_{\frac{1-\alpha}{2}} = \pm 1.645$). The alternative hypothesis is then established, implying that the data contains a substantial trend (Arfasa et al., 2024).

Moreover, the MK test statistics (S) are considered to be normally distributed with a mean equal to zero, for sampling sizes exceeding ten values (n > 10). In this instance, the variance and the standardized test statistics Z are calculated as follows:

$$\boldsymbol{\mu(S) = 0} \quad \textbf{(33)}$$

$$\boldsymbol{Var(S) = (n/18)(n-1)(2n+5)} \quad \textbf{(34)}$$

$$\boldsymbol{Z = \begin{cases} \frac{S-1}{\sigma}, \ if \ S > 0 \\ 0, \ if \ S = 0 \\ \frac{S+1}{\sigma}, \ if \ S > 0 \end{cases}} \quad \textbf{(35)}$$

Sen's slope estimator is a nonparametric method used to estimate the magnitude of trends in data (Sen, 1968). If the trend is assumed to be a linear function, Sen's slope follows this equation:

$$\boldsymbol{f(t) = \theta t + Int} \quad \textbf{(36)}$$

where θ is the slope and Int is the intercept. The slope for the pairs of data is calculated as follows:

$$\boldsymbol{Q_k = \frac{X_j - X_i}{j - i}} \quad \textbf{(37)}$$

while j > I, and X_j and X_i are the data values at times j and i respectively.

For n number of periods, $N = \frac{n(n-1)}{2}$ numbers of slopes can be estimated. The Q_k values are then sorted in ascending order according on their n values, leading to the computation of the median slope, also known as Sen's slope:

$$\boldsymbol{Q = \begin{cases} Q_{\left[(N+1)/2\right]}, & \textit{If N is odd} \\ \frac{1}{2}\left(Q_{\left[N/2\right]} + Q_{\left[(N+1)/2\right]}\right), & \textit{If N is even} \end{cases}} \quad \textbf{(38)}$$

In this study, the Mann-Kendall trend test and Sen's Slope Estimator provided by XLSTAT software are utilized to examine observed and predicted trends in precipitation, temperature, and discharge across a time series of meteorological and hydrological data.

In summary, this chapter detailed the comprehensive methodology employed in this study, which involved the integration of data collected from various sources. We utilized ArcGIS for data preprocessing and the MOLUSCE plugin in QGIS to derive the 2040 LULC map. The HEC-HMS model was then applied to simulate rainfall-runoff processes. Following the discharge simulations, we quantified the isolated impacts of climate and LULC changes, via the OFAT method. Finally, we conducted a trend analysis for two distinct periods: 1970-2010 and 2020-2060.

Chapter IV: Results & Discussion.

Change Detection Analysis of the Kebir river catchment

The change detection matrices results for the change periods between 1985–2003 and 2003–2020 are presented in **Figure 26** and Tables 10 - 12, respectively. The LULC change detection results between 1985 and 2020 also indicated a change in all LULC classes. The agricultural lands showed an increase from 554.99 km^2 to 562.14 km^2 (0.63%). The water bodies and built-up lands increased from 0.44 km^2 to 7.06 km^2 (0.58%) and 6.61 km^2 to 14.95 km^2 (0.74%) respectively. The barren lands and forests decreased from 22.28 km^2 to 14.10 km^2 (0.72%) and 547.96 km^2 to 534.02 km^2 (1.23%) respectively. The findings show the increase in built-up lands, agricultural lands and water bodies from 1985 to 2020 demonstrating urbanization development and growth of agricultural activities in the area. The increase of agricultural lands may also be due to deforestation. The increase in water bodies could be a result of the Zit-Emba Dam's construction in the Kebir river catchment. Previous research found that agricultural land is the essential driver of LULC changes, which is also supported by this study's findings (Araya and Cabral, 2010; Gashaw et al., 2018).

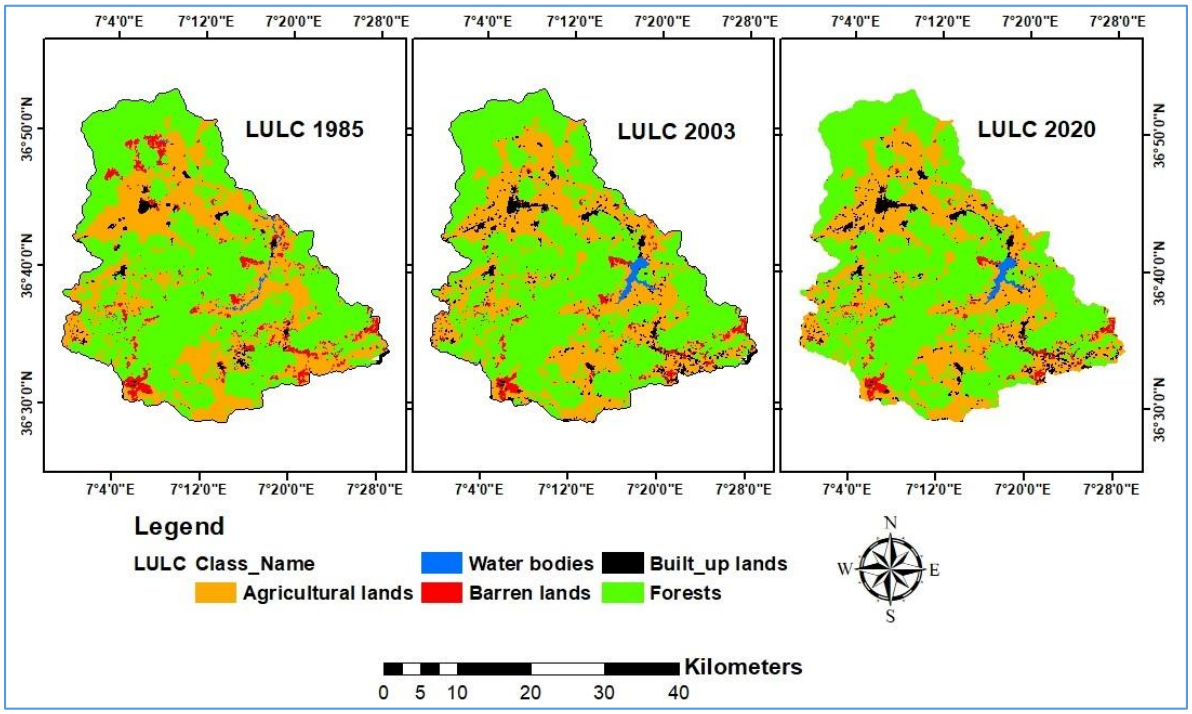

Figure 26. LULC map of the Kebir river catchment of the years of 1985, 2003 and 2020.

Table 10. LULC changes between 1985-2003 in Kebir River Catchement.

Classes	LULC Classes	LULC Area (km^2)		Δ Difference (km^2)	LULC Area (%)		Δ Difference (%)
		1985	2003		1985	2003	
1	Agricultural lands	554.99	563.69	8.71	48.988	49.757	0.768
2	Water Bodies	0.44	7.02	6.57	0.039	0.619	0.580
3	Barren lands	22.28	15.46	-6.82	1.967	1.365	-0.602
4	Built-up lands	6.61	12.82	6.22	0.583	1.132	0.549
5	Forests	548.58	533.91	-14.67	48.423	47.128	-1.295

Table 11. LULC changes between 2003-2020 in Kebir River Catchement.

Classes	LULC Classes	LULC Area (km^2)		Δ Difference (km^2)	LULC Area (%)		Δ Difference (%)
		2003	2020		2003	2020	
1	Agricultural lands	563.69	562.14	-1.55	49.779	49.642	-0.137
2	Water Bodies	7.02	7.06	0.04	0.620	0.623	0.004
3	Barren lands	15.46	14.10	-1.36	1.365	1.245	-0.120
4	Built-up lands	12.94	15.06	2.13	1.142	1.330	0.188
5	Forests	533.28	534.02	0.74	47.094	47.159	0.065

Table 12. LULC changes between 1985-2020 in Kebir River Catchement.

Classes	LULC Classes	LULC Area (km^2)		Δ Difference (km^2)	LULC Area (%)		Δ Difference (%)
		1985	2020		1985	2020	
1	Agricultural lands	554.99	562.14	7.16	49.015	49.647	0.632
2	Water Bodies	0.44	7.06	6.62	0.039	0.623	0.584
3	Barren lands	22.28	14.10	-8.18	1.968	1.245	-0.723
4	Built-up lands	6.61	14.95	8.34	0.583	1.320	0.737
5	Forests	547.96	534.02	-13.93	48.394	47.164	-1.230

Transition potential probabilities between 1985 and 2020

Tables 13 - 15 were automatically generated in Molusce plugin. These tables display the resultant probabilities matrix, reflecting the likelihood of each LULC type changing to another type.

Table 13 was used for generating the 2020 predicted LULC map. According to the results of this study, the greatest LULC change matrix from 1985 to 2003 could be detected in the conversion of agricultural lands to water bodies (probability rate = 0.554) and barren lands into agricultural lands (probability rate = 0.306).

Table 13. Transition matrix probabilities between 1985 and 2003.

Year		2003				
	Classes	**Agricultural lands**	**Water Bodies**	**Barren lands**	**Built up lands**	**Forests**
1985	**Agricultural lands**	0.977185	0.012328	0	0.010468	0.000019
	Water Bodies	0.553971	0.393075	0.010183	0	0.04277
	Barren lands	0.305682	0	0.693631	0.000687	0
	Built up lands	0.117318	0	0	0.881728	0.000954
	Forests	0.024675	0	0	0.002136	0.973189

Table 14 was used for generating the 2040 predicted LULC map. According to the results of this study, the greatest LULC change matrix from 2003 to 2020 could be detected in the conversion of barren lands into agricultural lands (probability rate = 0.066).

Table 14. Transition matrix probabilities between 2003 and 2020.

Year		2020				
	Classes	**Agricultural lands**	**Water Bodies**	**Barren lands**	**Built up lands**	**Forests**
2003	**Agricultural lands**	0.99384	0.000075	0.000011	0.00311	0.002963
	Water Bodies	0	1	0	0	0
	Barren lands	0.065716	0	0.911583	0.021246	0.001455
	Built up lands	0.000278	0	0	0.999722	0
	Forests	0.001693	0	0.000002	0.000091	0.998214

Table 15 was established to examine the general shifts between 1985 and 2020. The greatest LULC changes from this period indicated the conversion of agricultural lands into water bodies (probability rate = 0.554), barren lands into agricultural lands (probability rate = 0.341), and agricultural lands into built-up lands (probability rate = 0.111).

Table 15. Transition matrix probabilities between 1985 and 2020.

Year		2020				
1985	**Classes**	**Agricultural lands**	**Water Bodies**	**Barren lands**	**Built up lands**	**Forests**
	Agricultural lands	0.971592	0.012404	0.000011	0.013547	0.002445
	Water Bodies	0.553971	0.393075	0.010183	0	0.04277
	Barren lands	0.341424	0	0.632285	0.015468	0.010823
	Built up lands	0.111323	0	0	0.887996	0.000681
	Forests	0.026158	0	0.000002	0.002224	0.971616

Expansions of built-up areas and water bodies in Kebir river catchment are observed according to the LULC map for 2020 analysis results. These changes present serious challenges caused by the decrease of other LULC types, primarily cropland and, to a lesser extent, forests. In contrast to forests and barren areas, agricultural fields change the most in the research area.

LULC change prediction and validation

The study calculated the percentage of pixels that underwent changes, to quantify the magnitude and asses patterns of LULC class that transitioned from one to another, between the initial and final LULC map. In the process of learning, the ANN needs a number of parameters, set by the user as mentioned earlier, for which optimized values are usually found by trial and error.

LULC trends for 2020 were predicted using spatial variables, LULC data from 1985 to 2003, and the CA-ANN model. The CA-ANN model was first trained and validated using the available data, and then used to generate the predicted LULC map for the year 2020. This predicted LULC map was then compared to the reference LULC map for the year 2020 to evaluate the model's performance. The validated result shows that the model can reliably predict future LULC for the Kebir river catchment with an overall accuracy of 99.27 % and an overall Kappa value of 0.98. The predicted LULC map for 2040 (**Figure 27**) was generated based on this validated model, with an increase in iterations.

Table 16. LULC changes between 1985 - 2040 in Kebir River Catchment.

Classes	LULC Classes	LULC Area (km^2)		Δ Difference (km^2)	LULC Area (%)		Δ Difference (%)
		1985	2040		1985	2040	
1	Agricultural lands	554.99	559.56	4.57	48.988	49.392	0.403
2	Water Bodies	0.44	7.06	6.62	0.039	0.623	0.584
3	Barren lands	22.28	14.10	-8.18	1.967	1.245	-0.722
4	Built-up lands	6.61	18.16	11.55	0.583	1.603	1.020
5	Forests	548.58	534.02	-14.56	48.423	47.137	-1.285

Table 16 illustrates the percentage change for LULC from 1985 to 2040. The results demonstrate expansion of urban areas, water bodies, and croplands at the expense of forests and barren grounds. In 2040, the increase in the built-up, water bodies, and agricultural lands will represent 1.02%, 0.584%, and 0.403% respectively of the study area compared to 1985.

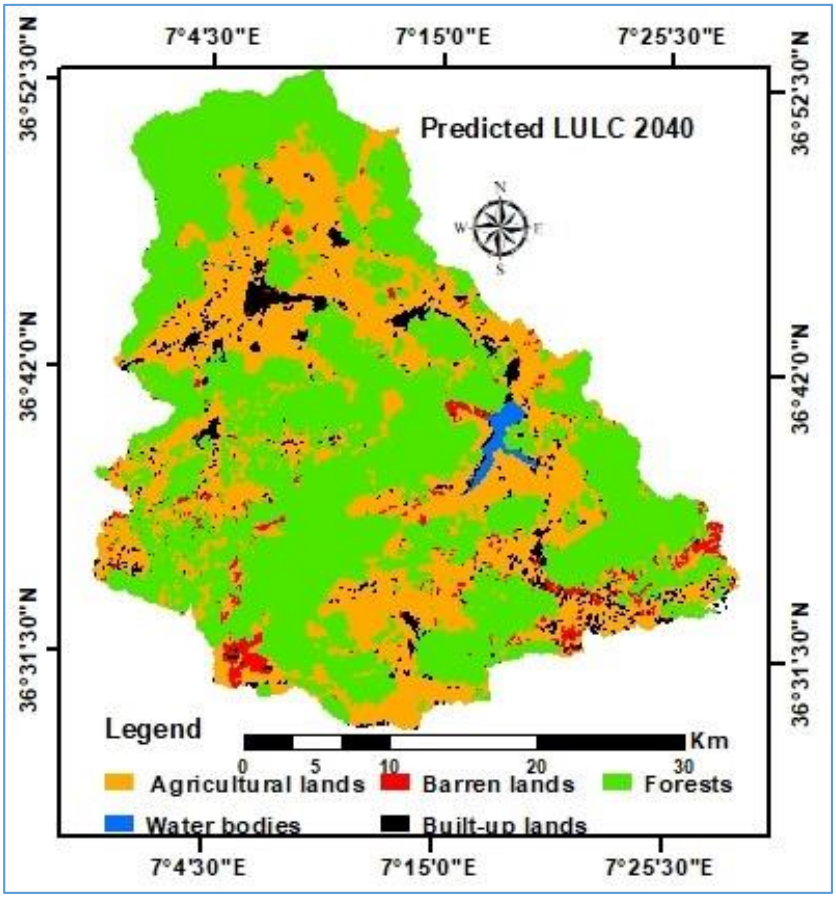

Figure 27. Predicted LULC map for 2040 in Kebir river catchment.

Compared to other LULCs, forest will have the greatest loss in surface area by 2040, losing roughly 1.285% from 1985, followed by barren lands (0.722%). The water cycle will be detrimentally affected by the ever-changing trends in LULC from 1985 to 2040. In addition, the projected increase in the urbanization, water bodies, and agricultural lands, and the decrease in forest areas will result in ecosystem disruptions. Although these changes may indicate local climate effects, it is important to carefully analyze whether they can be solely attributed to broader climate change.

Model calibration and validation

The HEC-HMS model was used to determine the simulated discharge and runoff volumes for LULC maps from 1985, 2003, 2020, and 2040. The results were then compared to analyze the hydrological effects of the LULC changes. Table 17 also incorporated specific CN, Lag time, and impervious percentage for both sub-catchments between 1985 and 2040. The results illustrate an

increase in CN and a decrease in lag time, with CN values ranging from 69.62 to 70.88 for the first sub-catchment and 69.71 to 71.25 for the second, resulting in a decrease in lag time for both sub-catchments. The impervious rate vary depending on the changes that have occurred in the catchment.

Table 17. Characteristics of Kebir river catchment for the different LULC scenarios.

Sub Catchment	LULC 1985			LULC 2003		
	CN	**Lag Time (min)**	**% Impv**	**CN**	**Lag Time (min)**	**% Impv**
W1	69.62	401.30	0.033	69.77	399.59	0.026
W2	69.71	311.49	0.049	70.22	307.28	0.042
Sub Catchment	**LULC 2020**			**LULC 2040**		
	CN	**Lag Time (min)**	**% Impv**	**CN**	**Lag Time (min)**	**% Impv**
W1	69.86	398.63	0.029	70.88	398.49	0.321
W2	70.49	306.91	0.041	71.25	306.63	0.348

Peak discharge and runoff volume were simulated in HEC-HMS using data from the Kebir river gage station. The model was calibrated from December 18, 1984 to July 31, 1985, and validated from January 1, 2003 to July 31, 2003. During both calibration and validation phases, simulated discharge hydrographs are compared to observed discharge hydrographs..

The simulated and observed discharge values during calibration are shown in Table 18 for different LULC maps. The discharge hydrographs for this period were generated in the HEC-HMS model are displayed in Figures 28 – 31.

Table 18. Global summary results for the events storm from 18/12/1984 to 31/07/1985.

LULC	Simulated peak discharge (m^3/s)	Simulated runoff volume (mm)	Observed peak discharge (m^3/s)	Observed runoff volume (mm)
1985	351.40	598.75	297.10	383.69
2003	351.40	600.07	297.10	383.69
2020	353.80	601.02	297.10	383.69
2040	358.20	605.67	297.10	383.69

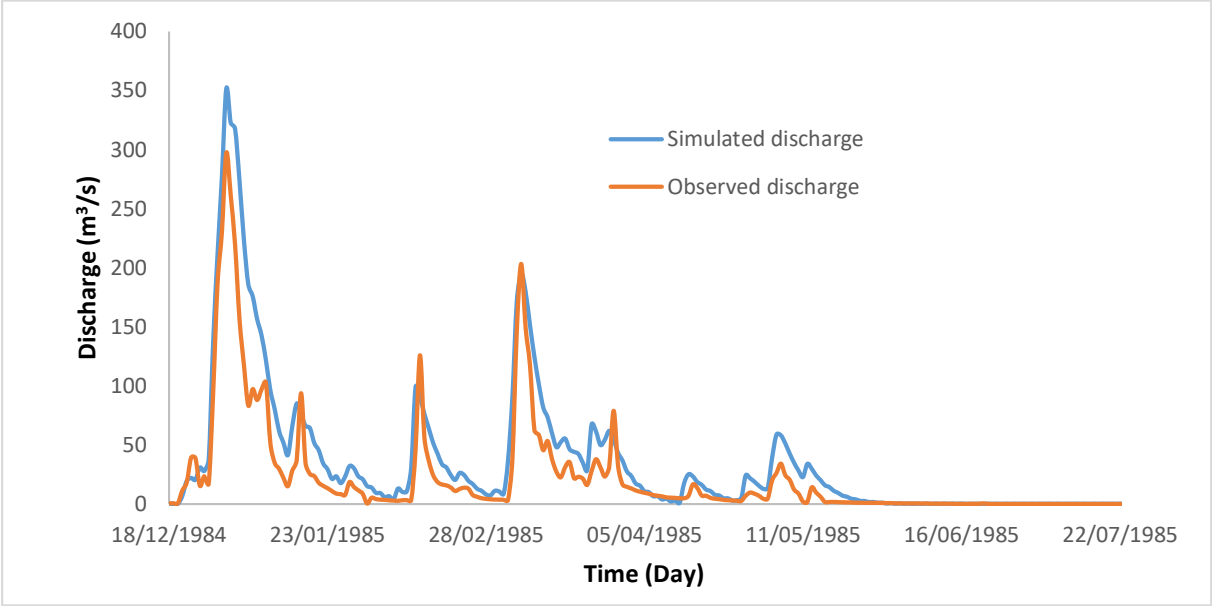

Figure 28. Comparison of simulated and observed hydrographs for the event storm from 8/12/1984 to 31/07/1985 in the case of the LULC 1985.

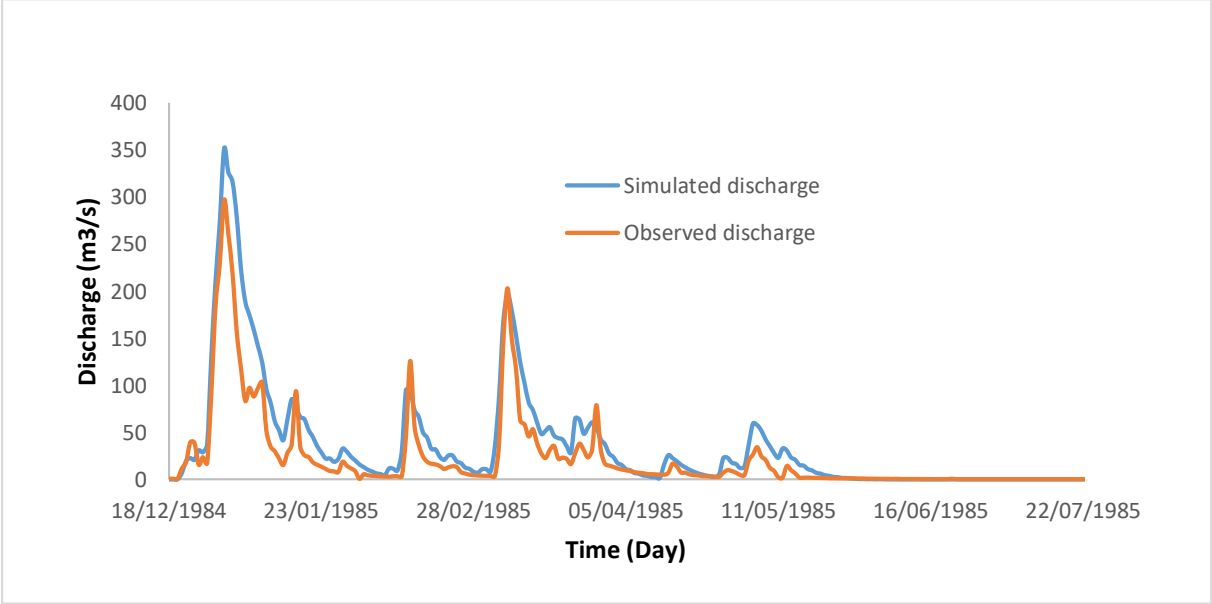

Figure 29. Comparison of simulated and observed hydrographs for the event storm from 18/12/1984 to 31/07/1985 in the case of the LULC 2003.

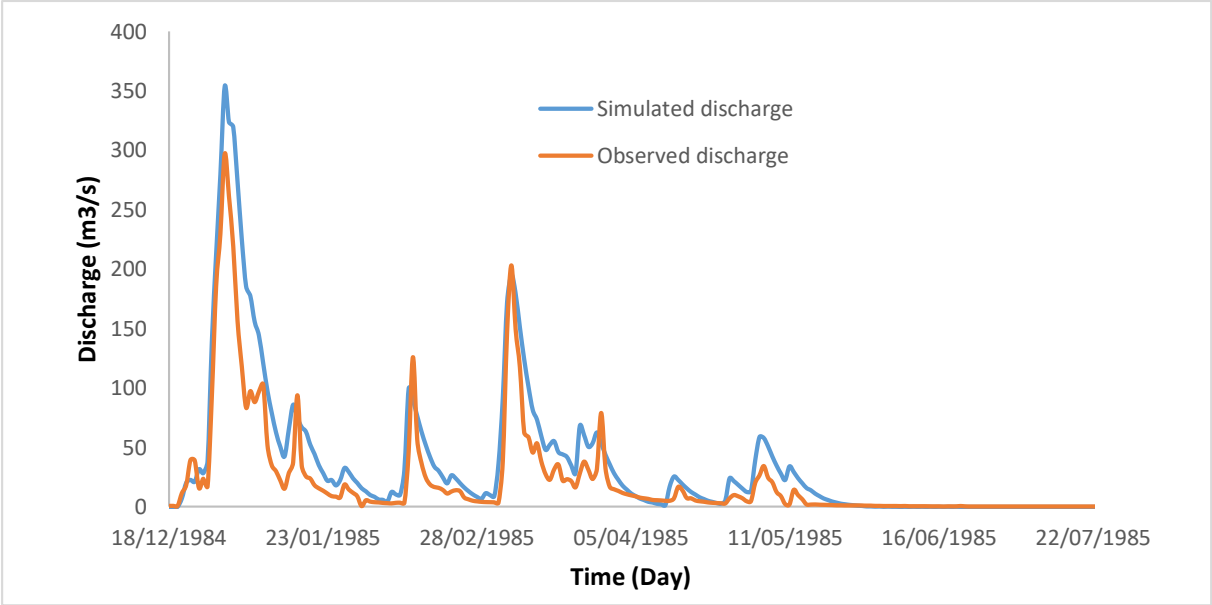

Figure 30. Comparison of simulated and observed hydrographs for the event storm from 18/12/1984 to 31/07/1985 in the case of the LULC 2020.

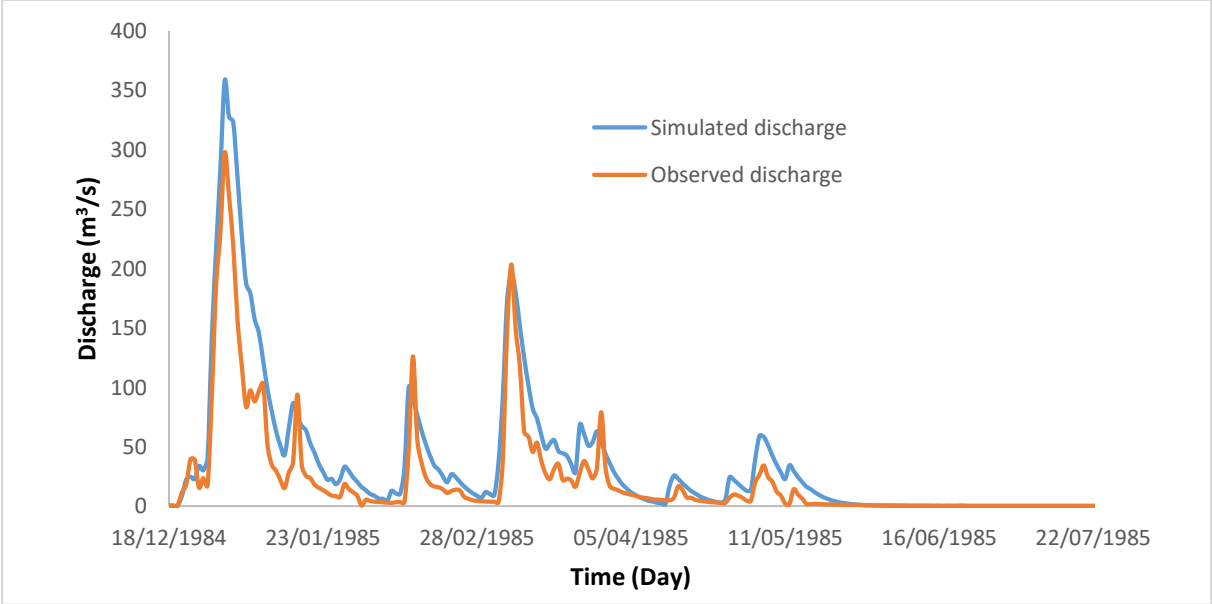

Figure 31. Comparison of simulated and observed hydrographs for the event storm from 18/12/1984 to 31/07/1985 in the case of the LULC 2040.

The model was validated for several LULC maps. The simulated and observed discharge values resulting are shown in Table 19. The discharge hydrographs for this period were also generated in the HEC-HMS model are displayed in Figures 32 - 35.

Table 19. Global summary results for the event storm from 01/01/2003 to 31/07/2003.

LULC	Simulated peak discharge (m^3/s)	Simulated runoff volume (mm)	Observed peak discharge (m^3/s)	Observed runoff volume (mm)
1985	163.20	444.45	156.20	280.11
2003	162.70	445.88	156.20	280.11
2020	164.60	446.85	156.20	280.11
2040	166.80	451.24	156.20	280.11

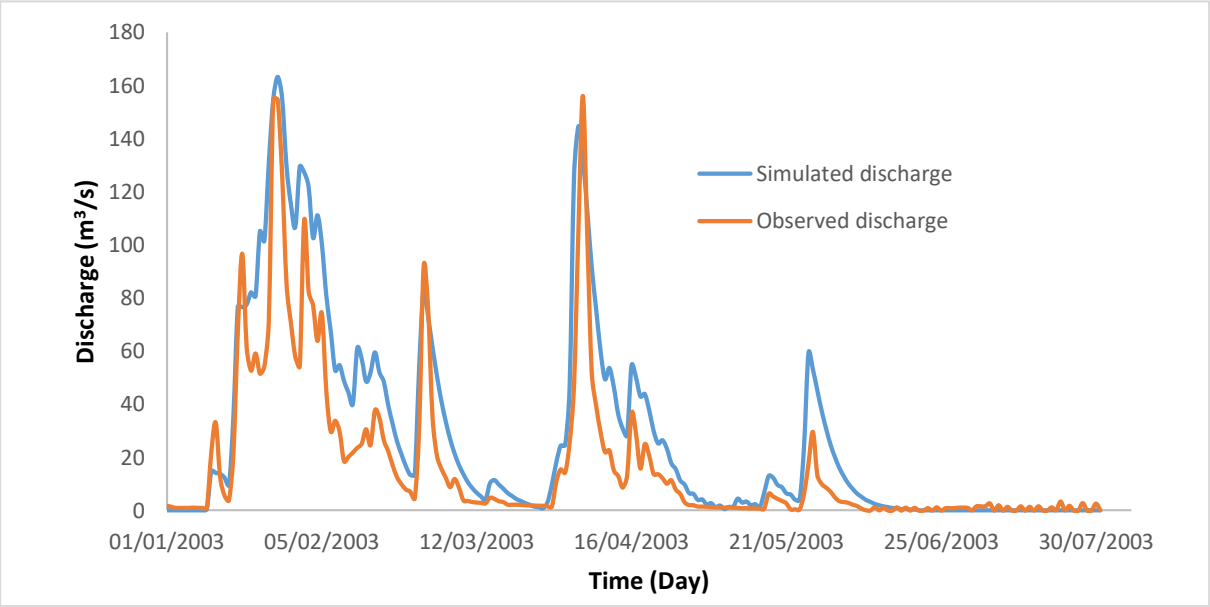

Figure 32. Comparison of simulated and observed hydrographs for the event storm from 01/01/2003 to 31/07/2003 in the case of the LULC 1985.

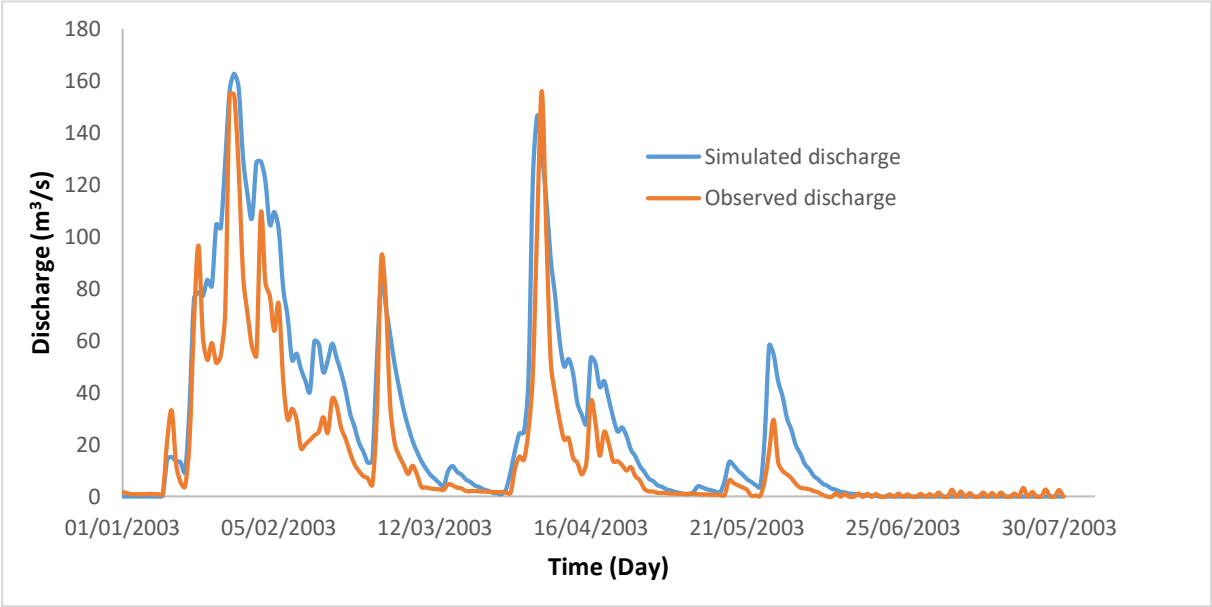

Figure 33. Comparison of simulated and observed hydrographs for the event storm from 01/01/2003 to 31/07/2003 in the case of the LULC 2003.

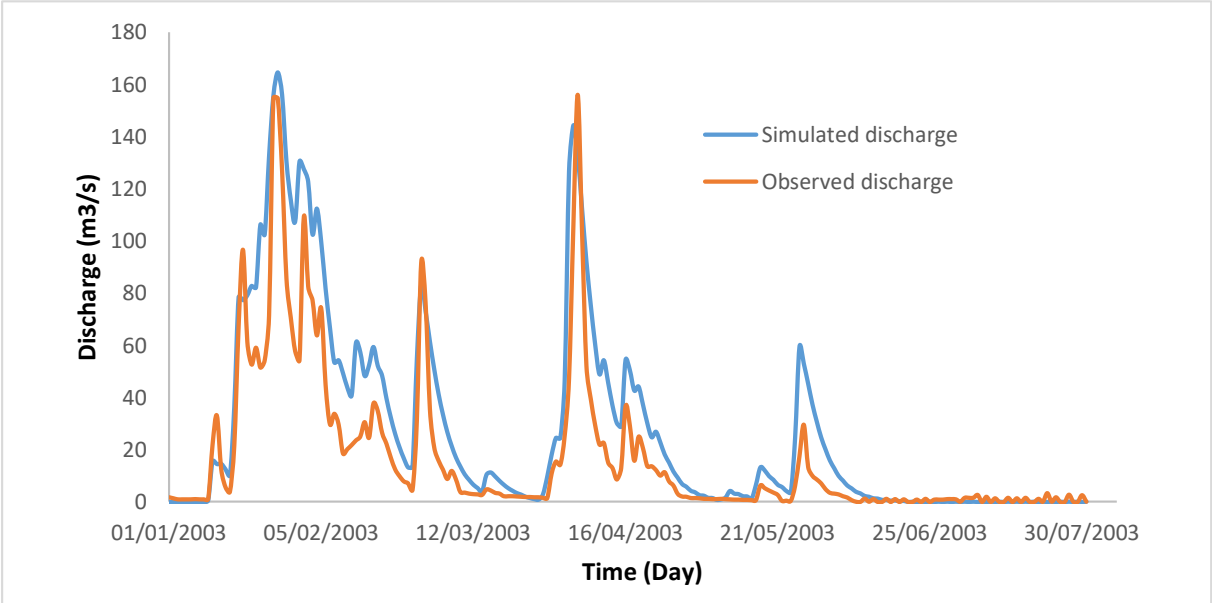

Figure 34. Comparison of simulated and observed hydrographs for the event storm from 01/01/2003 to 31/07/2003 in the case of the LULC 2020.

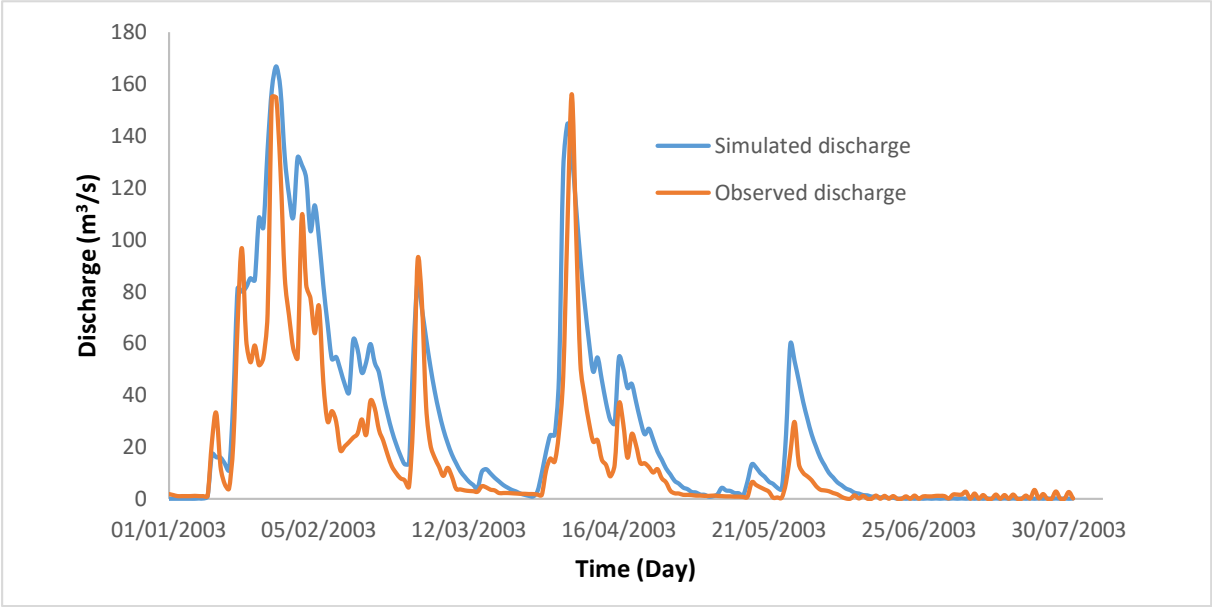

Figure 35. Comparison of simulated and observed hydrographs for the event storm from 01/01/2003 to 31/07/2003 in the case of the LULC 2040.

In this study, the simulated values for both phases and periods are recorded to be greater than the observed values (Figures 28 - 35). Neglecting to factor in the inflow and outflow dynamics of the Zit-Emba Dam in the Kebir River watershed in the process led to the observed distinctions. Given the scarcity of data and potential uncertainties in the input data, for instance precipitation data, even minor changes in these parameters might have significant impacts on the simulated outcomes. Moreover, the simulated results between 1985 and 2040 display an increase of 1.93% in peak discharge in the calibration period and an increase of 2.20% in the validation period. The runoff volume increased by 1.15% in the calibration period and by 1.53% in the validation period. The aforementioned rise correlated with an increase in CN value and a decrease in lag time value, which resulted mainly by growing urbanization, an improvement in agricultural croplands, and a decrease in wooded areas areas.

Model performance

The model performance was conducted, for daily time step, using observed data. The HEC-HMS model's performance is evaluated during the calibration and validation periods using RMSE, NSE, and R2 values.

The model performance was judged adequate for all LULC change scenarios. During the calibration period, the RMSE and R2 values were 0.50 and 0.92, respectively (Table 20).While, during validation, the RMSE value was 0.60 and the R2 value varied between 0.86 and 0.87 (Table 21). Furthermore, the NSE values were appropriate, ranging between 0.701 and 0.720 during calibration (Table 20) and between 0.598 and 0.608 during validation (Table 21). These results are considered suitable and satisfactory according to (Moriasi et al., 2007; Hachemaoui et al., 2022). The KGE values were relatively decent compared to benchmark bounds according to (Knoben et al., 2019) they varied between 0.36 and 0.56 during calibration (Table 20). During validation, they ranged between 0.31 and 0.34 (Table 21).

Table 20. Statistical performance results obtained during the calibration period from (18/12/1984 to 31/07/1985).

LULC	Computation point	RMSE	NSE	R^2	KGE
1985	Outlet	0.50	0.720	0.92	0.358
2003		0.50	0.717	0.92	0.565
2020		0.50	0.714	0.92	0.564
2040		0.50	0.701	0.92	0.555

Table 21. Statistical performance results obtained during the validation period from (01/01/2003 to 31/07/2003).

LULC	Computation point	RMSE	NSE	R^2	KGE
1985	Outlet	0.60	0.598	0.86	0.358
2003		0.60	0.608	0.87	0.565
2020		0.60	0.602	0.87	0.564
2040		0.60	0.598	0.87	0.555

Model forecasting

The impact of climate change and LULC changes on future discharges and runoff volume was evaluated using the HEC-HMS model. LULC maps from 1985, 2003, 2020, and 2040 were utilized, along with climate factors such as precipitation and maximum and minimum temperatures.

Climate data from the RCA4-CNRM-CERFACS-CM5 model underwent bias correction using historical data from 1970 to 2005 fitted to three meteorological stations (1102, 1108 and 1201). To assure the assessment's accuracy, three bias correction procedures were used for each climatic element. The bias correction techniques applied to precipitation and temperature data have improved the raw RCM simulations to some extent. They were compared and ranked based on their performance to bring the raw-RCM median closer to observations using time-series-based statistical measure shown in Table 22.

Table 22. Ranking of different bias correction procedures for temperature and precipitation based on RMSE and MAE.

PCP	**RMSE**			**MAE**		
	1102	**1108**	**1201**	**1102**	**1108**	**1201**
LOCI	6.82	7.39	7.72	2.62	2.96	3.00
PT	7.18	7.56	7.86	2.63	2.95	3.01
DM	8.14	8.94	8.78	2.75	3.11	3.10
TMPmin	**RMSE**			**MAE**		
	1102	**1108**	**1201**	**1102**	**1108**	**1201**
VS	3.52	3.28	3.39	2.81	2.62	2.70
DM	3.55	3.31	3.43	2.85	2.65	2.75
LS	5.14	5.09	5.02	4.14	4.1	4.03
TMPmax	**RMSE**			**MAE**		
	1102	**1108**	**1201**	**1102**	**1108**	**1201**
VS	5.02	4.79	4.83	3.99	3.77	3.84
DM	5.83	5.35	5.66	4.60	4.21	4.46
LS	5.84	5.84	5.71	4.66	4.27	4.53

LOCI: Local intensity scaling; PT: power transformation; DM: distribution mapping; VS: variance scaling; LS: linear scaling.

When considering precipitation, the LOCI method performed the best, followed by power transformation, with distribution mapping coming in last. For temperature correction, variance scaling was the most effective, followed by distribution mapping, and linear scaling was the least effective for both minimum and maximum temperatures. The necessity of bias-correcting raw

RCM or GCM datasets before utilizing them for climate change impact assessments is evident, highlighting the need to fit the CDF gridded data to enhance simulated climatic data.

Using precipitation data obtained by LOCI correction and Temperature data by VS correction, discharge hydrographs were simulated for the year 2020 and the year 2040. Two greenhouse gas emission scenarios (RCP4.5 and 8.5) were considered and compared.

The simulated discharge values, under RCP 4.5 and RCP 8.5, during the first period from 01/01/2020 to 31/12/2020 are shown in Table 23 for different LULC changes. The discharge hydrographs for this period were generated in the HEC-HMS model are displayed in Figures 36 - 39.

Table 23. Global summary results for the event storm from 01/01/2020 to 31/12/2020.

	RCP 4.5		RCP 8.5	
LULC	**Peak discharge (m3/s)**	**Volume runoff (mm)**	**Peak discharge (m3/s)**	**Volume runoff (mm)**
1985	130.6	525	108.8	598.26
2003	131.5	527.02	108.8	619.53
2020	131.6	527.23	108.8	600.02
2040	131.8	527.69	108.9	600.49

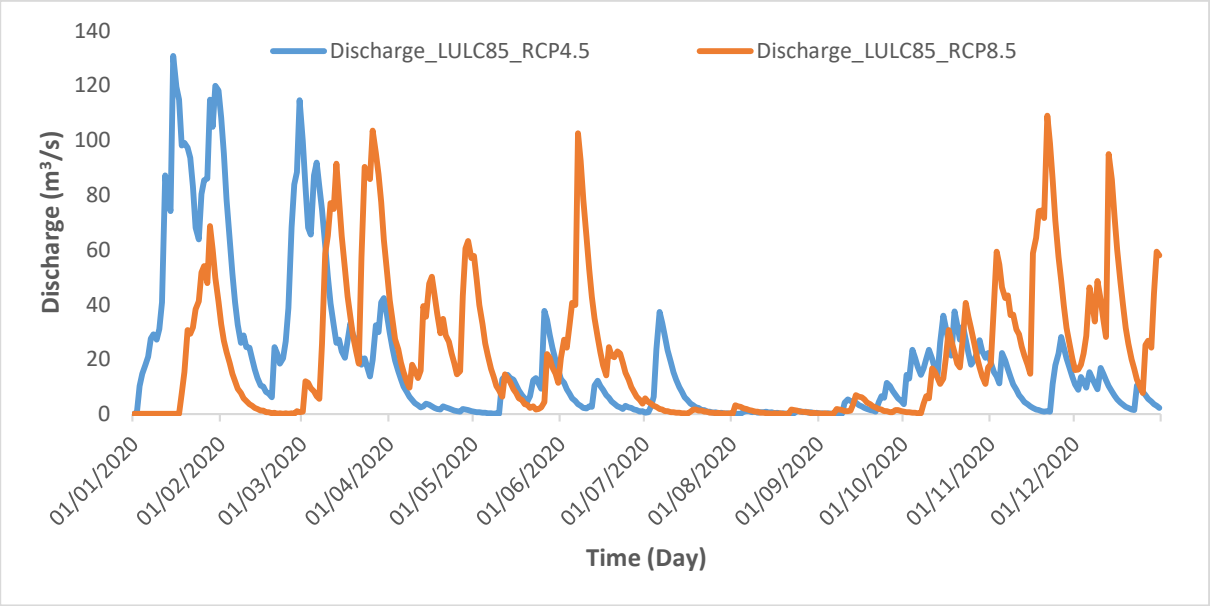

Figure 36. Comparison of simulated RCP 4.5 and RCP 8.5 hydrographs for the event storm from 01/01/2020 to 31/12/2020 in the case of the LULC 1985.

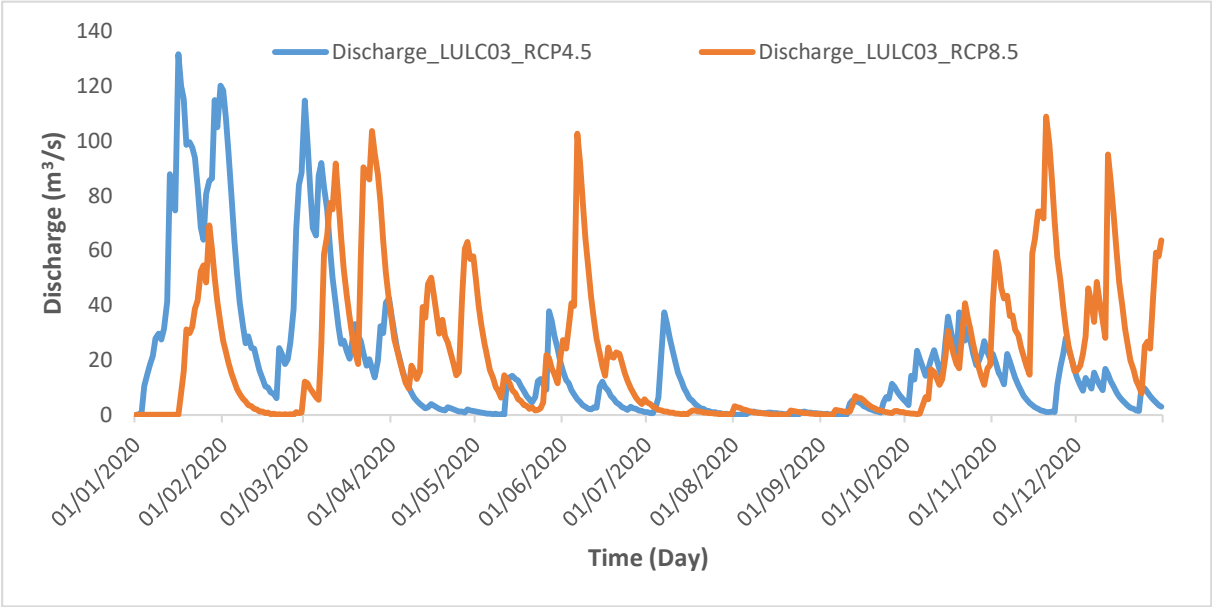

Figure 37. Comparison of simulated RCP 4.5 and RCP 8.5 hydrographs for the event storm from 01/01/2020 to 31/12/2020 in the case of the LULC 2003.

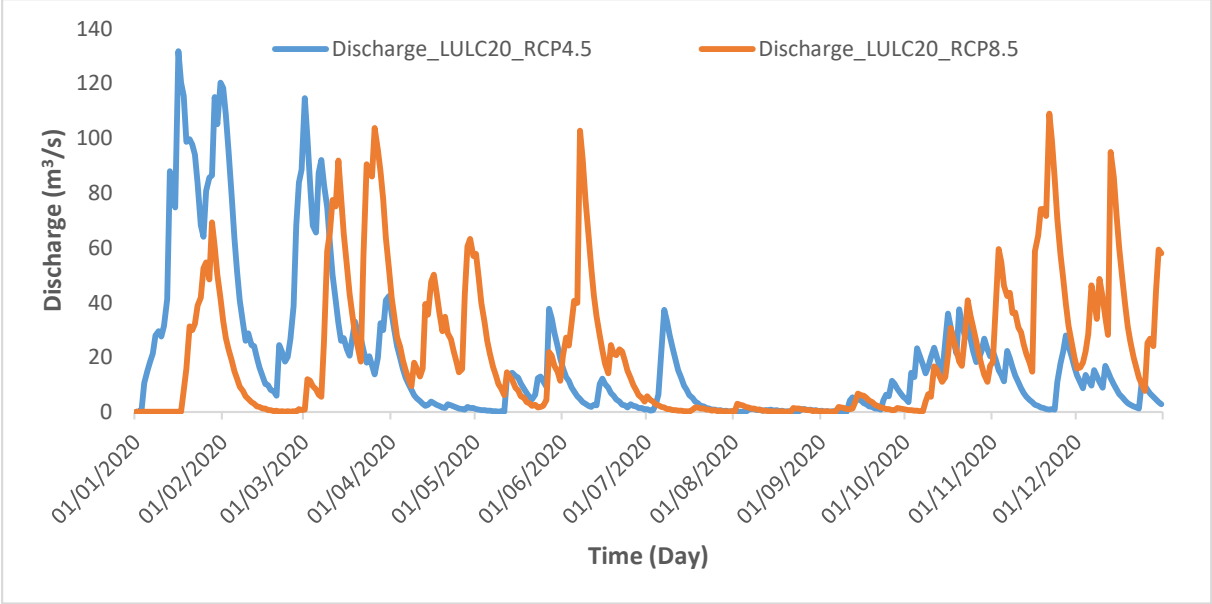

Figure 38. Comparison of simulated RCP 4.5 and RCP 8.5 hydrographs for the event storm from 01/01/2020 to 31/12/2020 in the case of the LULC 2020.

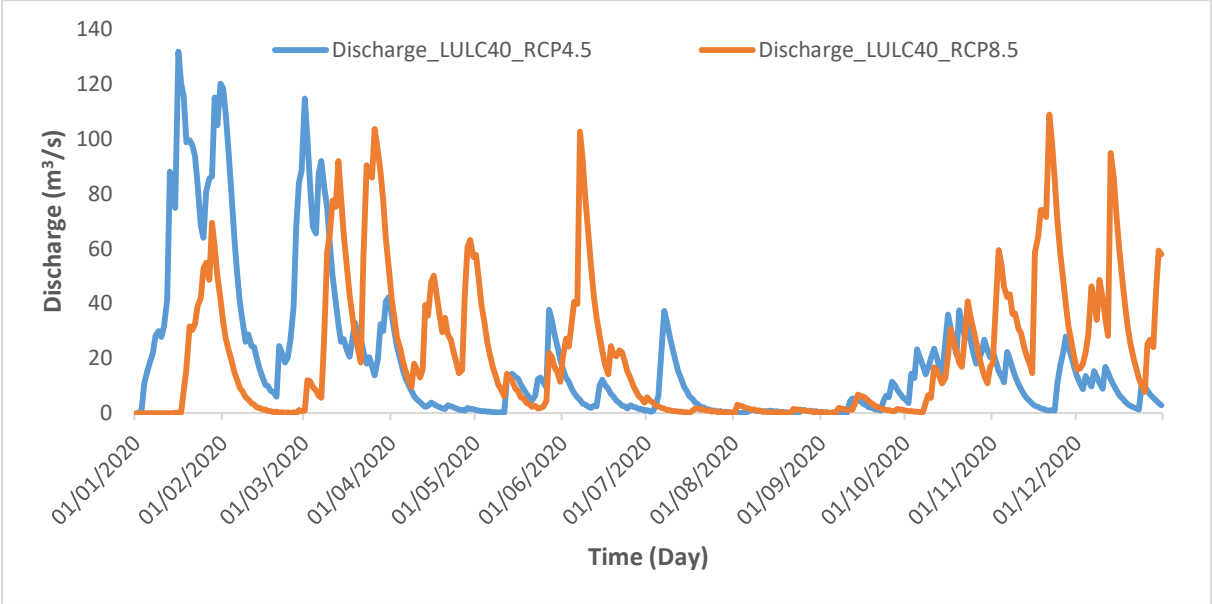

Figure 39. Comparison of simulated RCP 4.5 and RCP 8.5 hydrographs for the event storm from 01/01/2020 to 31/12/2020 in the case of the LULC 2040.

The simulated discharge values, under RCP 4.5 and RCP 8.5, resulting for the period from 01/01/2040 to 31/12/2040 are shown in Tale 24. The discharge hydrographs for this period were also generated in the HEC-HMS model are displayed in Figures 40 – 43.

Table 24. Global summary results for the event storm from 01/01/2040 to 31/12/2040.

	RCP 4.5		RCP 8.5	
LULC	**Peak discharge (m3/s)**	**Volume runoff (mm)**	**Peak discharge (m3/s)**	**Volume runoff (mm)**
1985	345.6	593.72	139.1	327.12
2003	345.8	595.27	139.3	335.07
2020	345.8	595.48	139.4	328.65
2040	345.9	595.95	139.4	329.09

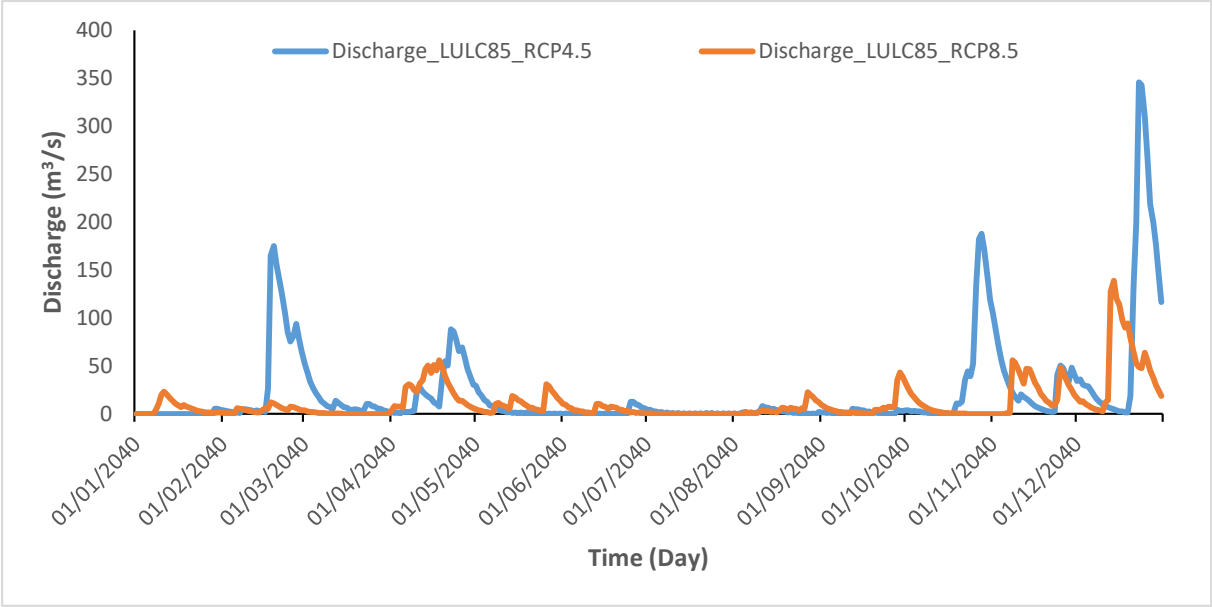

Figure 40. Comparison of simulated RCP 4.5 and RCP 8.5 hydrographs for the event storm from 01/01/2040 to 31/12/2040 in the case of the LULC 1985.

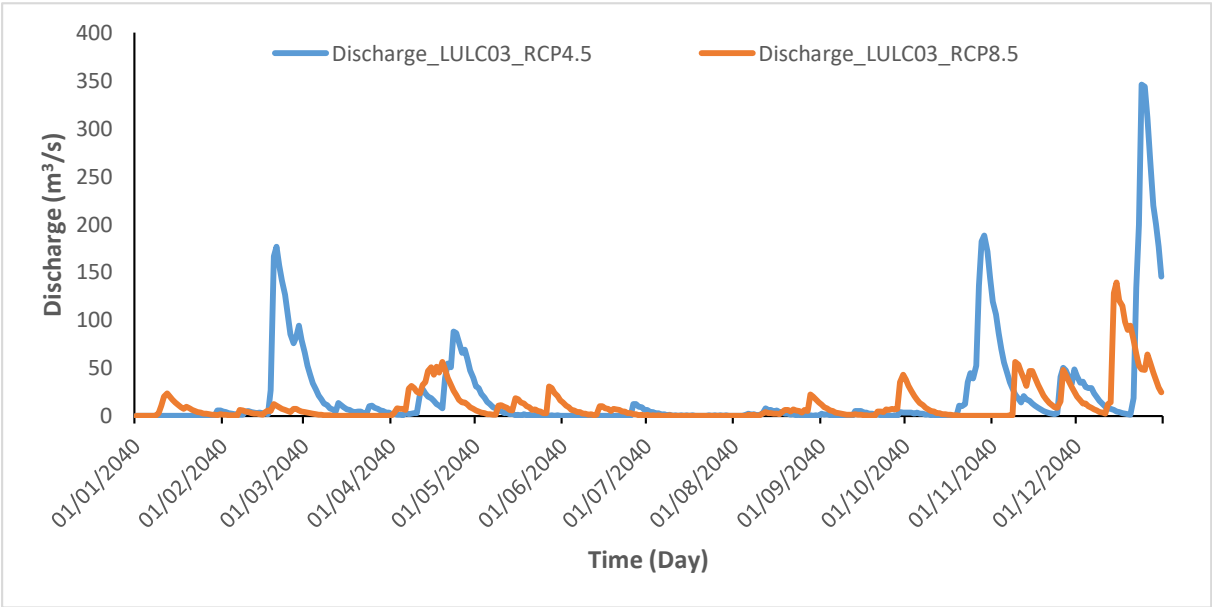

Figure 41. Comparison of simulated RCP 4.5 and RCP 8.5 hydrographs for the event storm from 01/01/2040 to 31/12/2040 in the case of the LULC 2003.

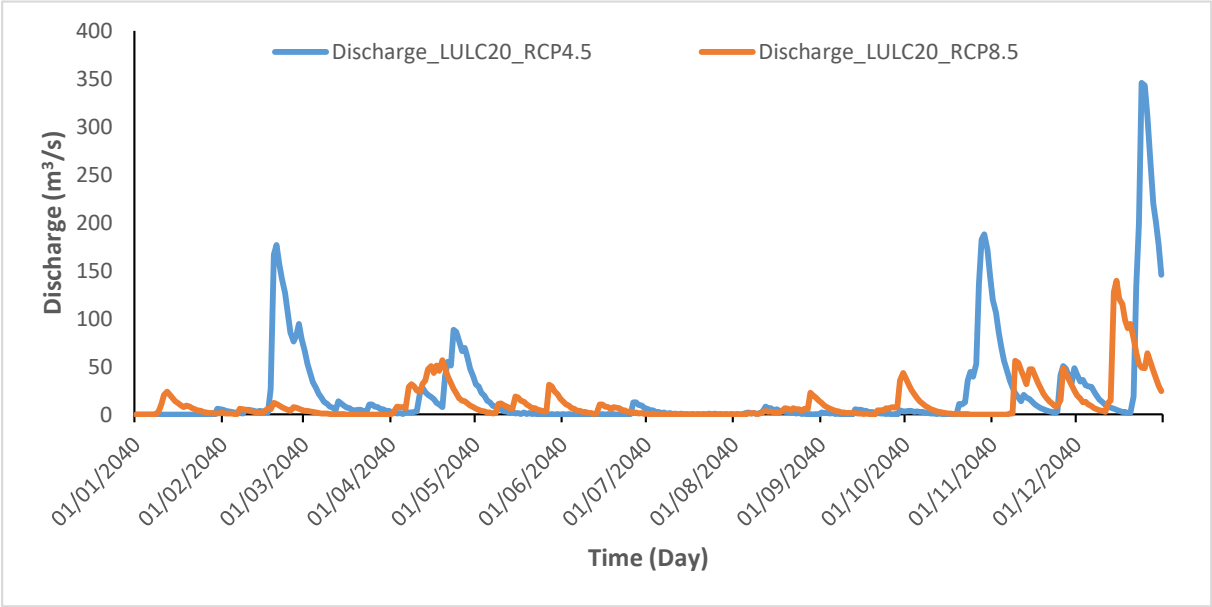

Figure 42. Comparison of simulated RCP 4.5 and RCP 8.5 hydrographs for the event storm from 01/01/2040 to 31/12/2040 in the case of the LULC 2020.

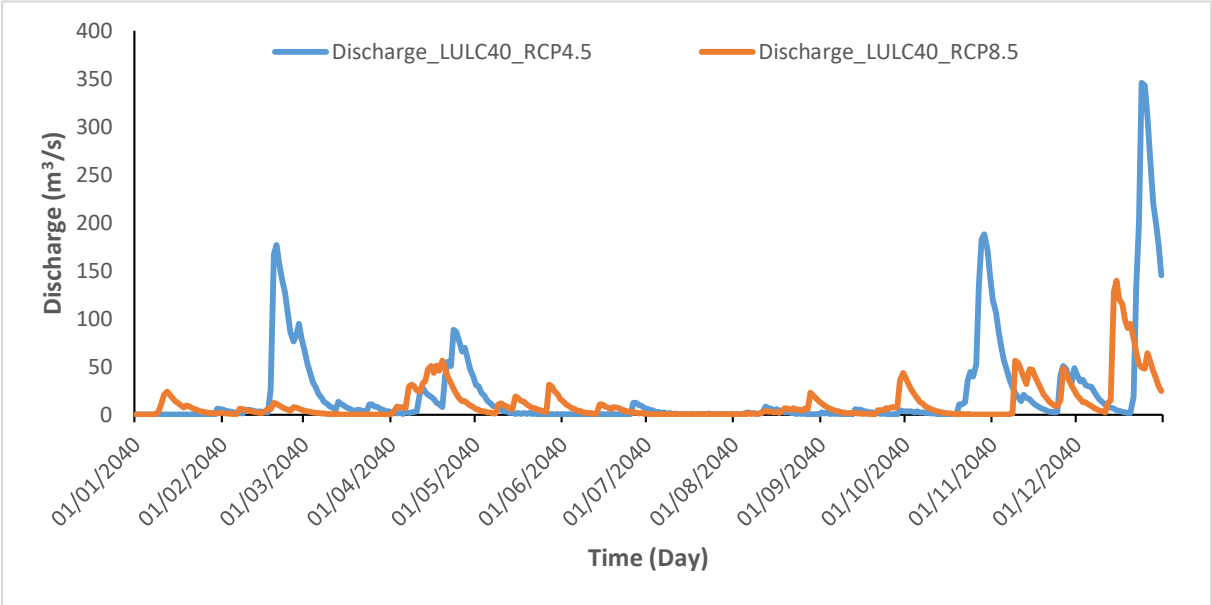

Figure 43. Comparison of simulated RCP 4.5 and RCP 8.5 hydrographs for the event storm from 01/01/2040 to 31/12/2040 in the case of the LULC 2040.

The simulated discharge values for RCP 4.5 were found to be higher than values generated with RCP 8.5 scenario data for both the 2020 and 2040 experiments. From a comparison of RCP scenario perspective, the results show that RCP 8.5 scenario resulted in a peak discharge that was on average 17.16% lower than the ones simulated under the RCP 4.5 scenario, while the volume runoff was 14.77% higher, for the 2020 event storm. Similarly the 2040 event storm show, on average, a decrease of approximately 59.71% in peak discharge and a decrease of 44.55% in volume runoff, between RCP 4.5 and RCP 8.5. The results suggest the RCP 8.5 scenario generates less severe flood events than the RCP 4.5 scenario. This is consistent with the notion that the RCP 8.5 scenario involves higher greenhouse gas concentrations and elevated radiative forcing, which may result in more severe changes in critical indicators such as river flow, water temperature, and precipitation. However, from a LULC change perspective, the simulated results between 1985 and 2040, under RCP 4.5, display an increase of 0.91% peak discharge and a rise of 0.09% runoff volume, for the 2020 storm event. For the 2040 storm event, an increase of 0.09% in peak discharge and rise of 0.21% in runoff volume was shown. Under RCP 8.5, peak discharge increased by 0.09% and runoff volume augmented by 0.37%, for the 2020 storm event. Moreover, an increase by 0.21% in in peak discharge and a rise of 0.60% in runoff volume were observed for the 2040 storm event. The increase in CN value and a decrease in lag time value, caused by the expansion of built-up lands and agricultural lands were noted to be the reason for the increase in peak discharge and runoff volume, between 1985 and 2040.

Impacts of Climate Change and LULC Change on Runoff

To further assess the distinct impact of climate change and LULC change, The One factor at time (OFAT) approach (Yang et al., 2017) was applied on simulated results. The four experiments, E1 (1985 – 2003), E2 (1985 – 2020), E3 (1985 – 2040) and E4 (2020-2040), were considered for the analysis, in Table 25. For each time interval, four different scenarios (S1, S2, S3, and S4) were evaluated to understand the isolated impact of climate change and LULC change on the hydrological process. The comparison between S1 and S4 represent the combined impacts of climate change and LULC change, for each experiment, denoted as ΔQ. The comparison of S1-S3 and S2-S4 reveals the extent of climate change's influence (ΔQC). The comparison of S1-S2 and

S3-S4 shows the magnitude of the influence of LULC change (ΔQL). Table 26 shows the simulated peak runoff results different climate and LULC scenarios.

Table 25. Simulated peak discharge under different climate change and LULC change scenarios.

Experiment	Scenario	LULC Period	Storm Event	Simulated peak Discharge (m3/s)
E1	S1	1985	18/12/1984 - 31/07/1985	351.4
	S2	2003	18/12/1984 - 31/07/1985	351.4
	S3	1985	01/01/2003 – 31/07/2003	163.2
	S4	2003	01/01/2003 – 31/07/2003	162.7
E2	S1	1985	18/12/1984 - 31/07/1985	351.4
	S2	2020	18/12/1984 - 31/07/1985	353.8
	S3	1985	01/01/2020 – 31/12/2020	130.6
	S4	2020	01/01/2020 – 31/12/2020	131.6
E3	S1	1985	18/12/1984 - 31/07/1985	351.4
	S2	2040	18/12/1984 - 31/07/1985	358.2
	S3	1985	01/01/2040 – 31/12/2040	345.6
	S4	2040	01/01/2040 – 31/12/2040	345.9
E4 RCP 4.5	S1	2020	01/01/2020 – 31/12/2020	131.6
	S2	2040	01/01/2020 – 31/12/2020	131.8
	S3	2020	01/01/2040 – 31/12/2040	345.8
	S4	2040	01/01/2040 – 31/12/2040	345.9
E4 RCP 8.5	S1	2020	01/01/2020 – 31/12/2020	108.8
	S2	2040	01/01/2020 – 31/12/2020	108.9
	S3	2020	01/01/2040 – 31/12/2040	139.4
	S4	2040	01/01/2040 – 31/12/2040	139.4

Table 26. The results of separating the impacts of climate change and LULC change.

Experiment	Time frame	ΔQC	ΔQL	ΔQ	Climate change Impact	LULC change Impact
E1	1985-2003	-188.45	-0.25	-188.7	99.867	0.133
E2	1985-2020	-221.50	1.70	-223.2	99.238	0.761
E3	1985-2040	-9.05	3.55	-12.6	71.825	28.174
E4 RCP 4.5	2020-2040	214.15	0.15	214.3	99.930	0.070
E4 RCP 8.5	2020-2040	30.55	0.05	30.6	99.836	0.163

.

The simulated runoff generally declined for E1, E2, E3 by 188.7 m^3/s, 223.2m^3/s and 12.6 m^3/s, (-53.70%, -62.55%, -1.57%), respectively. However, for E4 under RCP 4.5 and E4 under RCP 8.5, the simulated runoff increased by 214.3 m^3/s and 30.6 m^3/s, (162.84%, 28.13%), respectively. Thus, representing a noticeable impact caused by the combined influence of climate change and LULC change (ΔQ) for each timeframe. The results suggested that, due to climate variations, runoff decreased by -188.45 m^3/s, -221.5 m^3/s and -9.05 m^3/s, expressing an impact rate (ΔQC) of 99.867%, 99.238% and 71.825%, for E1, E2 and E3 respectively. In contrast, runoff increased, for E4 under RCP 4.5 and E4 under RCP 8.5, by 214.15 m^3/s and 30.55 m^3/s, accounting for an impact rate (ΔQC) of 99.930% and 99.836%, respectively. LULC change also appeared to decrease insignificantly the runoff for E1 by -0.25 m^3/s conveying an impact rate (ΔQL) of 0.133%. As for E2, E3, E4 under RCP 4.5 and E4 under RCP 8.5, the LULC change show a minor runoff increase by 1.7 m^3/s, 3.55 m^3/s, 0.15 m^3/s, 0.05 m^3/s, reflecting an impact rate (ΔQL) of 0.761%, 28.174%, 0.07% and 0.163%, respectively. The transition in LULC within E3, from 1985 to 2040, is significant. This change correlates the rise in runoff with the expansion of agricultural lands, water bodies, and a noticeable increase in built-up areas at the expense of forests and barren lands. This period stands out as the most impactful in terms of LULC change. Overall, the study shows that the impact of climate alteration exceeded by far the impact of LULC variation (**Table 26**). The influence of LULC changes has primarily resulted in increased runoff, except for the interval from 1985 to 2003. Conversely, climate change has generally led to a decrease in runoff, except for the period from 2020 to 2040. The period from 2020 to 2040 is expected to experience significant changes in (LULC) and climate that will affect soil erosion, sediment yields and floods. Hence, it is a crucial timeframe for planning the construction of future hydraulic structures, some of which will be utilized to combat these issues and their associated risks.

Current meteorological data Trend Analysis

Trend analysis for rainfall, temperature and discharge data were conducted for averaged mean monthly and annual data of three stations Azzaba, Ain Charchar and Zit Emba. Standard statistical procedures, present in Hydrolab, were used to fill gaps in time series data on portions of the records from 1970-2010. Average daily precipitation and temperature, across the basin were derived using Thiessen polygon method, in ArcGIS. The Mann-Kendall (MK) test and Sen's slope estimator served to analyze averaged mean monthly and annual data.

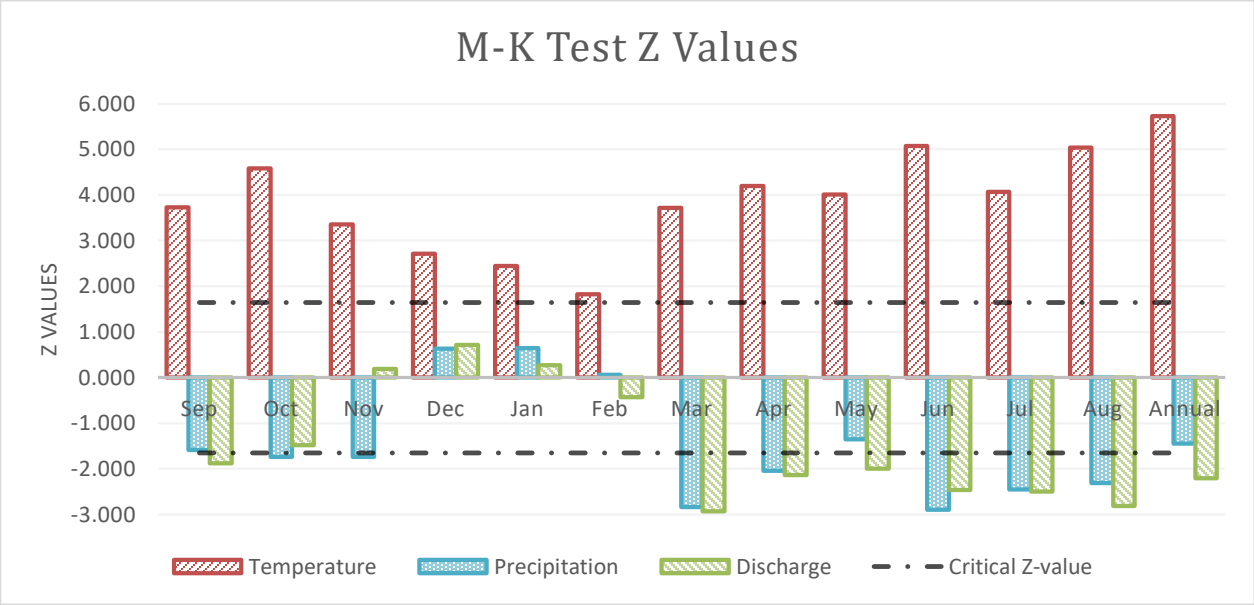

Figure 44. Mann–Kendall test results for runoff, precipitation, and temperature (α = 10%).

This MK test analysis based on Z-value revealed some distinct trends for the three variables, with varying significance in certain months throughout the entire period (Figure 44). When considering precipitation, the null hypothesis (H0) was accepted for five months (September, December, January, February, and May). H0 was also accepted in discharge analysis between October and February. The absolute calculated Z value is found to be lesser than the critical value (±1.645) in those months, indicating no consistent trend were observed in these instances. In this context, the MK test statistic S, calculated based on data ranking, is considered. When S differs notably from 0, H0 is rejected in favor of the alternative hypothesis (Ha) of a monotonic trend (Alemu and Dioha, 2020). The magnitude of the trend is estimated using Sen's slope estimator as shown in Tables 27 - 29 and Figures 45 - 49.

Analysis of rainfall data

Averaged mean monthly and annual precipitation data, covering the period 1970 to 2010, were used in the analysis.

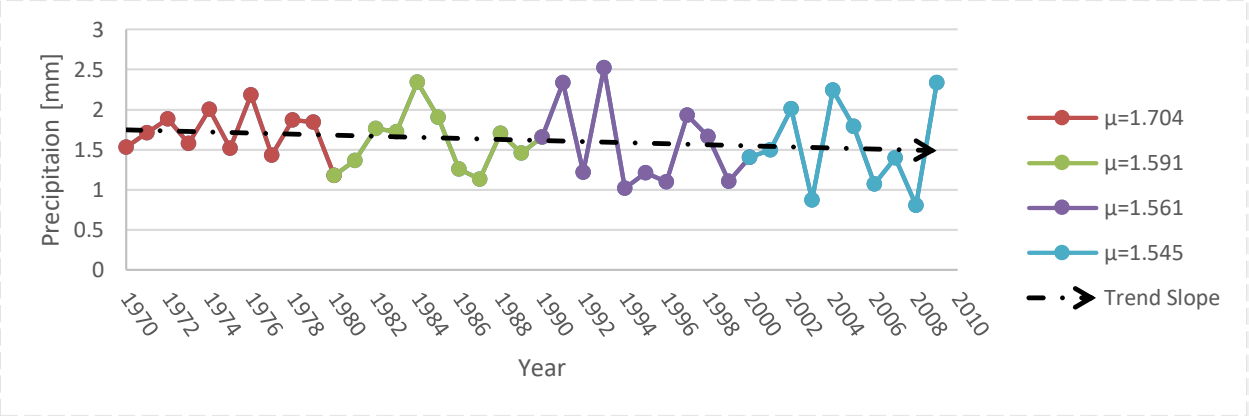

Figure 45. Mean annual rainfall trend, decadal mean (μ) and Sen's slope.

The Mann Kendall test ran across annual and monthly data showed that p-values were above the significant level of alpha of 0.1 in 5 months, as well as the mean annual precipitation (Table 27). In addition, the absolute calculated Z value is found to be lesser than the critical value (±1.645) for those months. The consideration of S being different from zero was acknowledged. Sen.'s slope presented an overall negative slope trend, it was however positive for the months from October to February. This indicates a general decreasing pattern in precipitation from 1970 to 2010 (Figures 45 and 46).

Table 27. Mann Kendal and Sen.'s Slope test results for precipitation analysis.

Variable	Tau	S	Var(S)	Z	p-Value	Beta (Sen Slope)
Sep	-0.177	-137	7357	-1.586	0.113	-0.017
Oct	-0.193	-150	7362.667	-1.736	0.082	-0.020
Nov	-0.193	150	7362.667	-1.736	0.082	0.019
Dec	0.071	55	7363.667	0.629	0.529	0.017
Jan	0.072	56	7365.667	0.641	0.524	0.015
Feb	0.008	6	7365.667	0.058	0.954	0.002
Mar	-0.313	-244	7364.667	-2.832	0.004	-0.049
Apr	-0.226	-176	7362.667	-2.039	0.041	-0.028
May	-0.150	-117	7361.667	-1.352	0.176	-0.012
Jun	-0.325	-248	7295.333	-2.892	0.004	-0.008
Jul	-0.294	-197	6397	-2.451	0.014	-0.002
Aug	-0.261	-198	7291.333	-2.307	0.021	-0.004
Annual	-0.160	-125	7365.667	-1.445	0.149	-0.011

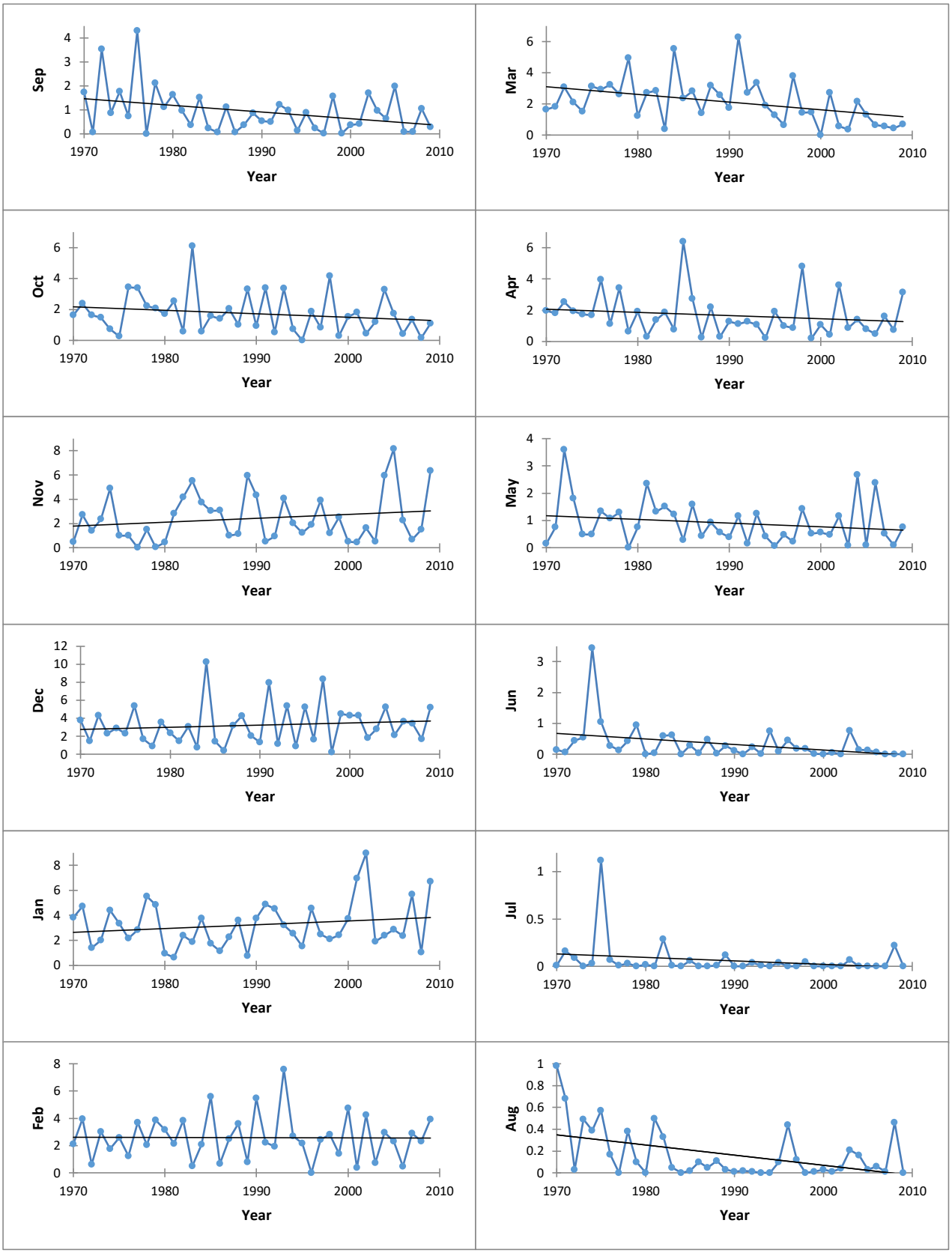

Figure 46. Monthly precipitation trend and Sen.'s slope over the period 1970-2010.

Analysis of temperature data

Averaged mean monthly and annual temperature data, covering the period 1970 to 2010, were used in the analysis.

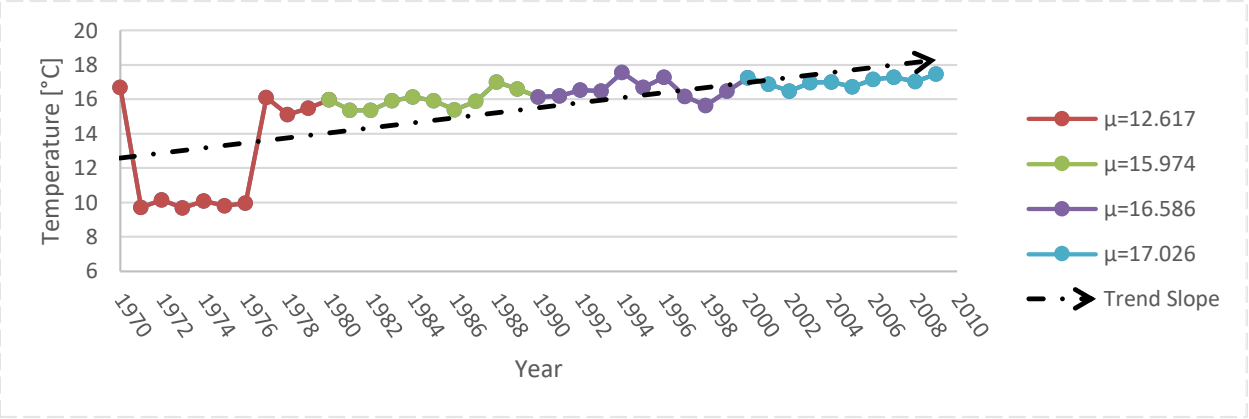

Figure 47. Mean annual temperature trend, decadal mean (μ) and Sen's slope.

The Mann Kendall test ran across annual and monthly data showed that p-values were all inferior to the significant level of alpha of 0.1 (Table 28). In addition, the calculated Z values are found to be superior to the critical value (±1.645) for all months, revealing that there was a significant increasing trend observed. Sen.'s slope presented an overall positive slope trend, indicating an increasing pattern in temperature from 1970 to 2010 (Figures 47 and 48).

Table 28. Mann Kendal and Sen.'s Slope test results for temperature analysis.

Variable	Tau	S	Var(S)	Z	p-Value	Beta (Sen Slope)
Sep	0.412	321	7363.667	3.729	0.000	0.110
Oct	0.505	394	7363.667	4.580	< 0.0001	0.157
Nov	0.371	289	7365.667	3.356	0.001	0.091
Dec	0.300	234	7364.667	2.715	0.007	0.067
Jan	0.271	211	7365.667	2.447	0.014	0.045
Feb	0.203	158	7365.667	1.829	0.067	0.045
Mar	0.410	320	7365.667	3.717	0.000	0.113
Apr	0.463	361	7365.667	4.195	< 0.0001	0.110
May	0.443	345	7365.667	4.008	< 0.0001	0.150
Jun	0.559	436	7365.667	5.069	< 0.0001	0.163
Jul	0.449	350	7365.667	4.066	< 0.0001	0.111
Aug	0.556	433	7363.667	5.034	< 0.0001	0.140
Annual	0.632	492	7362.667	5.722	< 0.0001	0.074

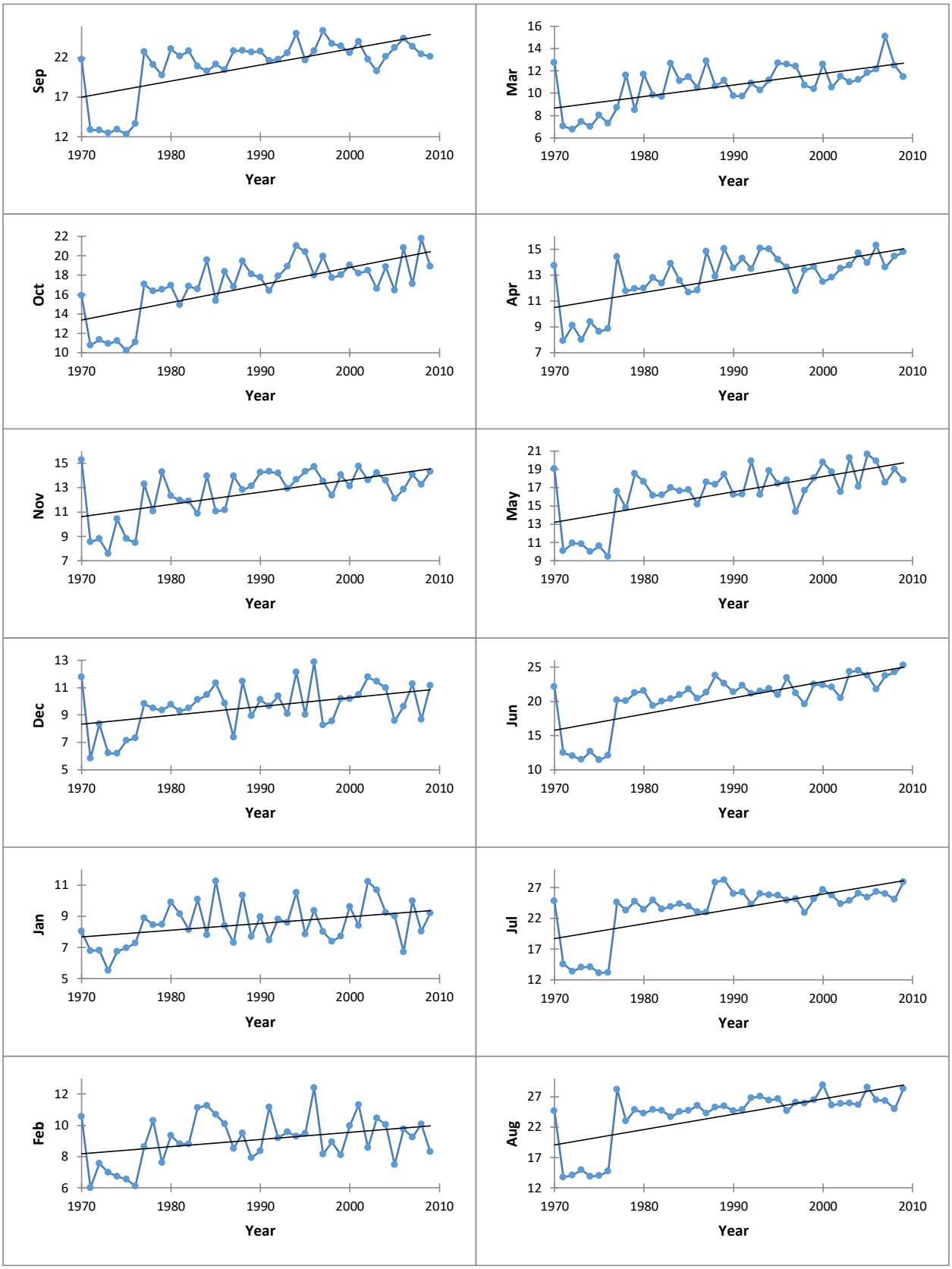

Figure 48. Monthly temperature trend and Sen.'s slope over the period 1970-2010.

Analysis of runoff data

Averaged mean monthly and annual runoff data, covering the period 1970 to 2010, were used in the analysis.

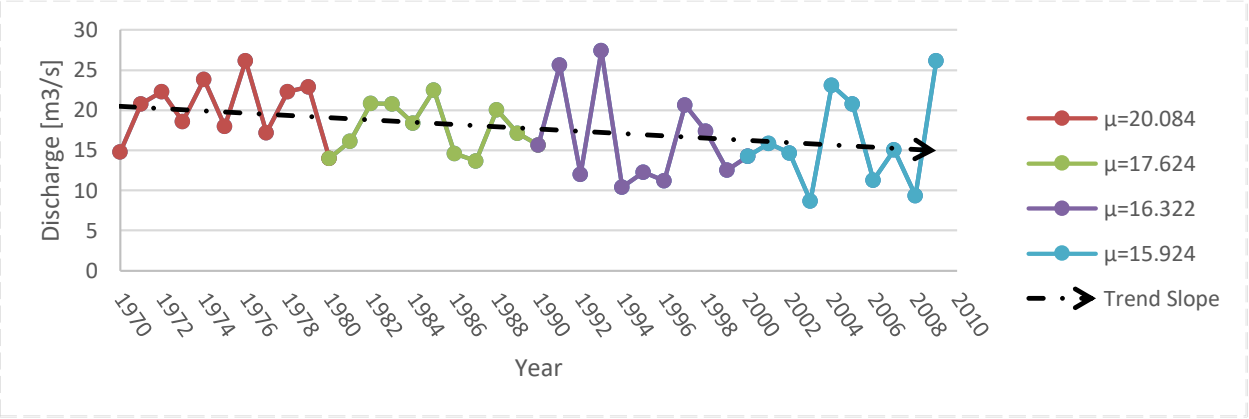

Figure 49. Mean annual runoff trend, decadal mean (μ) and Sen's slope.

The Mann Kendall test ran across annual and monthly data showed that p-values were above the significant level of alpha of 0.1 from October to February (Table 29). In addition, the calculated Z value is found to be inferior to the critical value (±1.645) for those months. The consideration of S being different from zero was acknowledged. Sen.'s slope displayed a generally negative slope trend, except for the months November, December, and January, where it was positive, demonstrating a declining pattern in runoff from 1970 to 2010. (Figures 49 and 50).

Table 29. Mann Kendal and Sen.'s Slope test results for runoff analysis.

Variable	Tau	S	Var(S)	Z	p-Value	Beta (Sen Slope)
Sep	-0.208	-162	7364.667	-1.8761	0.060	-0.139
Oct	-0.164	-128	7364.667	-1.4799	0.140	-0.202
Nov	0.022	17	7365.667	0.1864	0.852	0.025
Dec	0.079	62	7365.667	0.7108	0.480	0.208
Jan	0.031	24	7365.667	0.2680	0.790	0.05
Feb	-0.049	-38	7365.667	-0.4311	0.669	-0.114
Mar	-0.323	-252	7365.667	-2.9246	0.003	-0.584
Apr	-0.236	-184	7365.667	-2.1323	0.032	-0.359
May	-0.221	-172	7365.667	-1.9925	0.046	-0.191
Jun	-0.272	-212	7364.667	-2.4587	0.013	-0.104
Jul	-0.279	-215	7331.667	-2.4993	0.012	-0.012
Aug	-0.314	-242	7335.333	-2.8139	0.005	-0.032
Annual	-0.244	-190	7364.667	-2.2023	0.028	-0.178

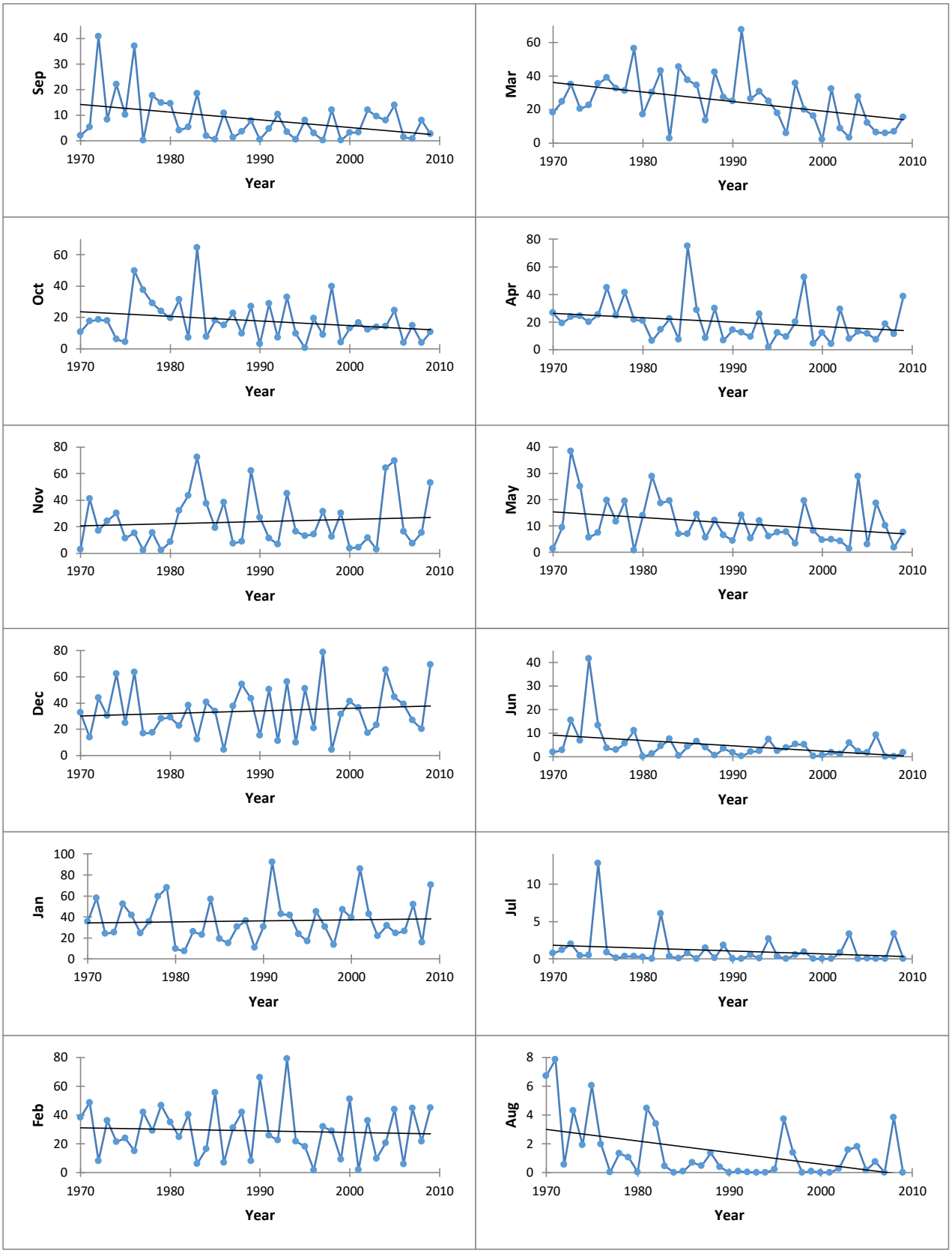

Figure 50. Monthly runoff trend and Sen.'s slope over the period 1970-2010.

Climatic data Trend Analysis

Trend analysis was performed on bias-adjusted RCM-simulated rainfall and temperature data (max and min) for the period from 2020 to 2060 under Representative Concentration Pathways scenarios 4.5 and 8.5. Daily RCM-simulated precipitation and temperature averages across the basin were calculated using the Thiessen polygon method in ArcGIS. Subsequently, discharge data was generated, via HEC-HMS, with the aforementioned data, to be then used in a trend analysis. The Mann-Kendall test and Sen's slope estimator served to analyze averaged mean monthly and annual data.

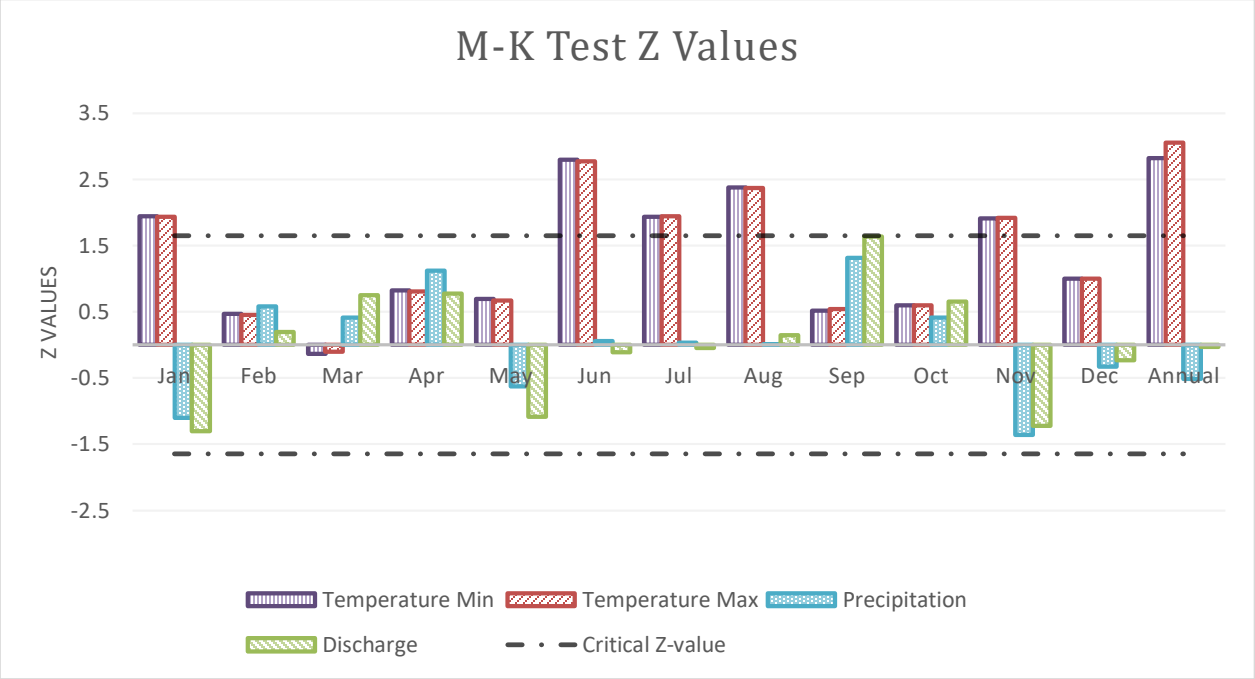

Figure 51. Mann–Kendall test results for simulated runoff, precipitation, and temperature under RCP 4.5 (α = 10%).

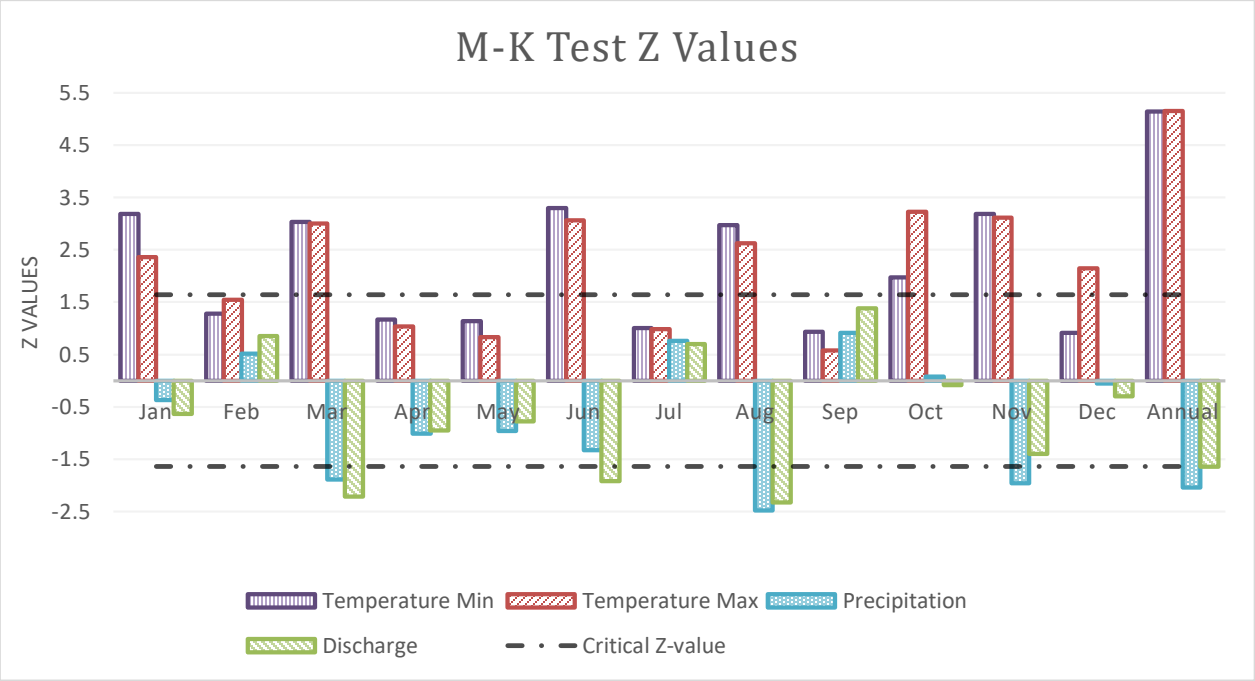

Figure 52. Mann–Kendall test results for simulated runoff, precipitation, and temperature under RCP 8.5 (α = 10%).

Figures 51 and 52, illustrate Mann-Kendall (MK) test analysis, based on Z-values, under two emission gas scenarios RCP4.5 and RCP8.5, respectively. The null hypothesis (H0) was mostly accepted. The absolute calculated Z value is found to be lesser than the critical value (±1.645) in majority, suggesting that there is little evidence of a trend in the data. This requires relying on the significance of the S statistics to interpret the trend and Sen's slope to establish its magnitude, as mention previously. Subsequently, climatic and hydrologic factors were examined individually to identify distinct trends, as shown below.

Analysis of simulated rainfall data under RCP4.5

Averaged mean monthly and annual precipitation data, covering the period 2020 to 2060, were used in the analysis.

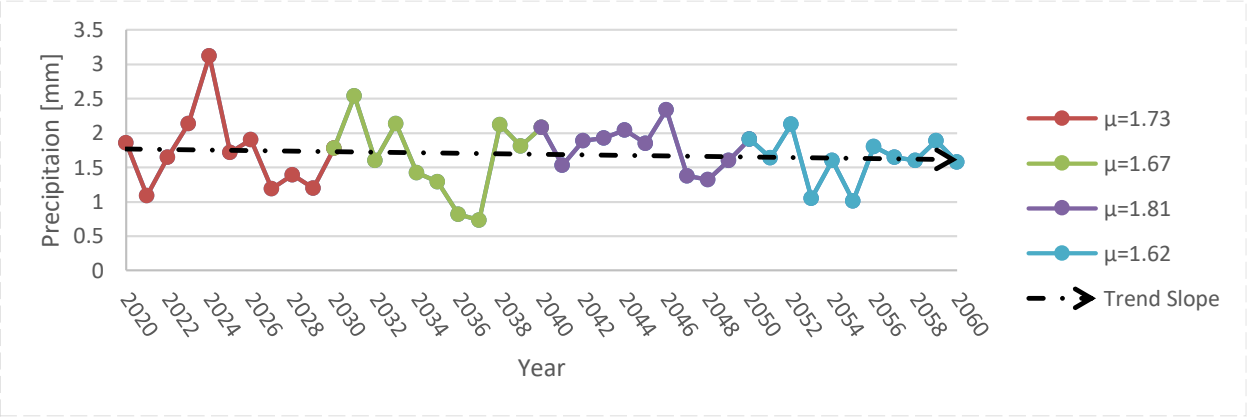

Figure 53. Mean annual simulated rainfall trend under RCP4.5, decadal mean and Sen's slope.

The Mann Kendall test ran across annual and monthly data showed that p-values were above the significant level of alpha of 0.1 in all months, as well as the mean annual precipitation (Table 30). In addition, the absolute calculated Z value is found to be lesser than the critical value (±1.645) for all instances. The consideration of S being different from zero was acknowledged. Sen.'s slope presented a minor positive slope trend for most months, it was however negative for the months January, May, July and November. The annual Sen's slope is negative indicating a decreasing pattern in precipitation from 2020 to 2060 (Figure 53 - Figure 54).

Table 30. Mann Kendal and Sen.'s Slope test results for RCP 4.5 simulated rainfall analysis.

Variable	Tau	S	Var(S)	Z	p-Value	Beta (Sen Slope)
Jan	-0.121	-99	7925.667	-1.100	0.271	-0.027
Feb	0.065	53	7925.667	0.584	0.559	0.013
Mar	0.046	38	7922.667	0.416	0.678	0.010
Apr	0.123	101	7923.667	1.123	0.261	0.020
May	-0.070	-57	7923.667	-0.629	0.529	-0.005
Jun	0.007	6	7908.667	0.056	0.955	0.003
Jul	0.005	4	7850.667	0.034	0.973	-0.002
Aug	0.002	2	7885.333	0.011	0.991	0.001
Sep	0.144	118	7922.000	1.315	0.189	0.010
Oct	0.046	38	7924.667	0.416	0.678	0.009
Nov	-0.149	-122	7922.667	-1.359	0.174	-0.029
Dec	-0.037	-30	7922.667	-0.326	0.746	-0.012
Annual	-0.058	-47	7915.000	-0.517	0.605	-0.002

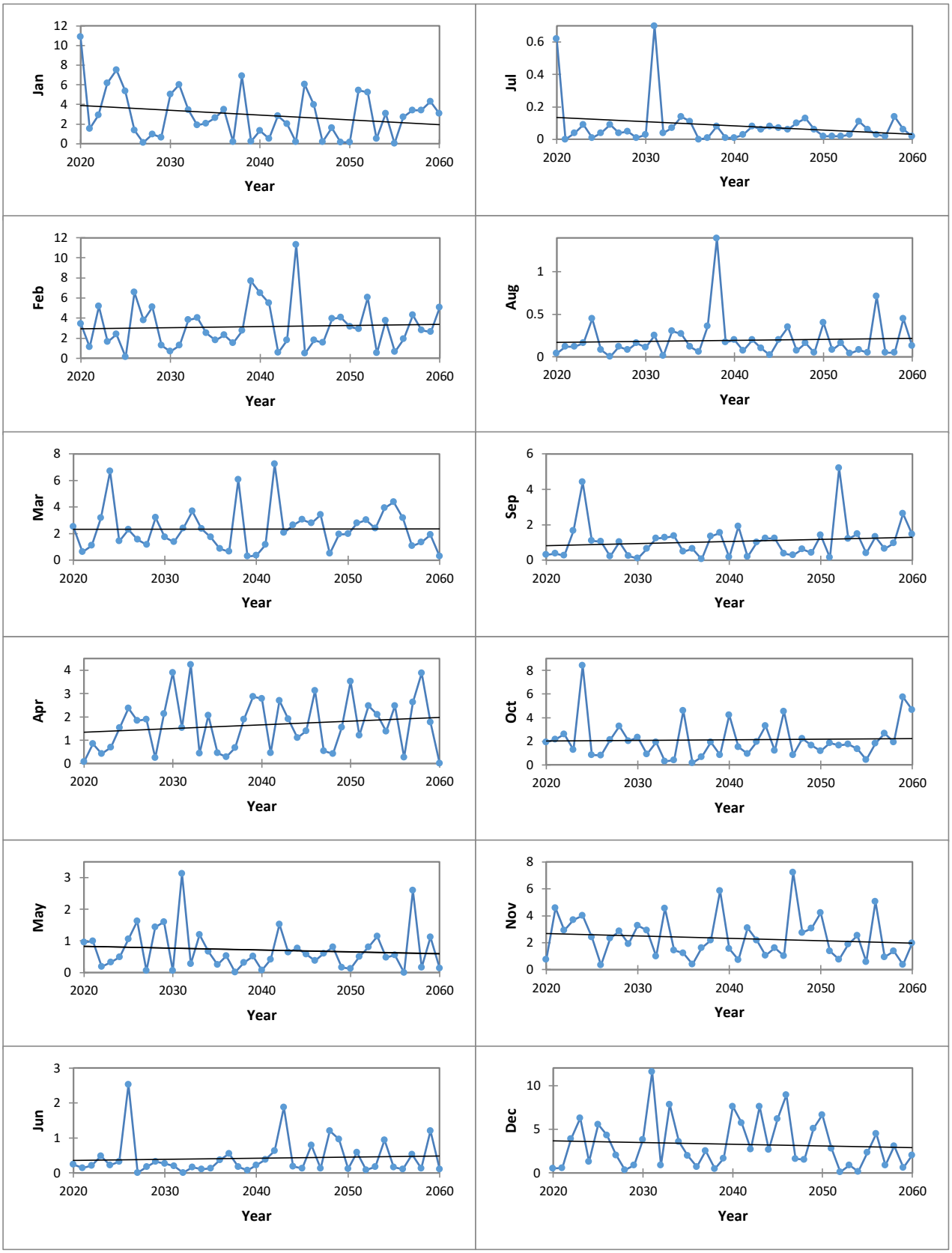

Figure 54. Monthly RCP4.5 simulated precipitation trend and Sen.'s slope over the period 2020-2060.

Analysis of simulated maximum temperature data under RCP4.5

Averaged max monthly and annual temperature data, covering the period from 2020 to 2060, were used in the analysis.

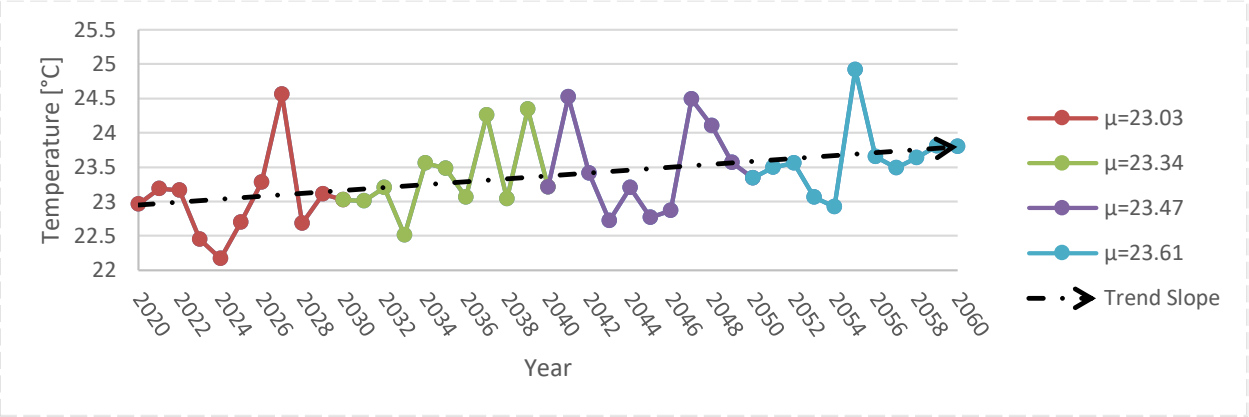

Figure 55. Maximum annual simulated temperature trend under RCP4.5, decadal mean and Sen's slope.

The Mann Kendall test ran across annual and monthly data showed that p-values were under the significant level of alpha of 0.1 for January, June, July, August and November, as well as the min annual temperature (Table 31). In addition, the absolute calculated Z value is found to be superior than the critical value (±1.645) for all instances. The consideration of S being different from zero was acknowledged. Sen.'s slope presented a minor positive slope trend for all months, except for the month of Mars. The annual Sen's slope is positive indicating a slightly increasing pattern in maximum temperature from 2020 to 2060 (Figure 55 and 56).

Table 31. Mann Kendal and Sen.'s Slope test results for RCP 4.5 simulated maximum temperature analysis.

Variable	Tau	S	Var(S)	Z	p-Value	Beta (Sen Slope)
Jan	0.211	173	7925.667	1.932	0.053	0.040
Feb	0.050	41	7925.667	0.449	0.653	0.009
Mar	-0.012	-10	7924.667	-0.101	0.919	-0.002
Apr	0.089	73	7925.667	0.809	0.419	0.017
May	0.074	61	7925.667	0.674	0.500	0.010
Jun	0.302	248	7924.667	2.775	0.005	0.045
Jul	0.212	174	7924.667	1.943	0.052	0.034
Aug	0.259	212	7924.667	2.370	0.018	0.043
Sep	0.060	49	7925.667	0.539	0.590	0.012
Oct	0.066	54	7924.667	0.595	0.552	0.007
Nov	0.210	172	7924.667	1.921	0.055	0.044
Dec	0.110	90	7924.667	0.999	0.317	0.018
Annual	0.334	273	7923.667	3.056	0.002	0.021

Figure 56. Monthly RCP4.5 simulated maximum temperature trend and Sen.'s slope over the period 2020-2060.

Analysis of simulated minimum temperature data under RCP4.5

Averaged min monthly and annual temperature data, covering the period from 2020 to 2060, were used in the analysis.

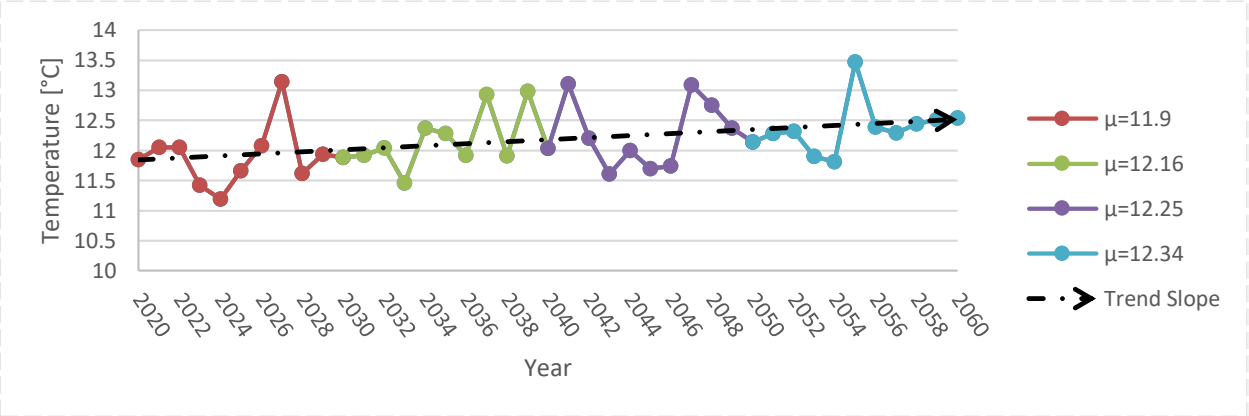

Figure 57. Minimum annual simulated temperature trend under RCP4.5, decadal mean and Sen's slope.

The Mann Kendall test ran across annual and monthly data showed that p-values were under the significant level of alpha of 0.1 for January, June, July, August and November, as well as the min annual temperature (Table 32). In addition, the absolute calculated Z value is found to be superior than the critical value (±1.645) for all instances. The consideration of S being different from zero was acknowledged. Sen.'s slope presented a minor positive slope trend for all months, except for the month of Mars. The annual Sen's slope is positive indicating a slightly increasing pattern in minimum temperature from 2020 to 2060 (Figure 57 and 58).

Table 32. Mann Kendal and Sen.'s Slope test results for RCP 4.5 simulated minimum temperature analysis.

Variable	Tau	S	Var(S)	Z	p-Value	Beta (Sen Slope)
Jan	0.213	174	7922.667	1.944	0.052	0.033
Feb	0.053	43	7923.667	0.472	0.637	0.008
Mar	-0.016	-13	7923.667	-0.135	0.893	-0.002
Apr	0.090	74	7923.667	0.820	0.415	0.015
May	0.077	63	7923.667	0.697	0.486	0.009
Jun	0.305	250	7924.667	2.797	0.005	0.036
Jul	0.211	173	7925.667	1.932	0.053	0.023
Aug	0.260	213	7923.667	2.382	0.017	0.032
Sep	0.057	47	7923.667	0.517	0.605	0.009
Oct	0.066	54	7924.667	0.595	0.552	0.006
Nov	0.209	171	7925.667	1.910	0.056	0.039
Dec	0.110	90	7924.667	0.999	0.317	0.015
Annual	0.308	252	7922.667	2.82	0.005	0.017

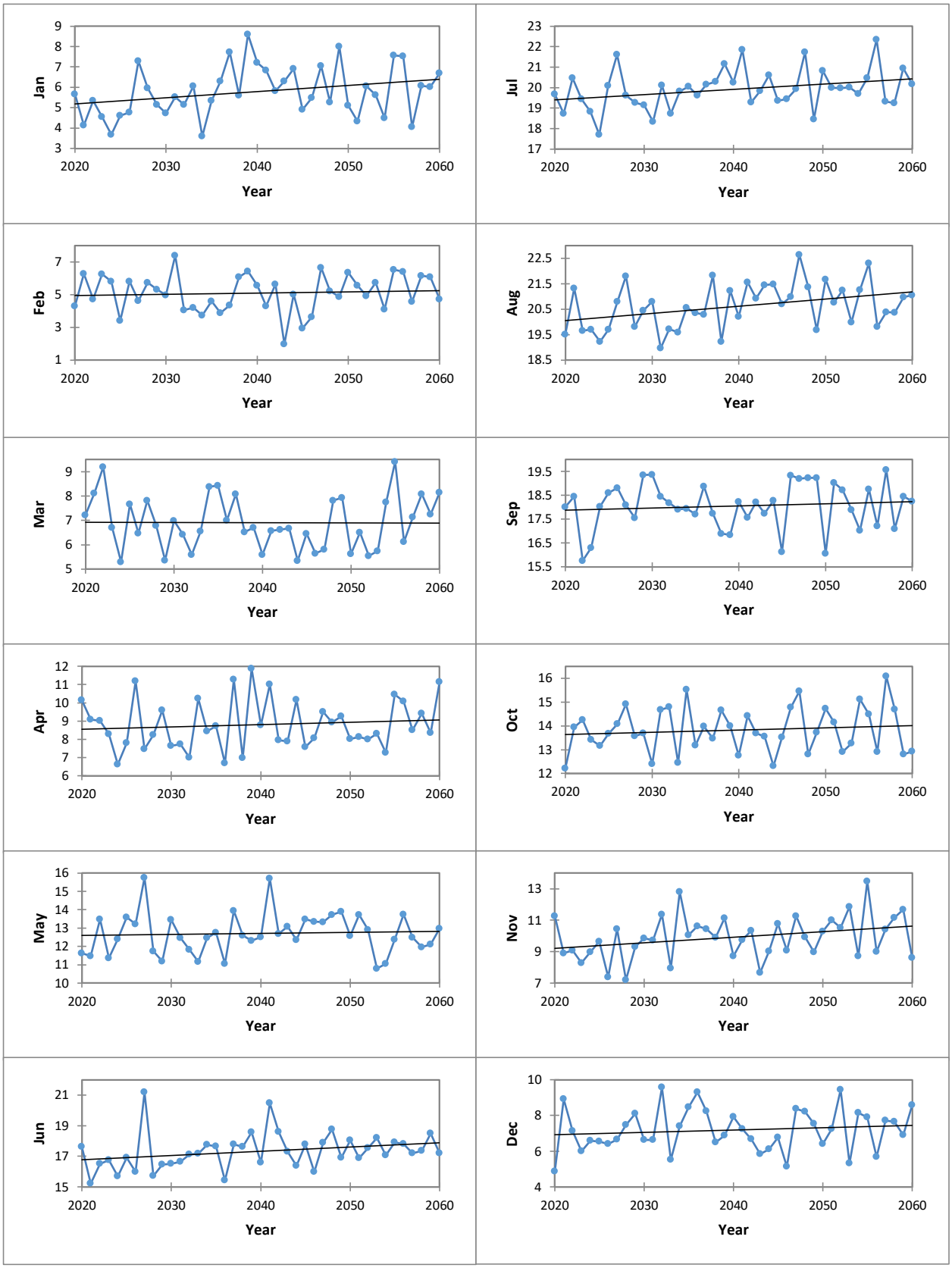

Figure 58. Monthly RCP4.5 simulated minimum temperature trend and Sen.'s slope over the period 2020-2060.

Analysis of simulated runoff data under RCP4.5

Averaged mean monthly and annual runoff data, covering the period from 2020 to 2060, were used in the analysis.

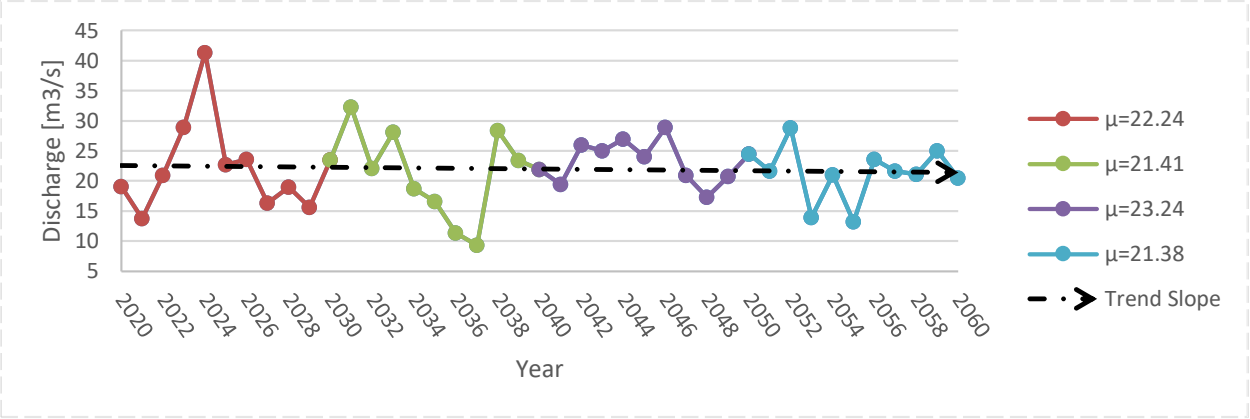

Figure 59. Mean annual simulated runoff trend under RCP4.5, decadal mean and Sen's slope.

The Mann Kendall test ran across annual and monthly data showed that p-values were above the significant level of alpha of 0.1 for all months, as well as the mean annual runoff (Table 33). In addition, the absolute calculated Z value is found to be lesser than the critical value (±1.645) for all instances. The consideration of S being different from zero was acknowledged. Sen.'s slope presented a positive slope trend for six months, and was negative for six months. The mean runoff annual Sen's slope is negative indicating a minor decreasing pattern in runoff from 2020 to 2060 (Figure 59 and 60).

Table 33. Mann Kendal and Sen.'s Slope test results for RCP 4.5 simulated runoff analysis.

Variable	Tau	S	Var(S)	Z	p-Value	Beta (Sen Slope)
Jan	-0.143	-117	7925.667	-1.303	0.193	-0.468
Feb	0.022	18	7923.667	0.191	0.850	0.096
Mar	0.083	68	7923.667	0.753	0.454	0.165
Apr	0.085	70	7925.667	0.775	0.441	0.186
May	-0.120	-98	7923.667	-1.09	0.278	-0.094
Jun	-0.013	-11	7925.667	-0.112	0.911	-0.006
Jul	-0.006	-5	7921.667	-0.045	0.964	-0.003
Aug	0.017	14	7922.667	0.146	0.884	0.003
Sep	0.179	147	7925.667	1.64	0.101	0.163
Oct	0.072	59	7925.667	0.651	0.515	0.099
Nov	-0.134	-110	7921.667	-1.225	0.223	-0.239
Dec	-0.027	-22	7921.667	-0.236	0.815	-0.079
Annual	-0.005	-4	7924.667	-0.034	0.973	-0.0006

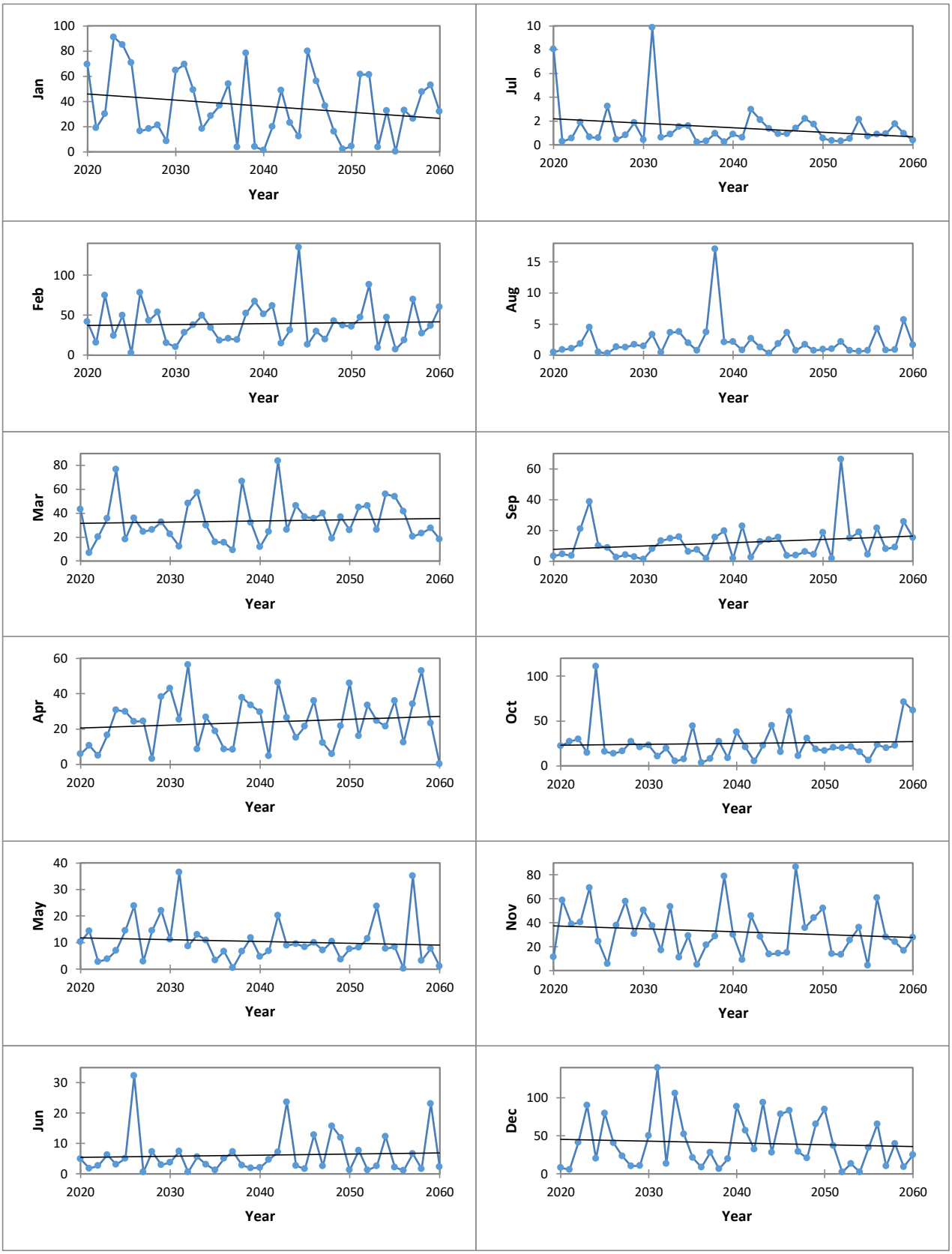

Figure 60. Monthly RCP4.5 simulated runoff trend and Sen.'s slope over the period 2020-2060.

Analysis of simulated rainfall data under RCP8.5

Averaged mean monthly and annual precipitation data, covering the period 2020 to 2060, were used in the analysis.

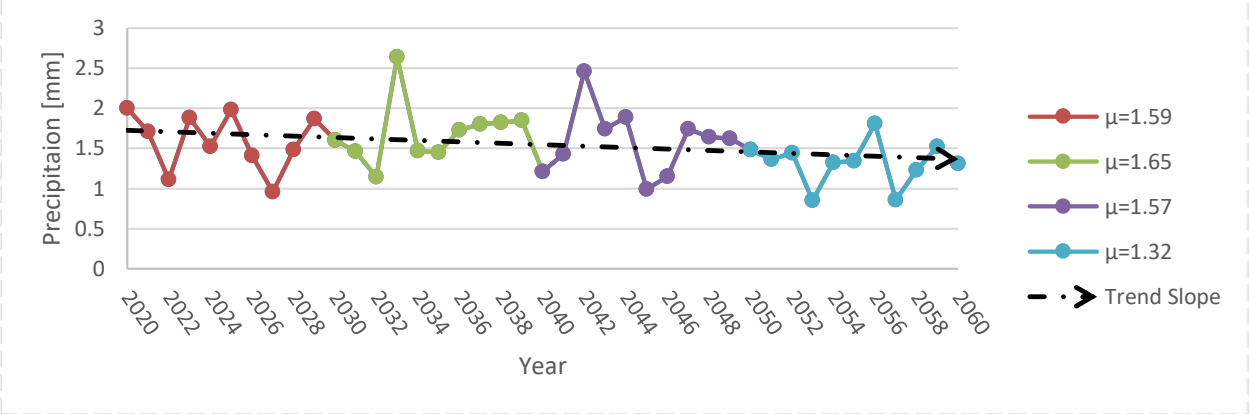

Figure 61. Mean annual simulated rainfall trend under RCP8.5, decadal mean and Sen's slope.

The Mann Kendall test ran across annual and monthly data showed that p-values were under the significant level of alpha of 0.1 in Mars, August, November, as well as the mean annual precipitation (Table 34). The absolute calculated Z value, for those instances, is found to be superior to the critical value (±1.645). The consideration of S being different from zero was acknowledged. Sen.'s slope presented mainly a negative slope trend, it was however positive for the months February, July, September and October. The annual Sen's slope is negative indicating a decreasing pattern in precipitation from 2020 to 2060 (Figure 61 and 62).

Table 34. Mann Kendal and Sen.'s Slope test results for RCP 8.5 simulated rainfall analysis.

Variable	Tau	S	Var(S)	Z	p-Value	Beta (Sen Slope)
Jan	-0.042	-34	7924.667	-0.371	0.711	-0.007
Feb	0.057	47	7925.667	0.517	0.605	0.006
Mar	-0.206	-169	7923.667	-1.887	0.059	-0.03
Apr	-0.111	-91	7925.667	-1.011	0.312	-0.016
May	-0.106	-87	7923.667	-0.966	0.334	-0.008
Jun	-0.146	-119	7919.667	-1.326	0.185	-0.005
Jul	0.087	68	7788.667	0.759	0.448	0.0003
Aug	-0.273	-222	7907.333	-2.485	0.013	-0.004
Sep	0.100	82	7920.000	0.91	0.363	0.006
Oct	0.010	8	7912.333	0.079	0.938	0.001
Nov	-0.215	-176	7924.667	-1.966	0.049	-0.029
Dec	-0.007	-6	7924.667	-0.056	0.955	-0.002
Annual	-0.224	-183	7923.667	-2.045	0.041	-0.009

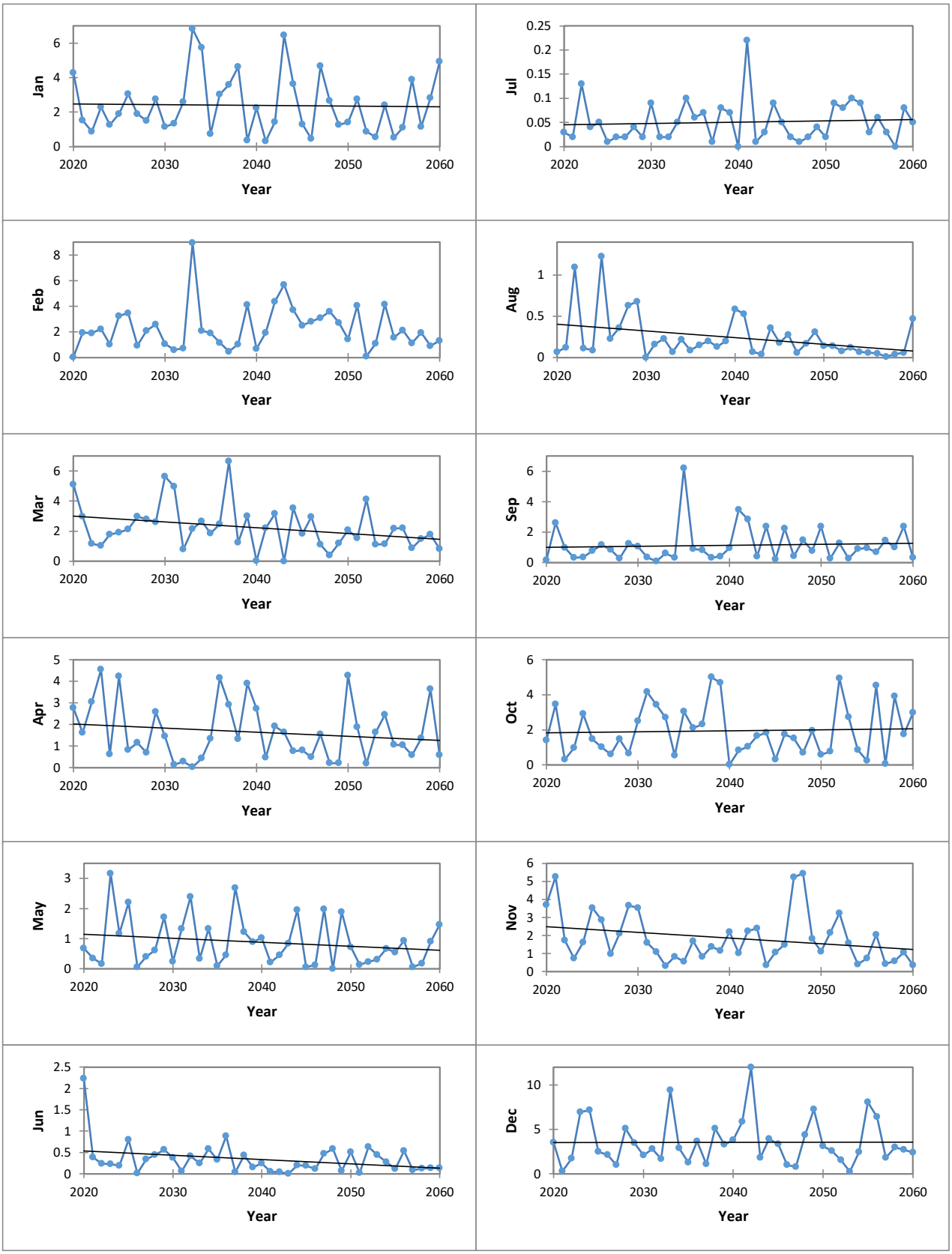

Figure 62. Monthly RCP8.5 simulated precipitation trend and Sen.'s slope over the period 2020-2060.

Analysis of simulated maximum temperature data under RCP8.5

Averaged max monthly and annual temperature data, covering the period from 2020 to 2060, were used in the analysis.

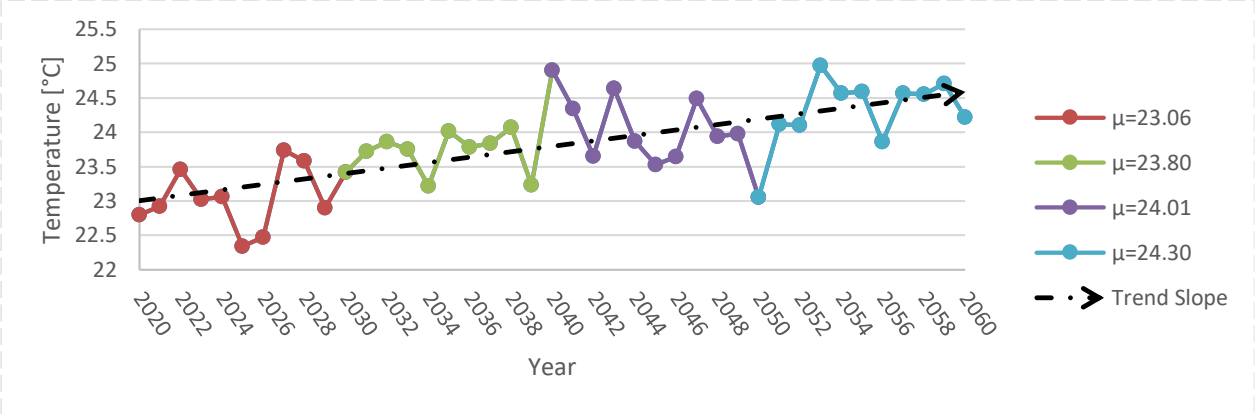

Figure 63. Maximum annual simulated temperature trend under RCP8.5, decadal mean and Sen's slope.

The Mann Kendall test ran across annual and monthly data showed that p-values were above the significant level of alpha of 0.1 for April, Mars, July and September (Table 35). In addition, the absolute calculated Z value is found to be inferior to the critical value (±1.645) for those instances. The consideration of S being different from zero was acknowledged. Sen.'s slope presented mainly a positive slope trend. The annual Sen's slope is positive indicating a slightly increasing pattern in maximum temperature from 2020 to 2060 (Figure 63 and 64).

Table 35. Mann Kendal and Sen.'s Slope test results for RCP 8.5 simulated maximum temperature analysis.

Variable	Tau	S	Var(S)	Z	p-Value	Beta (Sen Slope)
Jan	0.257	211	7925.667	2.359	0.018	0.037
Feb	0.170	139	7923.667	1.550	0.121	0.038
Mar	0.327	268	7924.667	2.999	0.003	0.063
Apr	0.113	93	7925.667	1.033	0.301	0.017
May	0.092	75	7925.667	0.831	0.406	0.016
Jun	0.334	274	7925.667	3.067	0.002	0.065
Jul	0.109	89	7925.667	0.988	0.323	0.022
Aug	0.287	235	7925.667	2.628	0.009	0.047
Sep	0.063	52	7924.667	0.573	0.567	0.009
Oct	0.351	288	7924.667	3.224	0.001	0.056
Nov	0.339	278	7924.667	3.112	0.002	0.063
Dec	0.234	192	7924.667	2.146	0.031	0.056
Annual	0.562	460	7925.667	5.156	< 0.0001	0.039

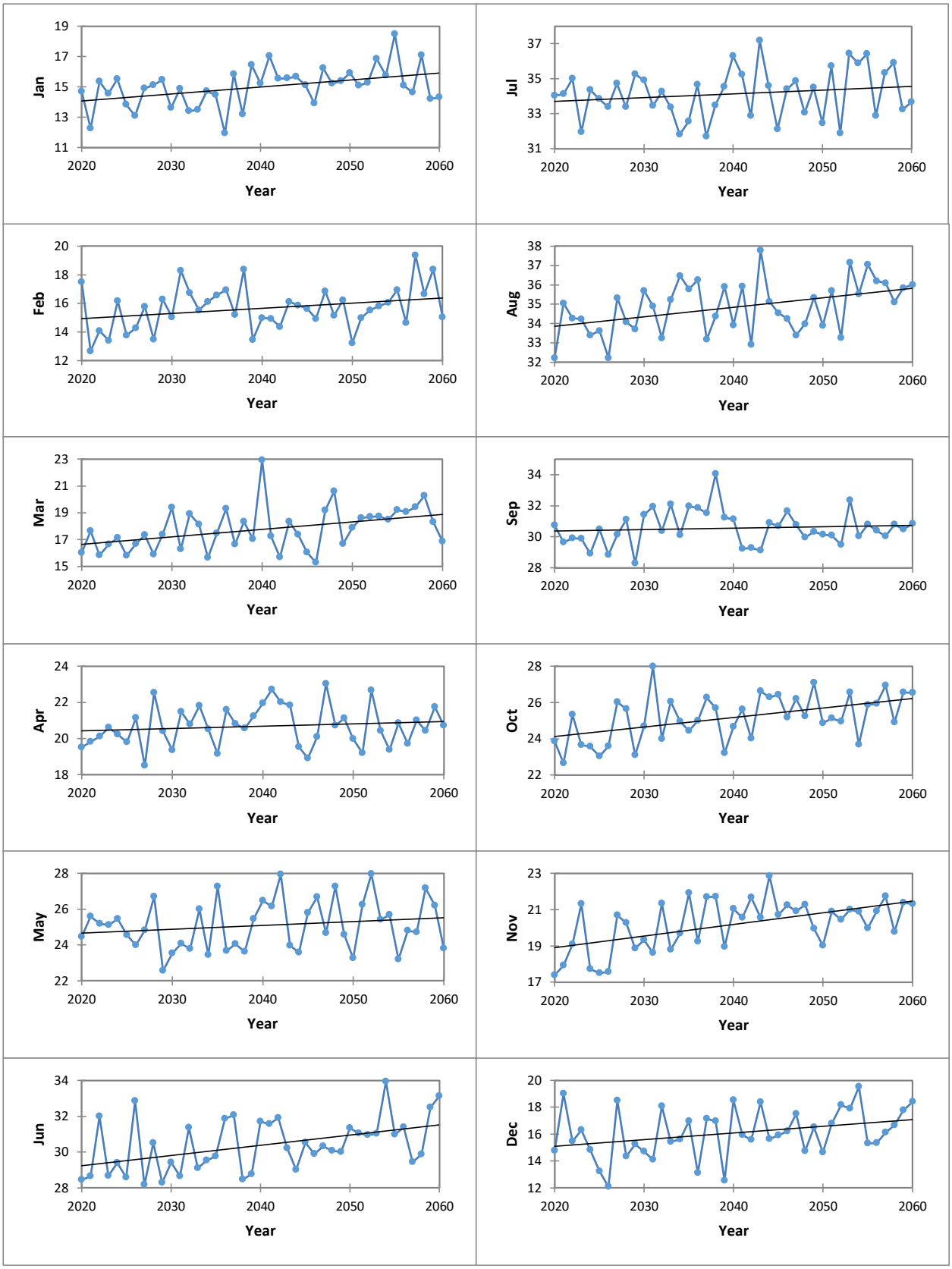

Figure 64. Monthly RCP8.5 simulated maximum temperature trend and Sen.'s slope over the period 2020-2060.

Analysis of simulated minimum temperature data under RCP8.5

Averaged max monthly and annual temperature data, covering the period from 2020 to 2060, were used in the analysis.

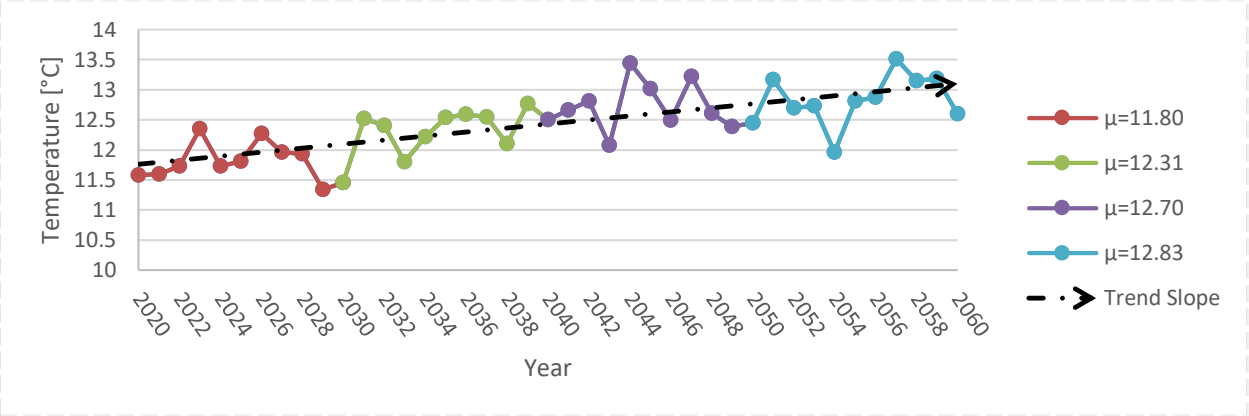

Figure 65. Minimum annual simulated temperature trend under RCP8.5, decadal mean and Sen's slope.

The Mann Kendall test ran across annual and monthly data showed that p-values were above the significant level of alpha of 0.1 for February, April, May, July, September and December (Table 36). The absolute calculated Z value is found to be lesser than the critical value (±1.645) for those instances. The consideration of S being different from zero was acknowledged. Sen.'s slope presented mainly a positive slope trend. The annual Sen's slope is positive indicating a slightly increasing pattern in minimum temperature from 2020 to 2060 (Figure 65 - Figure 66).

Table 36. Mann Kendal and Sen.'s Slope test results for RCP 8.5 simulated minimum temperature analysis.

Variable	Tau	S	Var(S)	Z	p-Value	Beta (Sen Slope)
Jan	0.348	285	7925.667	3.19	0.001	0.045
Feb	0.140	115	7925.667	1.281	0.200	0.022
Mar	0.331	271	7923.667	3.033	0.002	0.050
Apr	0.128	105	7925.667	1.168	0.243	0.019
May	0.125	102	7924.667	1.135	0.257	0.025
Jun	0.360	295	7925.667	3.302	0.001	0.054
Jul	0.110	90	7925.667	0.999	0.320	0.016
Aug	0.324	266	7925.667	2.977	0.003	0.047
Sep	0.102	84	7925.667	0.932	0.354	0.012
Oct	0.216	177	7923.667	1.977	0.048	0.038
Nov	0.348	285	7925.667	3.190	0.001	0.064
Dec	0.100	82	7925.667	0.910	0.365	0.022
Annual	0.561	459	7923.667	5.145	< 0.0001	0.035

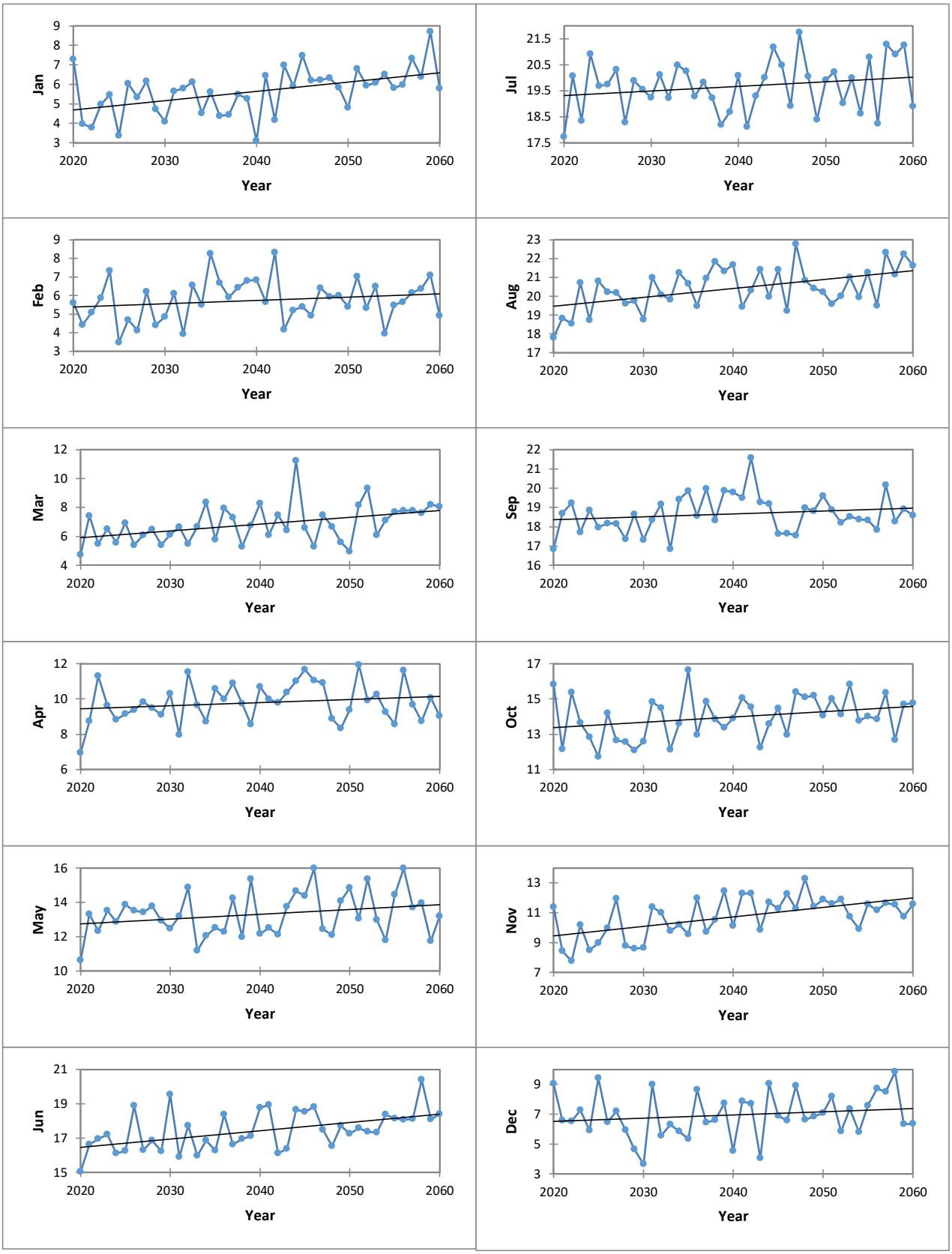

Figure 66. Monthly RCP8.5 simulated minimum temperature trend and Sen.'s slope over the period 2020-2060.

Analysis of simulated runoff data under RCP8.5

Averaged mean monthly and annual runoff data, covering the period from 2020 to 2060, were used in the analysis.

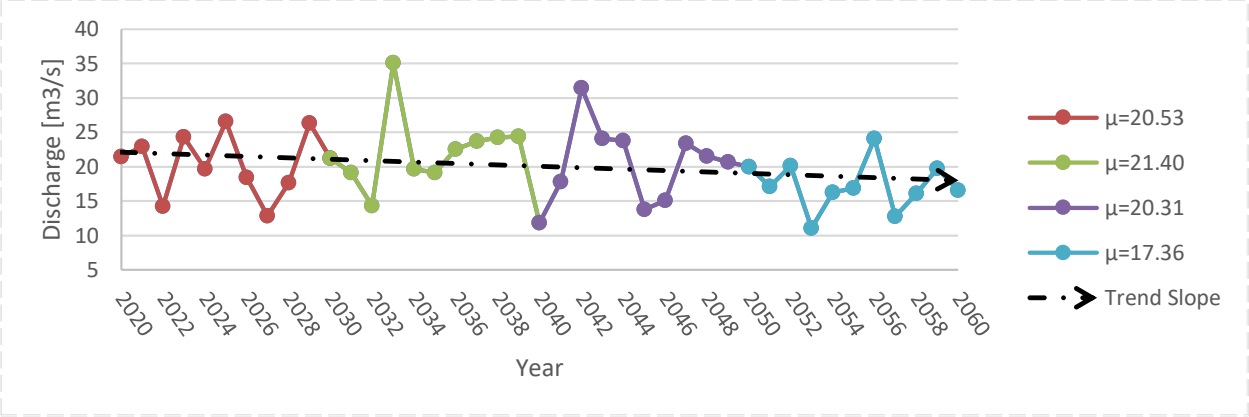

Figure 67. Mean annual simulated runoff trend under RCP8.5, decadal mean and Sen's slope.

The Mann Kendall test ran across annual and monthly data showed that p-values were under the significant level of alpha of 0.1 for Mars, June and August (Table 37). In addition, the absolute calculated Z value is found to be superior to the critical value (±1.645) for those instances. The consideration of S being different from zero was acknowledged. Sen.'s slope presented a negative slope trend for most months, except for the months February, July and September. The mean annual Sen's slope is negative indicating a slightly decreasing pattern in runoff from 2020 to 2060 (Figure 67 and 68).

Table 37. Mann Kendal and Sen.'s Slope test results for RCP 8.5 simulated runoff analysis.

Variable	Tau	S	Var(S)	Z	p-Value	Beta (Sen Slope)
Jan	0.001	-58	7923.667	-0.640	0.998	-0.002
Feb	0.094	77	7925.667	0.854	0.393	0.198
Mar	-0.241	-198	7923.667	-2.213	0.026	-0.497
Apr	-0.105	-86	7923.667	-0.955	0.342	-0.172
May	-0.085	-70	7925.667	-0.775	0.441	-0.099
Jun	-0.210	-172	7923.667	-1.921	0.054	-0.097
Jul	0.077	63	7921.667	0.697	0.486	0.004
Aug	-0.254	-208	7924.667	-2.325	0.020	-0.031
Sep	0.151	124	7925.667	1.382	0.168	0.126
Oct	-0.011	-9	7925.667	-0.090	0.928	-0.019
Nov	-0.154	-126	7925.667	-1.404	0.161	-0.298
Dec	-0.034	-28	7925.667	-0.303	0.763	-0.109
Annual	-0.179	-147	7925.667	-1.640	0.101	-0.101

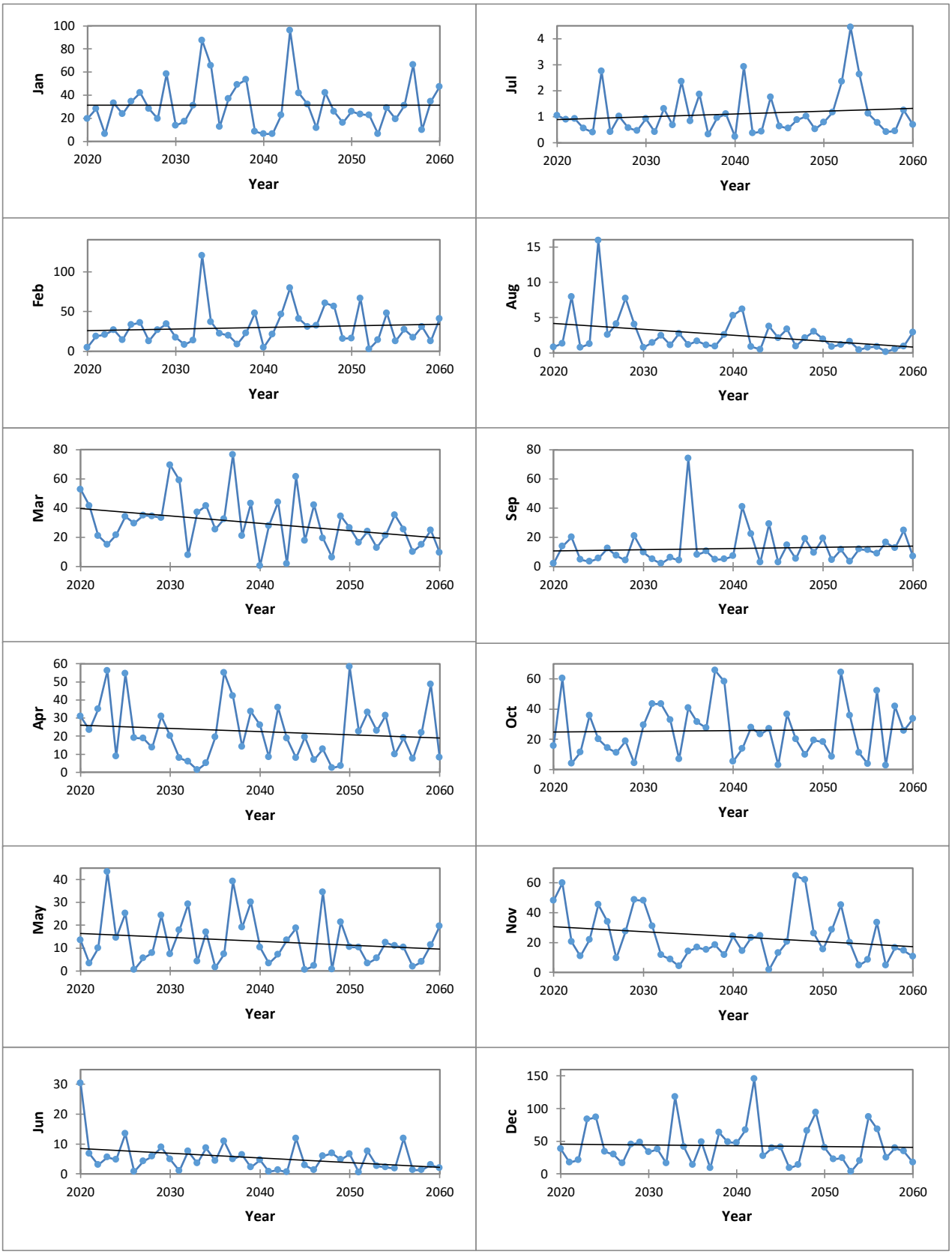

Figure 68. Monthly RCP8.5 simulated runoff trend and Sen.'s slope over the period 2020-2060.

Through trend analysis, a clear correlation between precipitation and runoff was observed. The results indicate a similar trend in which an increase in precipitation levels, particularly observed around winter and the beginning of autumn in RCP simulated climatic data, corresponds to an increase in runoff. In contrast, when precipitation decreases, so do runoff.

The analysis, incorporating both current data and climatic simulations, indicates an increase in temperature. Generally, precipitation and discharge decrease over the decades as shown by the decline of decadal mean from 2020 to 2060. However, within this trend, from 2030 to 2040, both precipitation and discharge are projected to increase. Subsequently, from 2040 to 2060, these trends are expected to reverse, with precipitation and discharge on the decline. The observed trends in precipitation, runoff, and temperature, as well as the projections for future changes, should be taken into consideration by water management planners to ensure sustainable water resource management. Additionally, the simulations under both the RCP4.5 and RCP8.5 scenarios produced comparable results. This similarity can be attributed to the region's largely agricultural character, with low industrial activity and hence insignificant gas emissions.

This chapter presents the findings of our study, highlighting the LULC maps derived from classification and MOLUSCE modeling. Transition matrices illustrate the changes in land use/land cover over the selected periods (1985, 2003, 2020, and 2040), revealing significant urban expansion and agricultural development at the expense of forests and barren lands. Notably, the implementation of the Zit Emba Dam in 2003 resulted in an increase in water body areas.

Simulation results from the HEC-HMS model, encompassing calibration, validation, and predictions under two RCP scenarios, demonstrated satisfactory model performance. The hydrological analysis indicated an overall decrease in discharge, with LULC changes contributing to increased peak discharge and runoff volumes due to urbanization, while climate change exerted a counteracting effect.

One-Factor-At-a-Time (OFAT) results confirmed that climate change had a more dominant impact on discharge than land use/land cover changes. Additionally, the trend analysis revealed a global rise in temperature within the basin, accompanied by a correlated decrease in precipitation and discharge. Similar patterns were observed for both RCP scenarios, attributed to the region's agricultural nature, which limits greenhouse gas emissions.

Conclusion

Water resources management and flood risk assessment are critical aspects that require thorough investigation and continuous monitoring in a catchment area. These investigations depend solely on understanding the influence of changes in Land Use and Land Cover (LULC) and climate on the catchment's hydrological response.

Remote sensing and geographic information systems (GIS) data have proven to be valuable tools in detecting and analyzing changes in discharge and runoff volume variations caused by LULC. Indeed, Landsat 5 and 7 data from 1985, 2003, and 2020 were classified to produce LULC maps for those periods. CA-ANN method integrated within the MOLUSCE plugin in QGIS was applied for data analysis and 2040 LULC projection. The error matrix and Kappa coefficient method were used for accuracy assessment on the classified images of 1985, 2003, and 2020 LULC maps. The overall accuracy is 99.27 % with a Kappa coefficient of 0.98. The LULC changes observed in the catchment between 1985 and 2040 indicate that the decrease in forests and barren lands (0.722% and 1.285%) is the reason for the increase in agricultural lands, water bodies, and built-up lands (0.403%, 0.584%, and 1.020%). Eventually, the hydrological model HEC-HMS, featuring the LULC maps, was used to simulate and analyze the impact of LULC changes in the Kebir river catchment.

Furthermore, the calibration of the model was conducted from 18/12/1984 to 31/07/1985, while the validation was performed from 01/01/2003 to 31/07/2003. The results depict that the Curve Number (CN) is the most sensitive parameter influencing peak discharge and runoff volume, during the calibration. The comparison of the simulated result using the four LULC maps, between 1985 and 2040, demonstrate a noticeable rise in peak discharge and runoff volume during both the calibration and validation periods. Specifically, there was an observed increase of 1.93% in peak discharge during the calibration period and a slightly higher increase of 2.20% in the validation period. Concurrently, the runoff volume exhibited a rise of 1.15% in the calibration period and a comparatively higher elevation of 1.53% in the validation period. These increments in both peak discharge and runoff volume were judged to be correlated with the expansion of urban areas and agricultural lands, associated with a loss in wooded areas, between 1985 and 2040.

Four common statistical indicators (RMSE, NSE, KGE, and R2) were applied to evaluate the performance of the HEC-HMS model for the Kebir river catchment during calibration and validation. The model results were found satisfactory for the RMSE, NSE, KGE, and R2 which

were 0.5, 0.701 to 0.720, 0.36 to 0.56, and 0.92 respectively during calibration and 0.60, 0.598 to 0.608, 0.31 to 0.34, and 0.86 to 0.87 respectively during validation.

Moreover, the impact of climate change and LULC changes on future discharges and runoff volume was evaluated. Data simulated by the RCA4-CNRM-CERFACS-CM5 model, based on two representative concentration pathways of greenhouse gas emission scenarios (RCP4.5 and 8.5), were adjusted via CMhyd. The Local Intensity Scaling (LOCI) and Variance Scaling (VS) approaches exhibited superior performance in correcting precipitation and temperature, respectively. The runoff hydrographs, generated from using these RCM simulated data and LULC maps, for the period from 01/01/2020 to 31/12/2020 and the Period 01/01/2040 to 31/12/2040, indicate that simulated discharge values for RCP 4.5 were found to be higher than values generated with RCP 8.5 scenario data for both periods. The results show that RCP 8.5 scenario resulted in a peak discharge that was on average 17.16% and 59.71% lower than the ones simulated under the RCP 4.5 scenario, for the 2020 and 2040 storm events respectively. While the volume runoff was 14.77% higher, for the 2020 event storm, between RCP 4.5 and RCP 8.5. It was 44.55% in lower, for the 2040 storm event. The LULC change, between 1985 and 2040, expedited an increase in peak discharge and run off volume for both storm events. Under RCP 4.5, peak discharge increased by 0.91% for the 2020 storm event and by 0.09% for the 2040 storm event. Under RCP 8.5, an increase of peak discharge by 0.09% and by 0.21% was observed for storm event 2020 and 2040 respectively. Runoff volume displayed a rise of 0.09% and of 0.21% for storm event 2020 and 2040 respectively, under RCP4.5. Additionally, under RCP8.5, Runoff volume increased by 0.37% and 0.60% for storm event 2020 and 2040 respectively. The expansion of built-up lands and agricultural lands were noted to be the reason for the negligible increase in peak discharge and runoff volume, between 1985 and 2040.

Subsequently, the isolated impact of climate change and LULC change on the hydrological process was examined, via the one factor at a time method (OFAT). Overall, the study shows that the impact of climate alteration exceeded by far the impact of LULC variation. The climate change impact rate were of 99.867%, 99.238%, 71.825%, for the time frames 1985-2003, 1985-2002, 1985-2040. Conversely, LULC change impact rates were of 0.133%, 0.761%, and 28.174% for the corresponding time frames. The period 1985-2040 as the most impactful in terms of LULC change. In the period 2020-2040, under RCP4.5, the climate change effect rate was 99.930%, while the LULC change impact rate was 0.070%. In contrast, under RCP8.5 over the same time frame, the

climate change effect rate was slightly lower at 99.836%, but the LULC change impact rate was considerably greater at 0.163%.

The trend analysis conducted on precipitation, discharge and temperature, between 1970-2010 and 2020-2060, reveals a noticeable rise in temperature over the years. While overall trends show a decrease in both precipitation and discharge over decades, projections suggest an increase from 2030 to 2040, followed by a decline from 2040 to 2060. Within this trend, a clear correlation between precipitation and runoff was observed. Both variables show an increase during winter and the beginning of autumn when using projected RCP simulated data. Conversely, they decrease during the rest of the year. The simulations under different RCP scenarios produce similar results due to the region's agricultural nature and low industrial activity, minimizing gas emissions. Water management planners should consider these trends for sustainable water resource management.

The modelling approach employed here holds potential applicability in diverse catchments that have encountered land use and land cover (LULC) alterations. This suggested procedure, combining GIS, CA-ANN (MOLUSCE) and HEC-HMS, proves highly valuable in comprehending the repercussions of LULC changes on the hydrological dynamics of a basin. Moreover, trend analysis, using the Mann-Kendall test, is extremely useful in evaluating the influence of climate change on hydrological components, particularly precipitation and discharge.

This study gave insights into probability to future change of hydrological components caused by climate and LULC changes. Climate variations findings aids policymakers in identifying months and periods prone to see increased discharge. Meanwhile, LULC variations outcomes provides insights for managing soils more effectively, thus mitigating the risk of increased discharge and runoff volume that often culminate in floods.

References

Abbas, Z., Jaber, H.S., 2020. Accuracy assessment of supervised classification methods for extraction land use maps using remote sensing and GIS techniques, in: IOP Conference Series: Materials Science and Engineering. Iop Publishing, p. 012166.

Abdelkebir, B., Maoui, A., Mokhtari, E., Engel, B., Chen, J., Aboelnour, M., 2021. Evaluating Low-Impact Development practice performance to reduce runoff volume in an urban watershed in Algeria. Arabian Journal of Geosciences 14, 814.

Abdulkareem, J.H., Pradhan, B., Sulaiman, W.N.A., Jamil, N.R., 2018. Review of studies on hydrological modelling in Malaysia. Modeling Earth Systems and Environment 4, 1577–1605.

Agus, F., Prafanto, A., Kamil, Z.A., 2023. Detecting land use land cover using supervised maximum likelihood algorithm on spatiotemporal imagery in Samarinda, Indonesia, in: IOP Conference Series: Earth and Environmental Science. IOP Publishing, p. 012085.

Ahmed, N., Wang, G., Booij, M.J., Xiangyang, S., Hussain, F., Nabi, G., 2022. Separation of the impact of landuse/landcover change and climate change on runoff in the upstream area of the Yangtze River, China. Water Resources Management 36, 181–201.

Alemu, Z.A., Dioha, M.O., 2020. Climate change and trend analysis of temperature: the case of Addis Ababa, Ethiopia. Environmental Systems Research 9, 1–15.

Allali, H., Elmeddahi, Y., Badni, N., El-nesr, M., 2023. Assessment of the Hydrological Responces to Land Use Changes in Wadi Ouahrane Watershed, Algeria. Russian Meteorology and Hydrology 48, 1084–1092.

Araya, Y.H., Cabral, P., 2010. Analysis and modeling of urban land cover change in Setúbal and Sesimbra, Portugal. Remote Sensing 2, 1549–1563.

Arfasa, G.F., Owusu-Sekyere, E., Doke, D.A., 2024. Climate Change Projections and Impacts on Future Temperature, Precipitation, and Stream flow in the Vea Catchment, Ghana. Environmental Challenges 14, 100813.

Arias, P., Bellouin, N., Coppola, E., Jones, R., Krinner, G., Marotzke, J., Naik, V., Palmer, M., Plattner, G.-K., Rogelj, J., 2021. Climate Change 2021: the physical science basis. Contribution of Working Group I to the Sixth Assessment Report of the Intergovernmental Panel on Climate Change; technical summary.

Astite, S.W., Kermani, S., Djediat, Y., 2023. The influence of the Land Use Land Cover (LULC) change on hydrological response in urbanized watersheds. Case study of Wadi Koriche and Wadi Kniss watersheds, northern Algeria. Arabian Journal of Geosciences 16, 242.

Bai, Y., Zhang, Z., Zhao, W., 2019. Assessing the impact of climate change on flood events using HEC-HMS and CMIP5. Water, Air, & Soil Pollution 230, 119.

Baig, M.F., Mustafa, M.R.U., Baig, I., Takaijudin, H.B., Zeshan, M.T., 2022. Assessment of land use land cover changes and future predictions using CA-ANN simulation for selangor, Malaysia. Water 14, 402.

Baláž, M., Danáčová, M., Szolgay, J., 2010. On the use of the Muskingum method for the simulation of flood wave movements. Slovak Journal of civil engineering 18, 14–20.

Baltas, E., Dervos, N., Mimikou, M., 2007. Technical Note: Determination of the SCS Initial Abstraction Ratio in an Experimental Watershed in Greece. Hydrology and Earth System Sciences 11. https://doi.org/10.5194/hess-11-1825-2007

Berg, P., Feldmann, H., Panitz, H.-J., 2012. Bias correction of high resolution regional climate model data. Journal of Hydrology 448, 80–92.

Bessaklia, H., Ghenim, A.N., Megnounif, A., Martín Vide, J., 2018. Spatial variability of concentration and aggressiveness of precipitation in North-East of Algeria. Journal of Water and Land Development, 2018, num. 36, p. 3-15.

Blissag, B., Yebdri, D., Kessar, C., 2024. Spatiotemporal change analysis of LULC using remote sensing and CA-ANN approach in the Hodna basin, NE of Algeria. Physics and Chemistry of the Earth, Parts A/B/C 133, 103535.

Blissag, B., Yebdri, D., Kessar, C., 2023. Spatiotemporal change analysis of LULC using remote sensing and CA-ANN approach in the Hodna basin, NE of Algeria. Physics and Chemistry of the Earth, Parts A/B/C 133, 103535.

Boyd, M.J., Bufill, M.C., Knee, R.M., 1993. Pervious and impervious runoff in urban catchments. Hydrological Sciences Journal 38, 463–478.

Brogli, R., Sørland, S.L., Kröner, N., Schär, C., 2019. Causes of future Mediterranean precipitation decline depend on the season. Environmental Research Letters 14, 114017.

Chandler, D.L., 2020. Why the Mediterranean is a climate change hotspot [WWW Document]. MIT News | Massachusetts Institute of Technology. URL https://news.mit.edu/2020/why-mediterranean-climate-change-hotspot-0617 (accessed 4.26.24).

Chen, J., Brissette, F.P., Leconte, R., 2011. Uncertainty of downscaling method in quantifying the impact of climate change on hydrology. Journal of hydrology 401, 190–202.

Chen, Y., Niu, J., Sun, Y., Liu, Q., Li, S., Li, P., Sun, L., Li, Q., 2020. Study on streamflow response to land use change over the upper reaches of Zhanghe Reservoir in the Yangtze River basin. Geoscience Letters 7, 1–12.

Congalton, R., 2001. Accuracy assessment and validation of remotely sensed and other spatial information. INTERNATIONAL JOURNAL OF WILDLAND FIRE 10, 321–328. https://doi.org/10.1071/WF01031

Da Silva, R.M., Santos, C.A., Moreira, M., Corte-Real, J., Silva, V.C., Medeiros, I.C., 2015. Rainfall and river flow trends using Mann–Kendall and Sen's slope estimator statistical tests in the Cobres River basin. Natural Hazards 77, 1205–1221.

Dede, M., Asdak, C., Setiawan, I., 2022. Spatial dynamics model of land use and land cover changes: A comparison of CA, ANN, and ANN-CA. Register: Jurnal Ilmiah Teknologi Sistem Informasi 8, 38–49.

Deng, X., Xu, Y., Han, L., Song, S., Yang, L., Li, G., Wang, Y., 2015. Impacts of urbanization on river systems in the Taihu Region, China. Water 7, 1340–1358.

Dennison, W.C., Thomas, J.E., Cain, C.J., Carruthers, T.J.B., Hall, M.R., Jesien, R.V., Wazniak, C.E., Wilson, D.E., 2009. Shifting sands: Environmental and cultural change in Maryland's Coastal Bays. University of Maryland Center for Environmental Science. Integration and Application Network Press, Cambridge 396.

Derdour, S., Ghenim, A.N., Megnounif, A., Tangang, F., Chung, J.X., Ayoub, A.B., 2022. Bias correction and evaluation of precipitation data from the CORDEX regional climate model for monitoring climate change in the Wadi Chemora Basin (Northeastern Algeria). Atmosphere 13, 1876.

Ekeroth, S., 2022. Developing a Rainfall-Runoff Routing Model using Spatially Distributed Travel Times: Modelling a Cloudburst Event in an Urban Catchment.

Feldman, A.D., 2000. Hydrologic Modeling System HEC-HMS, Technical Reference Manual.

Fleming, M., Brauer, T., 2018. Hydrologic Modeling System HEC-HMS, User's Manual.

Foley, A.M., 2010. Uncertainty in regional climate modelling: A review. Progress in Physical Geography 34, 647–670.

Ford, D., Pingel, N., DeVries, J.J., 2008. Hydrologic Modeling System HEC-HMS, Applications guide (updated by HEC), Computer software application guide.

Forootan, E., 2019. Analysis of trends of hydrologic and climatic variables.
Gashaw, T., Tulu, T., Argaw, M., Worqlul, A.W., 2018. Modeling the hydrological impacts of land use/land cover changes in the Andassa watershed, Blue Nile Basin, Ethiopia. Science of the Total Environment 619, 1394–1408.
Giorgi, F., Jones, C., Asrar, G.R., 2009. Addressing climate information needs at the regional level: the CORDEX framework. World Meteorological Organization (WMO) Bulletin 58, 175.
Giorgi, F., Raffaele, F., Coppola, E., 2019. The response of precipitation characteristics to global warming from climate projections. Earth System Dynamics 10, 73–89.
Godara, N., Bruland, O., 2019. Choosing an Appropriate Hydrologic Model. Department of Civil and Environmental Engineering NTNU.
Gupta, H.V., Kling, H., Yilmaz, K.K., Martinez, G.F., 2009. Decomposition of the mean squared error and NSE performance criteria: Implications for improving hydrological modelling. Journal of hydrology 377, 80–91.
Hachemaoui, A., Elouissi, A., Benzater, B., Fellah, S., 2022. Assessment of the hydrological impact of land use/cover changes in a semi-arid basin using the SWAT model (case of the Oued Saïda basin in western Algeria). Modeling Earth Systems and Environment 8, 5611–5624.
Hadour, A., Mahé, G., Meddi, M., 2020. Watershed based hydrological evolution under climate change effect: An example from North Western Algeria. Journal of Hydrology: Regional Studies 28, 100671.
Hallouz, F., Meddi, M., Mahe, G., Karahacane, H., Eddine, S., Rahmani, A., 2019. Trend in precipitation and evolution of discharge in a climate change context: Wadi Mina watershed in Algeria. Revue des Sciences de l'Eau: Journal of Water Science 32, 83–114.
Hawkins, R.H., Theurer, F.D., Rezaeianzadeh, M., 2019. Understanding the basis of the curve number method for watershed models and TMDLs. Journal of Hydrologic Engineering 24, 06019003.
Hind, M., M'hammed, S., Djamal, A., Zoubida, N., 2022. Assessment of land use–land cover changes using GIS, remote sensing, and CA–Markov model: a case study of Algiers, Algeria. Applied Geomatics 14, 811–825.
Hosseinzadehtalaei, P., Ishadi, N.K., Tabari, H., Willems, P., 2021. Climate change impact assessment on pluvial flooding using a distribution-based bias correction of regional climate model simulations. Journal of Hydrology 598, 126239.
Hu, S., Shrestha, P., 2020. Examine the impact of land use and land cover changes on peak discharges of a watershed in the midwestern United States using the HEC-HMS model. Papers in Applied Geography 6, 101–118.
Hu, Z., Liu, S., Zhong, G., Lin, H., Zhou, Z., 2020. Modified Mann-Kendall trend test for hydrological time series under the scaling hypothesis and its application. Hydrological Sciences Journal 65, 2419–2438.
Huang, H., Cheng, S., Wen, J., Lee, J., 2008. Effect of growing watershed imperviousness on hydrograph parameters and peak discharge. Hydrological Processes: An International Journal 22, 2075–2085.
Huq, E., Abdul-Aziz, O.I., 2021. Climate and land cover change impacts on stormwater runoff in large-scale coastal-urban environments. Science of the Total Environment 778, 146017.
Hurkmans, R., Terink, W., Uijlenhoet, R., Moors, E.J., Troch, P.A., Verburg, P.H., 2009. Effects of land use changes on streamflow generation in the Rhine basin. Water resources research 45.

IPCC (Ed.), 2023. Climate Change 2022 - Mitigation of Climate Change: Working Group III Contribution to the Sixth Assessment Report of the Intergovernmental Panel on Climate Change. Cambridge University Press, Cambridge. https://doi.org/10.1017/9781009157926

Iqbal, M., Wen, J., Masood, M., 2022. Impacts of climate and land-use changes on hydrological processes of the source region of Yellow River, China. Sustainability 14 (22).

Islam, M.Y., Nasher, N.R., Karim, K.R., Rashid, K.J., 2023. Quantifying forest land-use changes using remote-sensing and CA-ANN model of Madhupur Sal Forests, Bangladesh. Heliyon 9.

Jaiswal, R.K., Ali, S., Bharti, B., 2020. Comparative evaluation of conceptual and physical rainfall–runoff models. Applied water science 10, 48.

Jiang, Y., Liu, C., Li, X., Liu, L., Wang, H., 2015. Rainfall-runoff modeling, parameter estimation and sensitivity analysis in a semiarid catchment. Environmental Modelling & Software 67, 72–88.

Kendall, M.G., 1948. The advanced theory of statistics. Vols. 1. The advanced theory of statistics. Vols. 1. 1.

Kiprotich, P., Wei, X., Zhang, Z., Ngigi, T., Qiu, F., Wang, L., 2021. Assessing the impact of land use and climate change on surface runoff response using gridded observations and swat+. Hydrology 8, 48.

Knoben, W.J., Freer, J.E., Woods, R.A., 2019. Inherent benchmark or not? Comparing Nash–Sutcliffe and Kling–Gupta efficiency scores. Hydrology and Earth System Sciences 23, 4323–4331.

Kulithalai S. S., P., Deka, P.C., 2022. Spatio-temporal classification and prediction of land use and land cover change for the Vembanad Lake system, Kerala: a machine learning approach. Environmental Science and Pollution Research 29, 86220–86236.

Kusre, B.C., Baruah, D.C., Bordoloi, P.K., Patra, S.C., 2010. Assessment of hydropower potential using GIS and hydrological modeling technique in Kopili River basin in Assam (India). Applied Energy 87, 298–309.

Legesse, D., Abiye, T.A., Vallet-Coulomb, C., Abate, H., 2010. Streamflow sensitivity to climate and land cover changes: Meki River, Ethiopia. Hydrology and Earth System Sciences 14, 2277–2287.

Li, H., Yu, C., Qin, B., Li, Y., Jin, J., Luo, L., Wu, Z., Shi, K., Zhu, G., 2022. Modeling the effects of climate change and land use/land cover change on sediment yield in a large reservoir basin in the East Asian monsoonal region. Water 14, 2346.

Li, R., Zhu, G., Lu, S., Sang, L., Meng, G., Chen, L., Jiao, Y., Wang, Q., 2023. Effects of Urbanization on the water cycle in the Shiyang River Basin: Based on stable isotope method. Hydrology and Earth System Sciences Discussions 2023, 1–34.

Liping, C., Yujun, S., Saeed, S., 2018. Monitoring and predicting land use and land cover changes using remote sensing and GIS techniques—A case study of a hilly area, Jiangle, China. PloS one 13, e0200493.

Liu, S., Xie, Y., Fang, H., Du, H., Xu, P., 2022. Trend Test for Hydrological and Climatic Time Series Considering the Interaction of Trend and Autocorrelations. Water 14, 3006.

Makhlouf Adel, K., Djamel, T., Yahyaoui, H., 2021. Integration of a GIS and HEC-HMS modeling to improve urban resilience to flood risk in Algiers, Algeria. Analele Universităţii din Oradea, Seria Geografie 31, 100–109.

Mami, A., Yebdri, D., Sauvage, S., Raimonet, M., Miguel, J., 2021. Spatio-temporal trends of hydrological components: the case of the Tafna basin (northwestern Algeria). Journal of Water and Climate Change 12, 2948–2976.

Mamuye, M., Kebebewu, Z., 2018. Review on impacts of climate change on watershed hydrology. atmosphere 8.
Mann, H.B., 1945. Nonparametric tests against trend. Econometrica: Journal of the econometric society 245–259.
Masood, M.U., Haider, S., Rashid, M., Aldlemy, M.S., Pande, C.B., Đurin, B., Homod, R.Z., Alshehri, F., Elkhrachy, I., 2023. Quantifying the impacts of climate and land cover changes on the hydrological regime of a complex dam catchment area. Sustainability 15, 15223.
Mendez, M., Maathuis, B., Hein-Griggs, D., Alvarado-Gamboa, L.-F., 2020. Performance evaluation of bias correction methods for climate change monthly precipitation projections over Costa Rica. Water 12, 482.
Mengistu, A.G., Woldesenbet, T.A., Dile, Y.T., Bayabil, H.K., 2023. Modeling the impacts of climate change on hydrological processes in the Baro–Akobo River basin, Ethiopia. Acta Geophysica 71, 1915–1935.
Ming, A., Rowell, I., Lewin, S., Rouse, R., Aubry, T., Boland, E., 2021. Key messages from the IPCC AR6 climate science report.
Mishra, S., Sahu, R.K., Eldho, T.I., Jain, M., 2006. An Improved IaS Relation Incorporating Antecedent Moisture in SCS-CN Methodology. Water Resour. Manage. 20, 643–660. https://doi.org/10.1007/s11269-005-9000-4
Mishra, V.N., Rai, P.K., 2016. A remote sensing aided multi-layer perceptron-Markov chain analysis for land use and land cover change prediction in Patna district (Bihar), India. Arabian Journal of Geosciences 9, 1–18.
Moriasi, D., Arnold, J., Van Liew, M., Bingner, R., Harmel, R.D., Veith, T., 2007. Model Evaluation Guidelines for Systematic Quantification of Accuracy in Watershed Simulations. Transactions of the ASABE 50. https://doi.org/10.13031/2013.23153
Msovu, U.E., Mulungu, D.M., Nobert, J.K., Mahoo, H., 2019. Land use/cover change and their impacts on streamflow in Kikuletwa Catchment of Pangani River Basin, Tanzania. Tanzania Journal of Engineering and Technology 38, 171–192.
Mutayoba, E., Kashaigili, J.J., Kahimba, F.C., Mbungu, W., Chilagane, N.A., 2018. Assessing the impacts of land use and land cover changes on hydrology of the Mbarali River Sub-Catchment. The Case of Upper Great Ruaha Sub-Basin, Tanzania. Engineering 10, 616.
Nugroho, A.B., Hasyim, A.W., Usman, F., 2018. Urban growth modelling of Malang city using artificial neural network based on multi-temporal remote sensing. Civil and Environmental Science Journal 1, 52–61.
Ogden, F.L., 2021. Geohydrology: Hydrological Modeling, in: Alderton, D., Elias, S.A. (Eds.), Encyclopedia of Geology (Second Edition). Academic Press, Oxford, pp. 457–476. https://doi.org/10.1016/B978-0-08-102908-4.00115-6
Orkodjo, T.P., Kranjac-Berisavijevic, G., Abagale, F.K., 2022. Impact of climate change on future precipitation amounts, seasonal distribution, and streamflow in the Omo-Gibe basin, Ethiopia. Heliyon 8.
Piani, C., Haerter, J.O., Coppola, E., 2010. Statistical bias correction for daily precipitation in regional climate models over Europe. Theoretical and applied climatology 99, 187–192.
Rashid, H., Yang, K., Zeng, A., Ju, S., Rashid, A., Guo, F., Lan, S., 2021. Predicting the hydrological impacts of future climate change in a humid-subtropical watershed. Atmosphere 13, 12.
Rathjens, H., Bieger, K., Srinivasan, R., Chaubey, I., Arnold, J.G., 2016. CMhyd user manual. Doc. Prep. Simulated Clim. Change Data Hydrol. Impact Study 1413.

Rawat, J.S., Kumar, M., 2015. Monitoring land use/cover change using remote sensing and GIS techniques: A case study of Hawalbagh block, district Almora, Uttarakhand, India. The Egyptian Journal of Remote Sensing and Space Science 18, 77–84.

Rezaei, A.R., Ismail, Z.B., Niksokhan, M.H., Ramli, A.H., Sidek, L.M., Dayarian, M.A., 2019. Investigating the effective factors influencing surface runoff generation in urban catchments–A review. Desalination Water Treat 164, 276–292.

Richards, J.A., Jia, X., 2006. Interpretation of hyperspectral image data. Remote sensing digital image analysis: An introduction 359–388.

Ross, C.W., Prihodko, L., Anchang, J., Kumar, S., Ji, W., Hanan, N.P., 2018. Global hydrologic soil groups (HYSOGs250m) for curve number-based runoff modeling. ORNL DAAC, Oak Ridge, Tennessee, USA.

Saghafian, B., Farazjoo, H., Bozorgy, B., Yazdandoost, F., 2008. Flood intensification due to changes in land use. Water resources management 22, 1051–1067.

San José, R., Pérez, J.L., González, R.M., Pecci, J., Garzón, A., Palacios, M., 2016. Impacts of the 4.5 and 8.5 RCP global climate scenarios on urban meteorology and air quality: Application to Madrid, Antwerp, Milan, Helsinki and London. Journal of Computational and Applied Mathematics 293, 192–207.

Satya, B., Shashi, M., Deva, P., 2020. Future land use land cover scenario simulation using open source GIS for the city of Warangal, Telangana, India. Applied Geomatics 12, 281–290. https://doi.org/10.1007/s12518-020-00298-4

Schmidli, J., Frei, C., Vidale, P.L., 2006. Downscaling from GCM precipitation: a benchmark for dynamical and statistical downscaling methods. International Journal of Climatology: A Journal of the Royal Meteorological Society 26, 679–689.

Scott, D., Hall, C.M., Gössling, S., 2016. A review of the IPCC Fifth Assessment and implications for tourism sector climate resilience and decarbonization. Journal of Sustainable Tourism 24, 8–30.

Sen, P.K., 1968. Estimates of the regression coefficient based on Kendall's tau. Journal of the American statistical association 63, 1379–1389.

Shen, L., Li, J.B., Wheate, R., Yin, J., Paul, S.S., 2020. Multi-layer perceptron neural network and Markov chain based geospatial analysis of land use and land cover change. J. Environ. Inform. Lett 3, 29–39.

Shukla, P.R., Skea, J., Calvo Buendia, E., Masson-Delmotte, V., Pörtner, H.O., Roberts, D.C., Zhai, P., Slade, R., Connors, S., Van Diemen, R., 2019. IPCC, 2019: Climate Change and Land: an IPCC special report on climate change, desertification, land degradation, sustainable land management, food security, and greenhouse gas fluxes in terrestrial ecosystems.

Sleeter, B.M., Loveland, T., Domke, G., Herold, N., Wickham, J., Wood, N.J., 2018. Land cover and land use change. US Global Change Research Program.

Song, X., Kong, F., Zhu, Z., 2011. Application of Muskingum routing method with variable parameters in ungauged basin. Water Science and Engineering 4, 1–12.

Soriano, E., Mediero, L., Garijo, C., 2019. Selection of bias correction methods to assess the impact of climate change on flood frequency curves. Water 11, 2266.

Stainforth, T., Pepinster, S., 2022. CO2 emissions need to be reduced twice as fast as the rate they have gone up since 1990. IEEP AISBL. URL https://ieep.eu/news/co2-emissions-need-to-be-reduced-twice-as-fast-as-the-rate-they-have-gone-up-since-1990/ (accessed 4.26.24).

Taibi, S., Souag, D., 2012. Impact of Climate Change in Northern Algeria: Current Tendency of Precipitation and Temperature.

Teutschbein, C., Seibert, J., 2012. Bias correction of regional climate model simulations for hydrological climate-change impact studies: Review and evaluation of different methods. Journal of hydrology 456, 12–29.
Thom, H.C., 1958. A note on the gamma distribution. Monthly weather review 86, 117–122.
Trenberth, K.E., 2018. Climate change caused by human activities is happening and it already has major consequences. Journal of energy & natural resources law 36, 463–481.
Unger, N., 2010. NASA's Goddard Institute for Space Studies (GISS). Road Transportation Emerges as Key Driver of Warming in New Analysis from NASA.
United Nations, 2018. World Urbanization Prospects 2018 | Population Division [WWW Document]. URL https://www.un.org/development/desa/pd/news/world-urbanization-prospects-2018 (accessed 2.13.24).
USDA, 1986. Urban Hydrology for Small Watersheds, Technical Report 55.
Wang, Y., Leung, L.R., McGREGOR, J.L., Lee, D.-K., Wang, W.-C., Ding, Y., Kimura, F., 2004. Regional climate modeling: progress, challenges, and prospects. Journal of the Meteorological Society of Japan. Ser. II 82, 1599–1628.
Weslati, O., Bouaziz, S., Serbaji, M.M., 2023. Mapping and monitoring land use and land cover changes in Mellegue watershed using remote sensing and GIS. Arabian Journal of Geosciences 13, 1–19.
WRCP, C., 2015. CORDEX domains for model integrations.
Wuebbles, D., Easterling, D., Hayhoe, K., Knutson, T., Kopp, R., Kossin, J., Kunkel, K., LeGrande, A., Mears, C., Sweet, W., Taylor, P., Vose, R., Wehner, M., 2017. Our globally changing climate.
Xiao, B., Wang, Q., Jun, F., HAN, F.-P., DAI, Q.-H., 2011. Application of the SCS-CN Model to Runoff Estimation in a Small Watershed with High Spatial Heterogeneity. Pedosphere 21, 738–749. https://doi.org/10.1016/S1002-0160(11)60177-X
Xu, C., Chen, Yaning, Li, W., Chen, Yapeng, 2006. Climate change and hydrologic process response in the Tarim River Basin over the past 50 years. CHINESE SCI BULL 51, 25–36. https://doi.org/10.1007/s11434-006-8204-1
Yang, L., Feng, Q., Yin, Z., Wen, X., Si, J., Li, C., Deo, R.C., 2017. Identifying separate impacts of climate and land use/cover change on hydrological processes in upper stream of Heihe River, Northwest China. Hydrological Processes 31, 1100–1112.
Yang, X., Chen, R., Zheng, X.Q., 2016. Simulating land use change by integrating ANN-CA model and landscape pattern indices. Geomatics, Natural Hazards and Risk 7, 918–932.
Yeboah, K.A., Akpoti, K., Kabo-bah, A.T., Ofosu, E.A., Siabi, E.K., Mortey, E.M., Okyereh, S.A., 2022. Assessing climate change projections in the Volta Basin using the CORDEX-Africa climate simulations and statistical bias-correction. Environmental Challenges 6, 100439.
Yu, Z., 2015. HYDROLOGY, FLOODS AND DROUGHTS | Modeling and Prediction, in: North, G.R., Pyle, J., Zhang, F. (Eds.), Encyclopedia of Atmospheric Sciences (Second Edition). Academic Press, Oxford, pp. 217–223. https://doi.org/10.1016/B978-0-12-382225-3.00172-9
Yue, S., Wang, C., 2004. The Mann-Kendall test modified by effective sample size to detect trend in serially correlated hydrological series. Water resources management 18, 201–218.
Zeroual, A., Meddi, M., Bensaad, S., 2013. The impact of climate change on river flow in arid and semi-arid rivers in Algeria. IAHS-AISH Proceedings and Reports 359, 1–6.
Zhang, B., Shrestha, N.K., Daggupati, P., Rudra, R., Shukla, R., Kaur, B., Hou, J., 2018a. Quantifying the impacts of climate change on streamflow dynamics of two major rivers of the Northern Lake Erie Basin in Canada. Sustainability 10, 2897.

Zhang, B., Shrestha, N.K., Daggupati, P., Rudra, R., Shukla, R., Kaur, B., Hou, J., 2018b. Quantifying the impacts of climate change on streamflow dynamics of two major rivers of the Northern Lake Erie Basin in Canada. Sustainability 10, 2897.

Zhang, H.L., Wang, Y.J., Wang, Y.Q., Li, D.X., Wang, X.K., 2013. The effect of watershed scale on HEC-HMS calibrated parameters: a case study in the Clear Creek watershed in Iowa, US. Hydrology and Earth System Sciences 17, 2735–2745.

Zhang, X., Zhang, L., Zhao, J., Rustomji, P., Hairsine, P., 2008. Responses of streamflow to changes in climate and land use/cover in the Loess Plateau, China. Water resources research 44.

Zope, P.E., Eldho, T.I., Jothiprakash, V., 2017. Hydrological impacts of land use–land cover change and detention basins on urban flood hazard: a case study of Poisar River basin, Mumbai, India. Natural Hazards 87, 1267–1283.

Zope, P.E., Eldho, T.I., Jothiprakash, V., 2015. Impacts of urbanization on flooding of a coastal urban catchment: a case study of Mumbai City, India. Natural Hazards 75, 887–908.